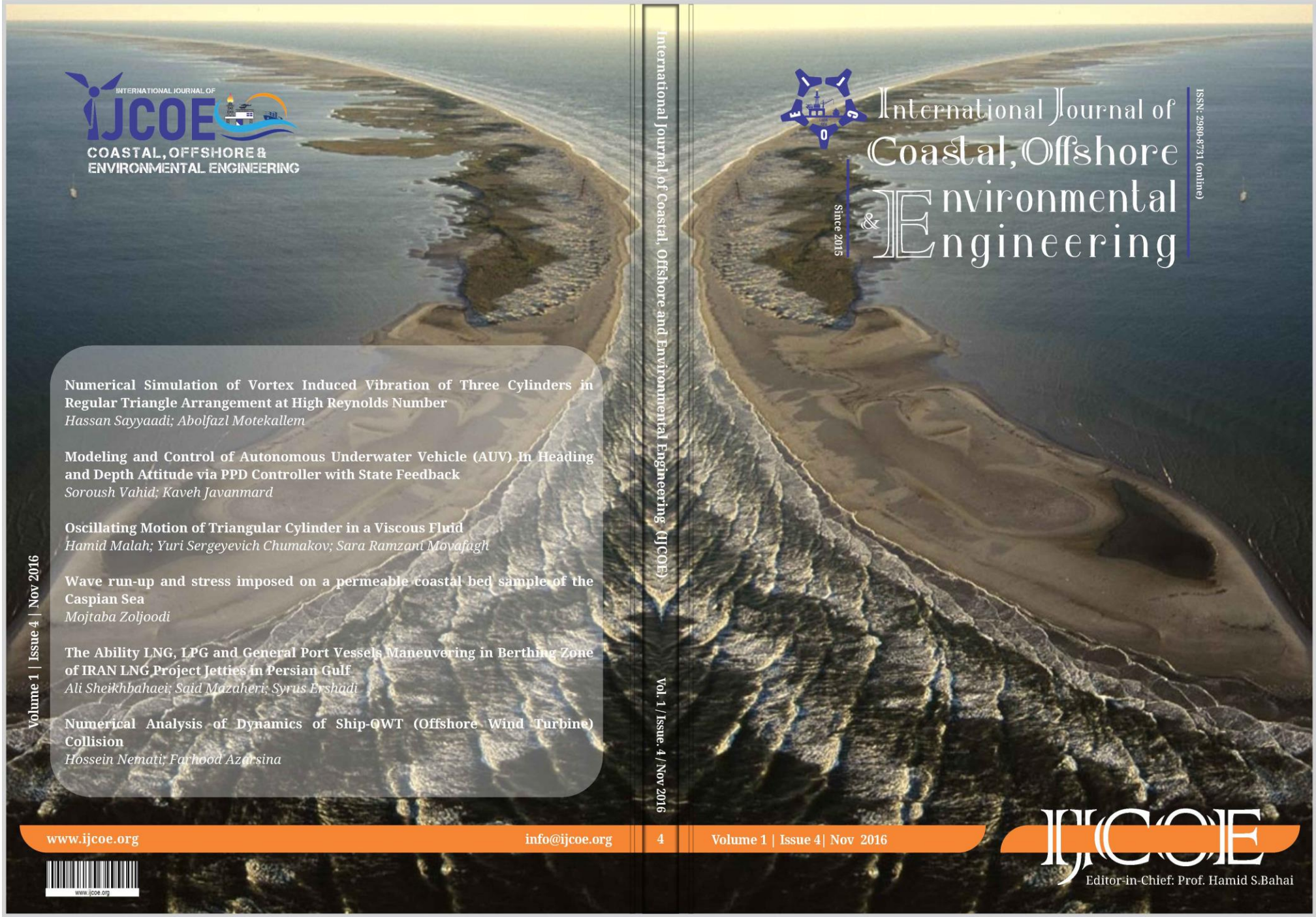

INTERNATIONAL JOURNAL OF
IJCOE
COASTAL, OFFSHORE & ENVIRONMENTAL ENGINEERING

Volume 1 | Issue 4 | Nov 2016

International Journal of Coastal, Offshore and Environmental Engineering (IJCOE)
Vol. 1 / Issue. 4 / Nov 2016
4

ISSN: 2980-8731 (online)

International Journal of
Coastal, Offshore & Environmental Engineering

Since 2015

www.ijcoe.org info@ijcoe.org

Volume 1 | Issue 4| Nov 2016

IJCOE

International Journal of Coastal, Offshore & Environmental Engineering
Since 2015
ISSN: 2980-8721 (online)

In The Name of God

Message from the Editor-in-Chief

The IJCOE journal office was established in 2015,and its first issue was published in 2016. TheIJCOE covers a wide range of research in thefields of oceanography & ocean technology, aswell as marine industries & marine engineering.The editorial board of IJCOE consists of nearly130 of the greatest scientists and researchersfrom over 30 countries worldwide, and thejournal's review board comprises 1,000 membersfrom all five continents. The membership andapplication process for joining the editorial andreview boards of this journal is ongoing. IJCOE isa research-academic quarterly journal that haspublication and distribution permissions fromthe Press Organization and permission topublish scientific-research articles from theMinistry of Science, Research, and Technology(MSRT) with an "A" rating. It also holds a "Q1"rating from the ISC institute with an impactfactor (IF) of approximately 0.43 and isconsidered a "core journal" (prestigious andoutstanding journal). IJCOE is an open-accessjournal and allows the download and receipt ofaccepted articles in full text for free. It respectsand adheres to copyright and COPE regulations.The journal's office operates 24/7, providingservices to researchers. In addition to publishinga regular quarterly journal, IJCOE has 16 specialissues on specific topics in preparation. It alsoprovides conditions for publishing specializedbooks, references, and handbooks. Moreover, itis ready to cooperate with the secretariats ofreputable international conferences to publishtheir selected and outstanding articles. IJCOEevaluates, appraises, and publishes books,articles, and the scientific achievements andfindings of esteemed researchers and scientistsworldwide who are innovating and conductingin-depth research in the "important and strategicfield of the maritime technology & Oceanengineering." It welcomes any form of jointcooperation with universities, research institutes,and related research centers at the national,regional, and international levels, and extends ahand for collaboration.

Classification of Editorial Board in IJCOE

Editor-in-Chief

Director-in-Chief

Deputy Editor

Executive Managers

English Text Editor

Technical Editor

International Editorial Board

National Editorial Board

Editorial Board Associate

Editorial Board Assistant

Guest Editorial Board

Advisory Board

Administrative Coordinator

Honorary Board Member

Methodology Advisor

Author Benefits

- Open Access
- Rapid Publication
- Thorough Peer-Review
- No Copyright Constraints
- Coverage by Leading Indexing Services
- Discounts On Article Processing Charges (APC)
- No Space Constraints, No restriction on the maximum length of the papers, number of figures or colors

INTERNATIONAL JOURNAL OF IJCOE COASTAL, OFFSHORE & ENVIRONMENTAL ENGINEERING

Aims of IJCOE

Hydrodynamics

Marine equipment

Structural mechanics

Ocean environmental predictions

Stochastic calculations Experimental

Automatic Control of Marine Systems

Scope of IJCOE

Marine Hazards

Ocean Acoustics

Naval Architecture

Ocean Engineering

Coastal Engineering

Marine Meteorology

Marine Earth Sciences

Underwater Technology

Marine Renewable Energy

Polar & Arctic Engineering

Marine Renewable Energy

Marine Geography & Geodesy

Marine Environmental Engineering

Automatic Control of Marine Systems

Hydro Physics & Physical Oceanography

Type of papers

- Case Studies
- Book Reviews
- Review Article
- Letters to the Editor
- Methodology Papers
- Editorials and Commentaries
- Response or Rejoinder Papers
- Perspective or Opinion Papers
- Conceptual or Theoretical Papers
- Meta-Analysis and Systematic Reviews
- Short Communications or Brief Reports
- Research Articles (Original Research Papers)

Scientific Research Journal

Ministry of Science, Research And Technology (MSRT)

Jurnal Ranking 2023: A

Ministry Of Science, Research And Technology (ISC)

Citation Impact 2022: 0.429

Quartile 2022 : Q1

Core Collection

IJCOE is a Member of

Cantact Us

Office 1 | Research Institute of Meteorology and Atmospheric Science

Address | Tehran, Shahid Kharrazi Highway, Pajoohesh Blvd, Research Institute of Meteorology and Atmospheric Science, Sand and Dust Storm International Research Center (SDS-IRC), No. 13, 1st floor.

Phone | +982144787652

Postal code | 13611-14977

website | www.rimac.ac.ir

Office 2 | Iranian National Institute for Oceanography and Atmospheric Science

Address | Tehran, Dr. Fatemi Gharbi St., Shahid Etemadzade St., No. 3, third floor.

Phone | +982166944873

Postal code | 13389 – 14118

website | www.inio.ac.ir

Email | Info@ijcoe.org

Website | www.ijcoe.org

Follow Us

www.ijcoe.org

INTERNATIONAL JOURNAL OF IJCOE COASTAL, OFFSHORE & ENVIRONMENTAL ENGINEERING

Volume & Issue:

Volume 1, Issue 4, November 2016

Number of Articles: 6

Content

INTERNATIONAL JOURNAL OF
COASTAL & OFFSHORE ENGINEERING
IJCOE No. 4 / Autumn 2016 (1-10)

Numerical Simulation of Vortex Induced Vibration of Three Cylinders in Regular Triangle Arrangement at High Reynolds Number

Hassan Sayyaadi [1], Abolfazl Motekallem[2]

[1]*Professor, Center of Excellence in Hydrodynamics and Dynamics of Marine Vehicles, Sharif University of Technology/ Scholl of Mechanical Engineering; Sayyaadi@sharif.edu*
[2] *M.Sc. student, Sharif University of Technology/ School of Mechanical Engineering; Motekallem_Abolfazl@mech.sharif.edu*

ARTICLE INFO

Article History:
Received: 11 Sep. 2016
Accepted: 15 Dec. 2016

Keywords:
Fluids Structure Interaction (FSI)
Workbench System Coupling
Vortex Induced Vibration,
Numerical Method
Karman Vortex Shedding

ABSTRACT

This paper presents a three dimensional simulation of the vortex induced vibrations of three elastic cylinders in regular triangle arrangement at high Reynolds number. The motion of every single cylinder, which is free to oscillate in two degrees of freedom in a uniform flow and has the same mass and natural frequency in both X and Y directions, is modeled by a mass spring damping system. The displacement and lift forces for each cylinder are analyzed with five spacing ratios L/D changing from 2.5 to 6.5. The results indicate that the downstream cylinders are usually undergone serious fluctuating lift forces. It is found that the simultaneous resonance in the X and Y directions may occur for the downstream cylinders.
The stream wise oscillation of downstream cylinders could be as large as 0.54D, and the maximum transverse amplitude of three cylinders can reach to 2.30D. It is indicated that the cross flow oscillation amplitude of three cylinders significantly increased compared with the flow induced vibration of a single elastic cylinder and the stream wise oscillation of downstream cylinders is unneglectable for vortex induced vibration of multi cylinder system.

1. Introduction

The viability and accuracy of large eddy simulation (LES) with wall modeling for high Reynolds number complex turbulent flows is investigated by Pietro Catalano (2003), considering the flow around a circular cylinder in the super critical regime (5×10^5 and 10^6) [1]. Guilmineau (2004) present some numerical results from a study of the dynamics and fluid forcing on an elastically mounted rigid cylinder with low mass damping, constrained to oscillate transversely to a free stream [2]. Z. Huang (2006) had performed a systematic study of flow around one cylinder, two side by side cylinders, one row of cylinders and two rows of cylinders [3]. Experimental measurements and large eddy simulation (LES) technique were used by K. Lam to study the turbulent flow characteristics in a staggered tube bundle arrangement in 2010 at a subcritical Reynolds number of Re=7500 [4]. K. Lam presents the results of an investigation on the effects of wavy cylindrical tubes in a staggered heat exchanger tube bundle. The aim of this investigation is to compare the flow characteristics of a new configuration of cylindrical tubes with that of a similar arrangement which comprises purely circular cylinders. For the flow induced vibration problem some numerical work also carried out. A numerical study has been carried out by S. Mittal to study the flow induced vibrations of a pair of cylinders in tandem and staggered arrangements at Re=100 [5]. Detailed numerical results for the flow patterns for different arrangements of the cylinders, at a Reynolds number, Re=800, are presented. Several qualitatively distinct wake regimes were observed experimentally as well as numerically by F.L. Ponta (2006) [6]. In year 1996, C.H.K. Williamson had studied the three dimensional vortex behavior of flow past a bluff body [7]. Results predict that for a low Reynolds number flow ($Re < 260$) in wake region of the bluff body the flow remains two dimensional behavior. For $Re > 260$ the vortex generated due to flow past a bluff body having a three dimensional nature of flow.
In summary, thus, many experimental as well as numerical work at higher Reynolds no is done in FIV area. Some of them have calculated the FIV and suggested the techniques to damp the vibration, where

as some work are done experimentally by changing orientation of tube bundle in triangular array. Literatures also suggest the appropriate condition to setup the model of FIV. In spite of all these studies, the investigations of flow induced vibrations as a fully coupled problem are still incomplete. In addition, little theoretical work has been done for the simulation and control of flow induced vibrations

1. Numerical Method

The simulation associated with VIV includes the unsteady fluid flow and the motion of the cylinder. The interaction between fluid and cylinder is significant to the process.

2.1 The governing equations

The governing equations of fluid are the unsteady and viscous Navier Stokes equations written in terms of conservative variables. The continuity, momentum and energy equations are as follows:

$$\frac{\partial \rho}{\partial t} + \frac{\partial (\rho u_k)}{\partial x_k} = 0 \tag{1}$$

$$\frac{\partial (\rho u_i)}{\partial} + \frac{\partial (\rho u_i u_k + p\delta_{ik} - \tau_{ik})}{\partial x_k} = 0 \tag{2}$$

$$\frac{\partial E}{\partial t} + \frac{\partial [u_k (E + p) - \tau_{ik} u_i + Q_k]}{\partial x_k} = 0 \tag{3}$$

where the velocity components by u_k and the relationship for the total energy E is given by

$$E = \frac{p}{\gamma - 1} + \frac{1}{2}\rho u_k u_k \tag{4}$$

where γ is the specific heat capacity ratio, p is the pressure. The heat flux and stress tensor are given by

$$Q_k = -\frac{\gamma}{(\gamma - 1) RePr} \frac{\partial T}{\partial x_k} \tag{5}$$

$$\tau_{ik} = \frac{1}{Re}\left(\frac{\partial u_i}{\partial x_k} + \frac{\partial u_i}{\partial x_k}\right) - \frac{2}{3}\frac{1}{Re}\delta_{ik}\frac{\partial u_j}{\partial x_j} \tag{6}$$

where $\Pr = 0.72$ and Re are Prandtl and Reynolds numbers. The 2nd order finite difference is used as the spatial discretization scheme. The third order Runge Kutta scheme is applied for the temporal discretization. The immersed boundary method uses a regular Eulerian computational grid for the fluid mechanics together with a Lagrangian representation of the immersed boundary. Boundary movement to the orthogonal mesh can be simply done by changing the coordinates of boundary points without any adjustment to the basic grid, so the immersed boundary methods do not cost additional time for regridding. The boundary condition of velocity on the body surface is

$$u_f = u_b \tag{7}$$

where u_f is the velocity of fluid at a point on the surface, $u_b$is the velocity of this point on the body. An adiabatic boundary condition is used for temperature in the present work. The critical problem for the computation is implementing the boundary conditions for a body nonconformal grid. Instead of a curvilinear body nonconformal grid used by Ghias et al [8], an orthogonal body nonconformal grid is used as shown in Fig. 1. In the present work, some modifications are made for implementing the boundary conditions. In Fig. 1, the p_1 is a typical point whose parameters cannot be calculated by solving Eqs. (1)-(3). The parameters at this point have to be interpolated from the solid surface p_s and point p_2. The line $p_s p_2$ is across point p_1 and perpendicular to the solid surface. Point p_1 is on the solid surface, at which the velocity $(u_{s-x}.u_{s-y})$ is known. The velocity at point p_2 is $(u_{2-x}.u_{2-y})$,which can be interpolated from local grid $(i_0.j_0).(i_0+1.j_0).(i_0+1.j_0+1)$ and $(i_0+1.j_0+1)$. The u_{2-x}can be expressed as

$$u_{2-x} = \sum_{i=i_0}^{i_0+1}\sum_{j=j_0}^{j_0+1} \delta\left(\frac{h_x}{h}\right)\delta\left(\frac{h_y}{h}\right)(u_x)_{ij} \tag{8}$$

where the delta function is defined as

$$\delta(x) = \begin{cases} 1 - |x| & |x| < 1 \\ 0 & |x| \geq 1 \end{cases} \tag{9}$$

Here h_x denotes the element size near the solid surface. h_x and h_y are the distances between point p_2 and adjacent grid in the X and Y direction, respectively. Then, the u_{1-x} at u_1 can be calculated by

$$u_{1-x} = \frac{l_1}{l}u_{2-x} + \frac{l_2}{l}u_{s-x} \tag{10}$$

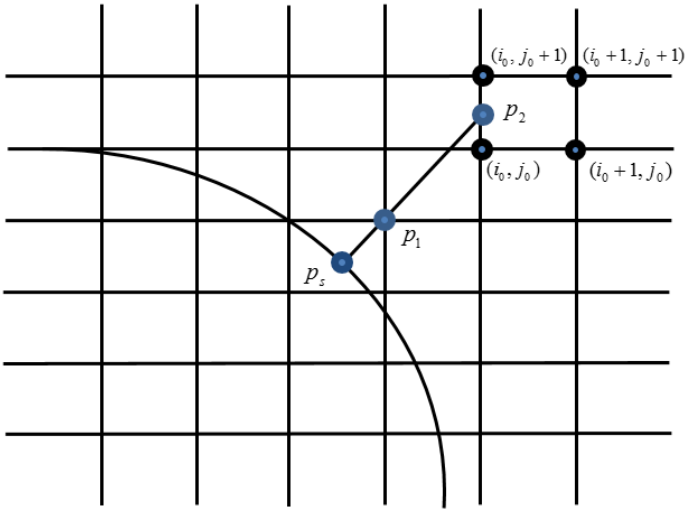

Fig. 1. Schematic showing an immersed boundary on an orthogonal body nonconformal grid.

where l_1 is the distance between points p_1 and p_s, and l_2 is the distance between points p_1 and p_2. l is $l_1 + l_2 + l_3$ set to $1 \cdot 5h$, which ensures that the interpolation of parameters at point p_2 is independent of parameters at point p_1. Temperature at p_1 is determined by assuming adiabatic condition at Point p_s and the density is determined by applying the equation of state at the wall.

In this simulation, drag and lift force coefficients are used to quantify the hydrodynamic characteristics. The definitions are also given here:

$$C_x = \frac{F_x}{\frac{1}{2}\rho U^2 DL} \tag{11}$$

$$C_y = \frac{F_y}{\frac{1}{2}\rho U^2 DL} \tag{12}$$

Here F_x and F_y are the fluid forces exerted on the bodies, respectively, in streamwise and transverse directions and are calculated by performing an integration along the wall, involving both pressure and viscous effects:

$$F_x = -\int_S (pn + \mu n \times \omega) n_x da \tag{13}$$

$$F_y = -\int_S (pn + \mu n \times \omega) n_y da \tag{14}$$

where $\omega = \nabla u$, whose value is calculated from the velocities at points p_s and p_2 in Fig. 1. The pressure on the surface is extrapolated from the interior of the flow onto the boundary. **n** denotes the outward unit normal to the cylinder surface. n_x and n_y are the Cartesian components of $\boldsymbol{n} \cdot S$ represents the cylinder surface. In order to analyze the aerodynamic behavior of VIV, we define the instantaneous potential added-mass and vortex force coefficients as

$$C_{Potential}(t) = 2\pi^3 \frac{[y(t)/D]}{(U^*/f^*)^2} \tag{15}$$

$$C_{Vortex}(t) = C_y(t) - C_{Potential}(t) \tag{16}$$

which are same as the definitions used by Govardhan and Williamson [9], $C_{Potenial}(t)$ is always in phase with the cylinder motion $y(t)$. Frequency ratio $f^* = f/f_N$; reduced velocity $U^* = U/f_N D$; and y is the displacement in transverse direction.

2.2. The equations for a rigid cylinder

The motion of the elastically mounted rigid cylinder is restricted in the transverse direction (Y axis in the present simulation), and is governed by

Vibration equations,

$$m\ddot{x} + c\dot{x} + kx = F \tag{17}$$

Force in X direction,

$$m\ddot{x} + c\dot{x} + kx = F_x \tag{18}$$

Force in Y direction,

$$m\ddot{x} + c\dot{x} + kx = F_y \tag{19}$$

Where, the forces F_x and F_y are the total drag and lift forces acting on the cylinder and ,c and k are the tube

mass per unit length, structural damping coefficient and spring constant respectively.

Drag and Lift coefficient,

$$C_D = \frac{F_D}{\frac{1}{2}\rho U_\infty^2 D} \tag{20}$$

$$C_L = \frac{F_L}{\frac{1}{2}\rho U_\infty^2 D} \tag{21}$$

Where, F_x and F_y are the total drag and lift forces exerted by the fluid acting on cylinder per unit cylinder length. Therefore $C_D = C_{DP} + C_{DF}$where C_{DP} and C_{DF} are pressure and friction drag coefficients respectively. The frequency of vortex shedding (f) in wake region is given by Strouhal number (St) and it is defined as

$$St = \frac{fD}{U_\infty} \tag{22}$$

Vortex shedding from a smooth, circular cylinder in a steady flow is a function of Reynolds number. The Reynolds number is based on free stream velocity *U* and cylinder diameter *D,*

$$Re = \frac{\rho U_\infty D}{\mu} \tag{23}$$

The cylinder has been modeled as a two degree of freedom system with independent responses in X the drag direction, and Y the lift direction. The initial conditions of the cylinder are zero displacement and velocity. As discussed in the introduction, the response is assumed to be two dimensional with symmetry along the cylinder axis. The following properties are applied:

k - Stiffness is 25.5742 N/m
m - Mass per unit length is 7.804kg/m

2. FSI Solution of ANSYS

The VIV behavior of a circular cylinder is simulated by a transient coupled FSI numerical model using the combination of CFX and ANSYS transient structure platforms. The well designed FSI solution scheme provides tight integrations between hydrodynamics and structural physics, offering a flexible, advanced structure fluid analysis tool. The geometry module provides a geometric model for the transient structure solver and the ANSYS CFX solver. Coupled simulations begin with the execution of the ANSYS transient structure and ANSYS CFX solvers. The system coupling solver acts as a coupling master process to which the transient structure solver and ANSYS CFX solvers connect. Once that connection is established, the solvers advance through a sequence of predefined synchronization points (SP). At each of these SPs, the ANSYS CFX solver transfers the fluid dynamic loads data to the transient structure solver based on the system coupling solver; in turn, the transient structure solver transfers the structure response data to the ANSYS CFX solver also based on the system coupling solver. Finally, the mesh is updated with the diffusion based smoothing method based on the response of the cylinder. The coupled simulation proceeds in time during the outer loop. Staggered iterations are repeated until a maximum number of stagger iterations is reached or until the data transferred between solvers and all field equations have converged. The adoption of implicit coupling iteration ensures that fluid and structure solution fields are consistent with each other at the end of each multi field step, leading to improved numerical solution stability.

3. Problem Definition

Consider unsteady, three dimensional, viscous, incompressible flow past triangular array of circular cylinder placed in a uniform stream, as shown schematically in Fig. 2. The flow is bounded by the plane at upper and lower side boundaries.

These are treated as symmetry boundary condition, while vertical plane at left side and vertical plane right of the domain are considered as the flow inlet and outlet planes respectively. Free stream velocity is specified as 0.5 m/s at the inflow boundary. Three stationary cylinders are placed in triangular array, two downstream sides and one upstream side. The cylinder wall is considered as no slip boundary condition (Fig. 2). Consider upper downstream side cylinder as cylinder D.U. Riser, lower downstream side cylinder as cylinder D.D. Riser and upstream cylinder as cylinder U. Riser hereafter. All three stationary circular cylinders are of diameter D (D=0.1m). It is observed from Fig. 2 that upstream cylinders were placed at 10D and 30D distance away from the inlet and outlet boundaries, respectively. Five different (L/D = 2.5 to 6.5) considered in the present study.

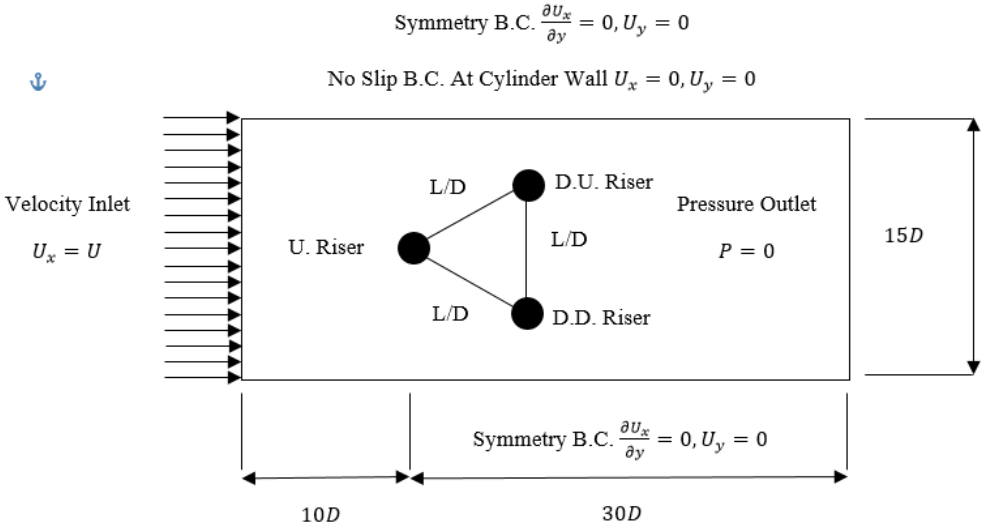

Fig. 2. Schematic of 2 DOF computational domains.

4. Mesh Validation

Mesh dependency study was carried out and it has been demonstrated that further increasing in mesh density makes little difference on the results for the Strouhal numbers simulated. Fig. 3 shows the computational domain as well as the generated grid (for one of the test cases). The size of the domain used in the numerical investigation was 40D×15D. In order to set up a grid independent solution, numerical simulations have been conducted for different meshes and the optimum mesh consisted of 272840 quadrilateral elements, with a finer mesh employed near the boundary layer to capture the flow behavior, since the boundary layer flow patterns are significant in this investigation. The number and type of mesh elements have been selected in an iterative solution with a minimal time step to obtain an accurate solution.

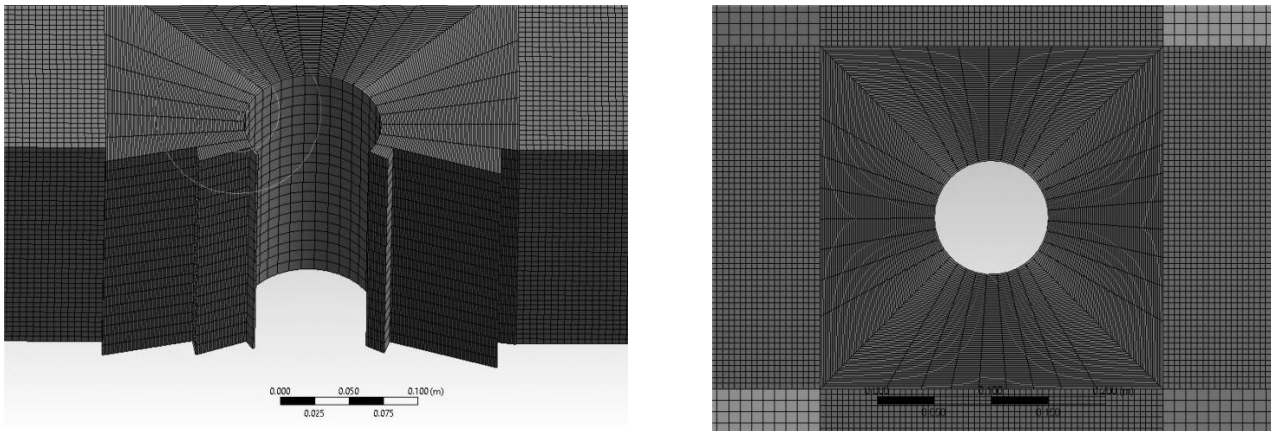

(a) (b)

Fig. 3. (a). Three dimensional grids near the cylinders, (b). Horizontal section of grids near the cylinders.

The same geometry and mesh elements, as well as initial and boundary conditions, were used for all numerical simulations. Based on the mesh size and the free stream velocity, the selected time step was kept constant in all simulations, $\Delta t = 0 \cdot 005 s$. Based on this time step the maximum number of iterations per each time step was 25. To reach solution convergence of the computational analyses the residual target of $10 - 5$was considered. In addition, the lift and drag coefficients on the cylinders were monitored during the computational process and sinusoidal behavior of these coefficients was taken into account to accompany the convergence criterion. Furthermore, a grid independent study was conducted with several mesh elements qualities for one of the test cases (L/D=2.5). Here, the mesh refinement sensitivity is summarized in Table 1. According to the findings, the refined mesh was chosen for the rest of the simulations and LES turbulence models were used to investigate the turbulent flow behavior around the three cylinders.

Table 1: Mesh Dependence Study at $Re = 4 \cdot 97 \times 10^5$ and $U^* = 5 \cdot 5$ for different meshes.

Mesh Case	Number of Elements	Lift Frequency	Drag Frequency	f_x/f_y	Strouhal Number
1	122700	0.75	1.56	2.08	0.15
2	272840	0.85	1.71	2.01	0.17
3	491250	0.85	1.76	2.07	0.17

5. Model Validation

Firstly, the flow around a rigid cylinder at $Re = 1 \cdot 1 \times 10e5$ is carried out in order to ensure the reliability of numerical calculation. In Fig. 4, high Reynolds number ($Re > 4 \times 10e5$) VIV data obtained through UTM experiments are presented along with results calculated through CFD simulations. The results in Fig. 4 are showing the ability of ANSYS CFX for detecting the oscillating behavior and nearly the same vertical displacement for the cylindrical riser as that for the experimental results at UR = 6.0. However, there is a noticeable irregular phase shift between the numerical and the experimental. Where the uniform flow condition was imposed exactly at the inlet boundary condition at all CFD simulations in this study, while in the experimental tests in UTM towing tank this uniform flow condition cannot be attained exactly. In addition, this miss matching between the experimental and the numerical results can also be attributed to the inability of the turbulence models even with the use of LES for predicting precisely the complex flow pattern of VIV for such cases [10]. Results shows maximum error between the numerical simulation and the experimental in lift coefficient is %16 at UR = 5.0. It is shown that the grid resolution, time step and numerical solving format chosen in present paper are proper for numerical simulation of the flow around the cylinder.

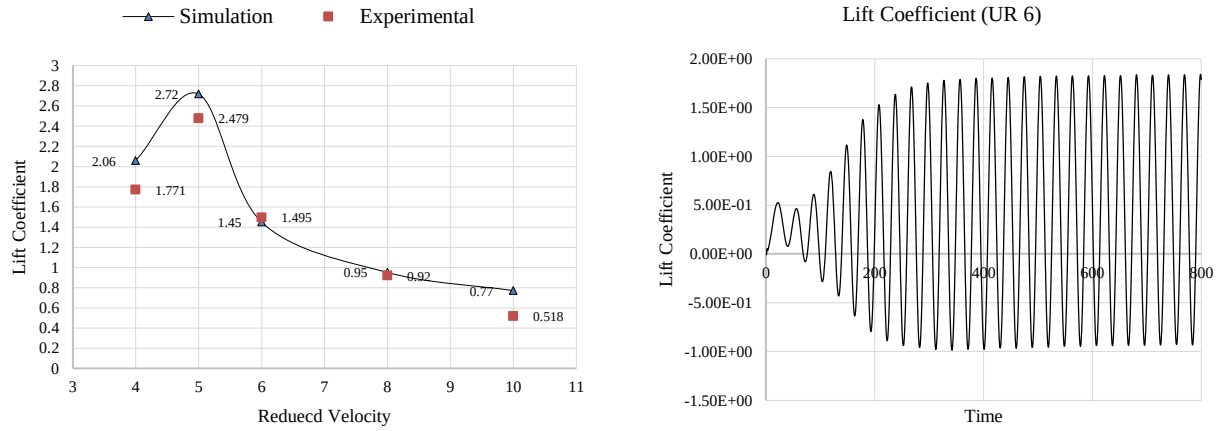

Fig. 4. Amplitude response of an elastically mounted circular cylinder in fluid flow.

6. Result and Discussion

Fig. 5 shows the force coefficients vary as the spacing ratio for three cylinders in regular triangle arrangement, which include the mean value of lift coefficient C_l. Fig. 5 indicates that the mean lift coefficients of downstream cylinders D.U. Riser and D.D. Riser are equal to each other in magnitude with opposite direction. It is seen that C_l D.U. Riser is positive and C_l D.D. Riser is negative, and the C_l U. Riser has positive negative value for L/D=2.5~5.5. All lift coefficient mean values gradually trend to zero as L/D increasing, and it indicates that the flow interference effects between upper and lower rows cylinders is gradually weakened as spacing increasing.

The ratio of cross flow displacement mean values to diameter is shown in Fig. 6. The ratio of the inflow displacement mean values to diameter is shown in Fig. 7(a) and Fig. 7(b), respectively. In Fig. 6, the cross flow displacement mean Y of each cylinder express same trend with the lift coefficients as shown in Fig. 5. When the L/D changes from 2.5 to 3.5, the Y magnitude of each cylinder obviously increase. In the region of L/D=2.5~3.5, the cross flow displacement amplitude of U. Riser, D.U. Riser and D.D. Riser reach their maximum values with 0.47, 2.30 and 1.92 times of cylinder diameter, respectively.

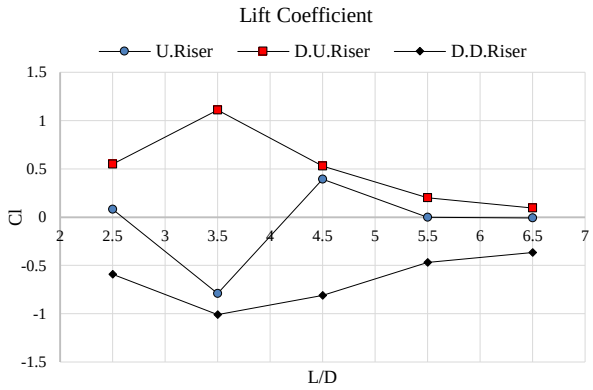

Fig. 5. Mean values of lift coefficients versus L/D.

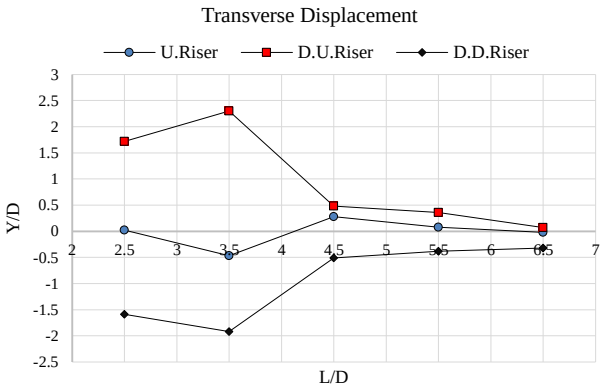

Fig. 6. Mean values of Y directions displacement versus L/D

In Fig. 7(a), it can be seen that the inflow displacement means $X_{D.U.\ Riser}$, $X_{D.D.\ Riser}$ of downstream cylinders have the same changing trend and increase in the all L/D range. The $X_{U.\ Riser}$ of upstream cylinder gradually increases from 0.31 to 0.64 as L/D increases and reaches the maximum value at L/D=6.5 that shown in Fig. 7(b).

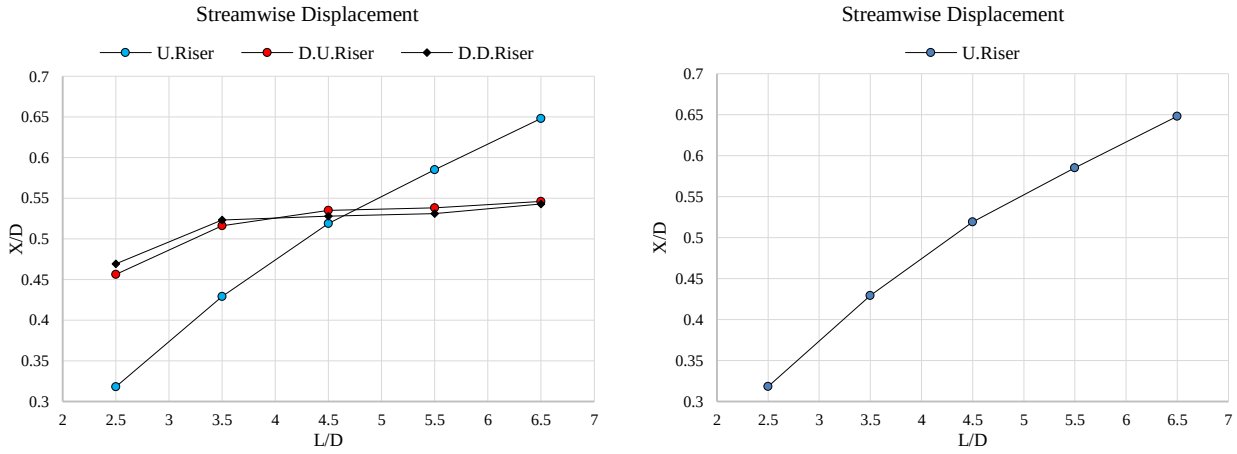

(a) (b)

Fig. 7. (a). Mean values of X directions displacement versus L/D, (b). Mean values of $X_{U.\ Riser}$ directions displacement versus L/D

Finally, contours of flow velocity of the model are shown in Fig. 8 to 11. The distance between the spacing ratio is considered L/D=3.5 that have maximum cross flow displacement. The velocity contours are shown when the oscillating cylinders are at their uppermost and lowermost positions. Fig. 8 shows the results for L/D=3.5 when all cylinders are at their minimum position in X direction and Fig. 9 shows the same contours for the maximum position in X direction. As it can be seen, the movement of downstream cylinders is more than upstream cylinder and also another thing that should be mention is the upstream cylinder never goes behind the reference point and all of its movements are in right hand of the reference point. In the other hand, the downstream cylinders, moves either in left or right hand of the reference point. The maximum amplitude for upstream cylinder in X direction is almost 0.64D and for downstream cylinders is slightly below 0.54D.

Fig. 10 shows the results for L/D=3.5 when the both cylinders are at their minimum positions in Y direction and Fig. 11 the same results when they are at their maximum positions in Y direction. For the upstream cylinder the maximum amplitude is about 0.47D and for downstream cylinders is almost 2.30 and 1.92 for D.U. Riser and D.D. Riser, respectively. It shows that downstream cylinders at L/D=3.5, have the same of movement and this is the exception because as can be seen in Fig.6, at all other spacing ratio, there are a different amplitude in Y direction for cylinders. Also the counter of velocity shows that the shear layers roll down after the downstream body and roll up after the upstream body.

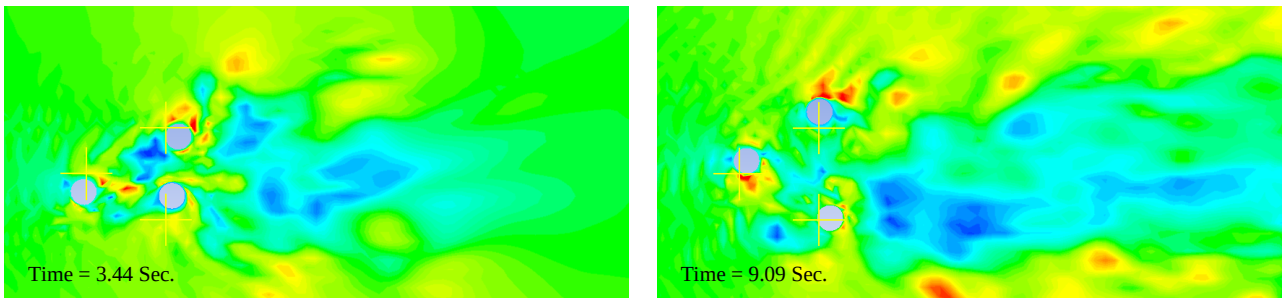

(a) (b)

Fig. 8. Velocity contours of three cylinders in triangle arrangement, L/D=3.5; Lowermost position of (a). Upstream cylinder in X direction, (b). Downstream cylinders in X direction

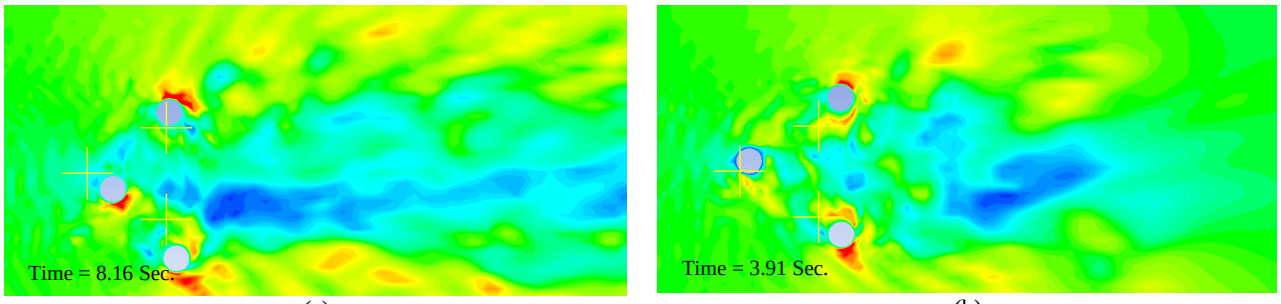

(a) (b)

Fig. 9. Velocity contours of three cylinders in triangle arrangement, L/D=3.5; Uppermost position of (a). Upstream cylinder in X direction, (b). Downstream cylinders in X direction

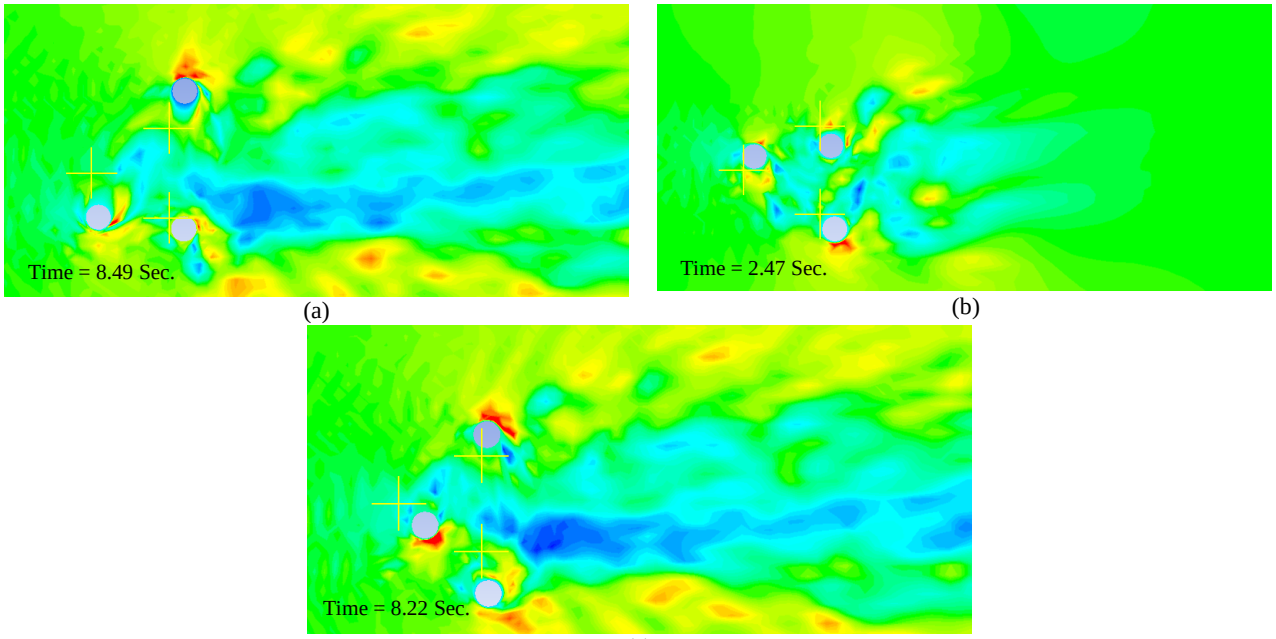

(a) (b)

(c)

Fig. 10. Velocity contours of three cylinders in triangle arrangement, L/D=3.5; Lowermost position of (a). Upstream cylinder in Y direction, (b). Downstream cylinder (D.U. Riser) in Y direction, (c). Downstream cylinder (D.D. Riser) in Y direction

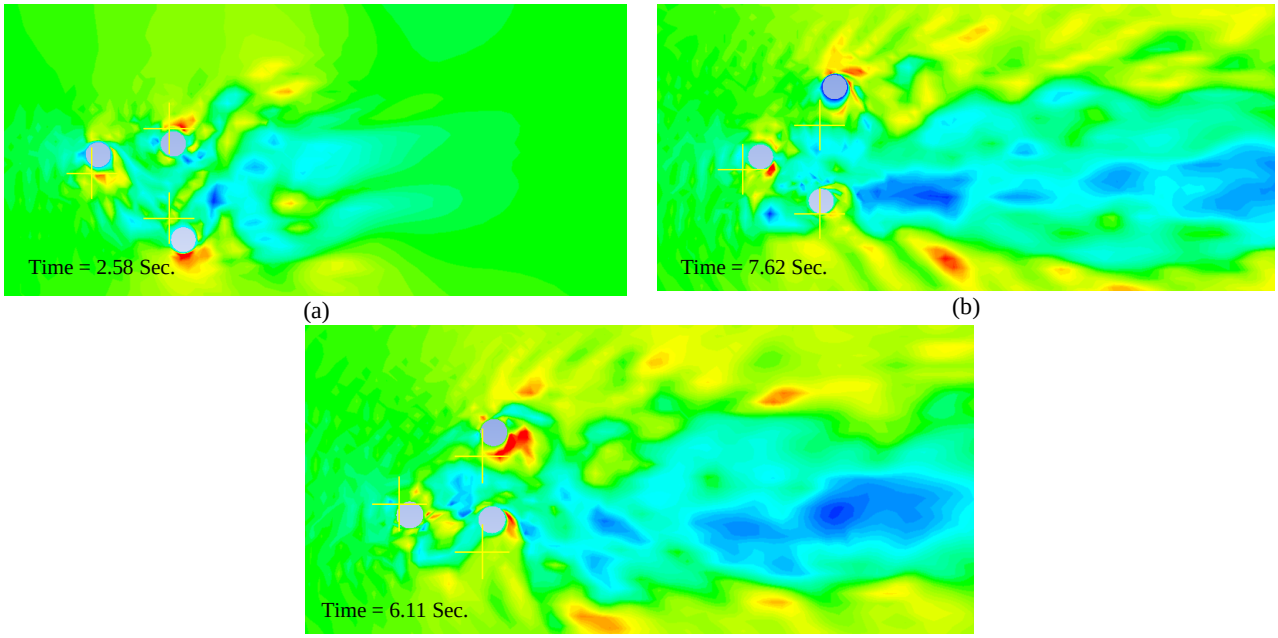

Fig. 11. Velocity contours of three cylinders in triangle arrangement, L/D=3.5; Uppermost position of (a). Upstream cylinder in Y direction, (b). Downstream cylinder (D.U. Riser) in Y direction, (c). Downstream cylinder (D.D. Riser) in Y direction

Conclusion

This paper presents a feasible research method for numerical simulation of vortex induced vibration of elastic multi cylinder oscillating system. The fluid domain simulation is completed by ANSYS CFX, the structure response is achieved using the LES turbulence method and the grid domain updating is accomplished through a dynamic mesh method. The mass ratio, reduced damping and frequency ratio are kept invariant and the emphasis analysis is carried out for influence of the spacing ratio variety to lift forces, vibrating responses and wake vortex modes of three cylinders in regular triangle configuration. The following conclusions are obtained from this study:

(1) As the spacing ratios increasing, the mean lift coefficient of each cylinder trends to zero. The fluctuating lift coefficients of downstream cylinders are larger than those of upstream cylinder for all range of spacing ratios.

(2) In all L/D range, the fluctuation of the transverse displacement (Y) is very close to each other, and the fluctuating stream wise displacement of downstream cylinders (X) is larger than that of upstream cylinder.

(3) The maximum transverse oscillation amplitude of three cylinders can be reached 2.30D which is much larger than that of the single cylinder undergoing VIV with the same parameters setting. On the other hand, the maximum stream wise fluctuating amplitude of the downstream cylinders reaches 0.54D. It is indicated that the transverse oscillation amplitude of downstream cylinders significantly increased and the stream wise oscillation of upstream cylinder is unneglectable for vortex induced vibration of multi cylinder system.

List of Symbols

Re	Reynolds Number
St	Strouhal Number
C_L	Lift Coefficient
C_D	Drag Coefficient
ρ	Density
μ	Fluid Viscosity
k	Stiffness
ζ	Structural damping
m	Mass per unit length
l	Length
D	Diameter
U_∞	Fluid Viscosity
F_l	Lift Force
F_D	Drag Force
f	Lift Coefficient Frequency
U^*	reduced velocity

References

[1] Catalano P., Wang M., Iaccarino G., Moin P.," Numerical Simulation of the flow around a circular cylinder at high Reynolds number". International Journal of Heat and Fluid Flow (2003) 24, 463-469.

[2] Guilmineau E., Queutey P.," Numerical simulation of vortex induced vibration of circular cylinder with low mass damping in a turbulent flow". Journal of Fluids and structures 19 (2004), 449-466.

[3] Huang Z., Olson J.A., Kerekes R.J., Green S.I.," Numerical simulation of the flow around rows of cylinders", Computers and Fluids 35 (2006), 485-491.
[4] Lam K., Lin Y.F., Zou L., Liu Y.," Experimental study and large eddy simulation of turbulent flow around tube bundles composed of wavy and circular cylinders". International Journal of Heat and Fluid 31 (2010)32-44.
[5] Mittal S., Kumar V.," Flow induced vibration of circular cylinder in tandem and staggered arrangement", Journal of Fluids and Structures 15 (2001), 717-736.
[6] Ponta F.L., Aref H.," Numerical experiments on vortex shedding from an oscillating cylinder", Journal of Fluids and Structures 22 (2006), 327-344.
[7] Williamson C.H.K.," Three dimensional vortex dynamics in bluff body wakes", Experimental Thermal and Fluid Science 12(1996), 150-168.
[8] Ghias, R., Mittal, R., Dong, H.," A sharp interface immersed boundary method for compressible viscous flows", Journal of Computational Physics 225(2006), 528–553.
[9] Govardhan, R., Williamson, C.H.K.," Modes of vortex formation and frequency response for a freely vibrating cylinder", Journal of Fluid Mechanics 420(2000), 85–130.
[10] F. Saltara, A. D. Agostini Nato, J. I. Z Lopez. 2011. 3D CFD Simulation of Vortex induced Vibration of Cylinder. International Journal of Offshore and Polar Engineering. 21(3): 192–197.

INTERNATIONAL JOURNAL OF
COASTAL & OFFSHORE ENGINEERING
IJCOE No. 4 / Autumn 2016 (11-18)

Modeling and Control of Autonomous Underwater Vehicle (AUV) In Heading and Depth Attitude via PPD Controller with State Feedback

Soroush Vahid[1], Kaveh Javanmard[2]

[1]*PhD candidate, Semnan University, Soroush.vahid@semnan.ac.ir*
[2] *PhD candidate, Semnan University, kavehjavanmard@semnan.ac.ir*

ARTICLE INFO

Article History:
Received: 17 Jun. 2016
Accepted: 15 Dec. 2016

Keywords:
AUV
PPD (Proportional- Proportional – Derivative)
Pitch
Circulate
hydrodynamic

ABSTRACT

This paper focuses on design of AUV control system to control depth and pitch. Complexity and highly coupled dynamics, time-variance, and difficulty in hydrodynamic modeling and simulation, complicates the AUV modeling process and the design of proper and acceptable controller. A PD (Proportional- Derivative) controller, control the vehicle pitch and an outer P loop controller with state feedback will control the depth. The kinematic and dynamic equations will be extracted using various conditions such as the relative speed along the axis X (u), the speed along the axis Z (w), Pitch rate, forward position relative to the ground (x), depth (z), and the Pitch angle (Θ). Then we linearize the equations of motion of the AUV by choosing a suitable set of operating conditions. For effective control of the motion of AUVs, we need to design controllers based on the AUV's dynamic model. Through the control of propeller and fin's deflection, we can achieve the control system of AUVs. The simulation results indicate that developed control system is stable, competent, and efficient enough to control the AUV in tracking the two channels of heading and depth with stabilized speed.

1. Introduction

Autonomous underwater vehicle (AUV) is an unmanned submersible in different sizes. It is intended to provide scientists and researchers with simple, low-cost, medium and long-range, appropriate time response capability to collect environmental data. There are a lot of applications for AUVs, including oil industry, survey on underwater animals and plants, operations in dangerous waters, photometric survey, pipeline route survey, seabed mapping, environmental monitoring, chemical plume tracing [1], salvage and rescue requests, and so on [2]. Today the significance of AUVs can easily be understood if the Unmanned Underwater Vehicles (UUV) program for the US Navy is studied [3].

Derivation of AUV parameters is a difficult process and finally its validation demands to analyze practical test like two tank test [4] or telemetry under sea [5, 6]. However, at last, estimation of parameters has uncertainty and variation; therefore, the controller must be self-tuning and robust in counter to variation of AUV parameters and also unpredictable environmental disturbances.

Inherently, nonlinear dynamics of AUVs make it more difficult to exert commonly used linear control. The dynamic characteristics of an AUV are quite complex due to its high nonlinearity, time-varying dynamic behavior, uncertainties in hydrodynamic coefficients, and disturbances caused by sea currents and waves.

Throughout the years various models of control techniques have been proposed. This includes linear controllers [1, 2, 7, 8, 10, 23], which have performed satisfactorily; SMC controllers [11, 13], adaptive control [12, 13, 20], FLC (Fuzzy Logic Control) [14], predictive control [18– 19], static feedback control [25], and neural-network-based control [15–17] have also shown good robustness and tuning ability. Since almost all control methods have some pros and cons, a proper controller can be achieved by the combination of classical and modern intelligent method.

One of the most important disadvantages of linear controllers like LQR and LQG is that they are unable to account for the nonlinearities of the system, thus they can result in suitable performance and even instability in high maneuver treatments.

Also, neural network has some weak points that bind its improvement. It converges to a precise model with long training time and slow rate, which is not acceptable by many systems. Also, classical neural network does not qualify the main requirements such as fast response, less overshoot–undershoot.

SMC is an earlier method that is a good solution for nonlinear system but it can cause chattering on actuators, waste energy, and make fault on fins. However, there are some methods like combination with fuzzy or changing the sign functions by saturation function to reduce chattering.

The FLC is easy to use in industrial process because of its simple control structure, easy and cost-effective design [24]. However, FLC with fixed scaling factors and fuzzy rules may not give complete performance if the controlled plant has uncertainty and high nonlinearity [24]. Traditional FLC can have errors in steady state if the system does not have an inherent integrating property. Modern controllers are more robust to dynamic variations and can offer better performance index than classical controllers; however, they may require neat to exact models. The main aim of this paper is to develop an attitude control system of an AUV based on Myring hull profile via using PPD controller with state feedback. The goals are to:

1. Understand the general dynamic and kinematic of AUV by using MATLAB 2014
2. Achieve a suitable and simple controller to control heading and depth
3. Simulate the AUV's maneuvers (Snake and Spiral) and analyze the performance and accuracy of controller.

The advantage of using a PID controller is it is simple to implement and maintain, however, it is primarily applicable for linear time-invariant systems, though many extensions to nonlinear systems have been made such as [21] and references therein.

2. Model description

2.1. Coordinate systems and kinematic and dynamic equations of motion

Generally, the motion of an AUV can be introduced by six degrees of freedom (6-DOF) differential equations of motion [4], [22]. These equations are developed using two coordinate frames shown in Fig. 1. Six velocity components [u, v, w, p, q, r] (surge, sway, heave velocity, roll, pitch rate, yaw rate) are defined in the body fixed frame, while the earth-fixed frame defines the corresponding attitudes and positions [x, y, z, ϕ, θ, and ψ]. It is listed in Table 1. The axis is right-handed. The origin of the body-fixed coordinate system is center of mass.

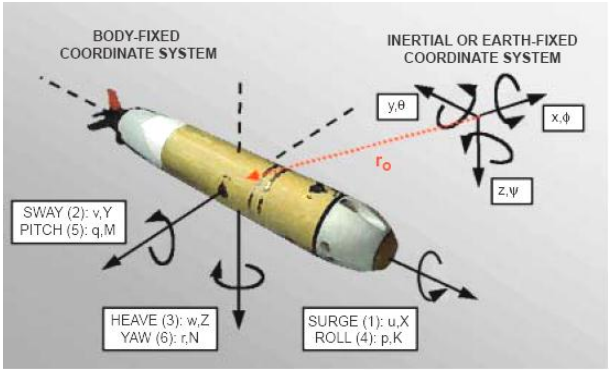

Fig. 1 Reference frame of AUV[16]

Table 1 Symbols used to describe 6-DOF

DOF	Motion	Forces and moments	velocity	Positions and Euler angles
1	surge	X	u	x
2	sway	Y	υ	y
3	Heave	Z	w	z
4	roll	K	P	ϕ
5	Pitch	M	q	θ
6	Yaw	N	r	ψ

The AUV motion is described by these vectors:

$$\eta = \begin{bmatrix} \eta_1 \\ \eta_2 \end{bmatrix} \quad \eta_1 = \begin{bmatrix} x \\ y \\ z \end{bmatrix} \text{position vector} \quad \eta_2 = \begin{bmatrix} \phi \\ \theta \\ \psi \end{bmatrix} \text{Euler angles vector} \tag{1}$$

$$\nu = \begin{bmatrix} \nu_1 \\ \nu_2 \end{bmatrix} \quad \nu_1 = \begin{bmatrix} u \\ v \\ w \end{bmatrix} \text{linear velocity vector} \quad \nu_2 = \begin{bmatrix} p \\ q \\ r \end{bmatrix} \text{angular velocity vector} \tag{2}$$

$$\tau = \begin{bmatrix} \tau_1 \\ \tau_2 \end{bmatrix} \quad \tau_1 = \begin{bmatrix} X \\ Y \\ Z \end{bmatrix} \text{forces vector} \quad \tau_2 = \begin{bmatrix} K \\ M \\ N \end{bmatrix} \text{moments vector} \tag{3}$$

It should be considered that in order to avoid singularity in circulation and transformation, Euler angles should be in this boundary:

$$\begin{aligned} &\mathbf{0} \le \psi < \mathbf{2}\pi \\ &{}^{-\pi}/_{2} < \theta < {}^{\pi}/_{2} \\ &-\pi < \phi \le \pi \end{aligned} \tag{4}$$

Transformation between these two coordinate systems is as follows:

$$J_1(\eta_2)=C_{z,\psi}^T * C_{y,\theta}^T * C_{x,\varphi}^T = \begin{bmatrix}\cos(\psi) & -\sin(\psi) & 0\\ \sin(\psi) & \cos(\psi) & 0\\ 0 & 0 & 1\end{bmatrix}\begin{bmatrix}\cos(\theta) & 0 & \sin(\theta)\\ 0 & 1 & 0\\ -\sin(\theta) & 0 & \cos(\theta)\end{bmatrix}\begin{bmatrix}1 & 0 & 0\\ 0 & \cos(\phi) & -\sin(\phi)\\ 0 & \sin(\phi) & \cos(\phi)\end{bmatrix} \quad (5)$$

$$J_1(\eta_2)=\begin{bmatrix}\cos\theta.\cos\psi & \sin\phi.\sin\theta.\cos\psi-\cos\phi.\sin\psi & \cos\phi.\sin\theta.\cos\psi+\sin\phi.\sin\psi\\ \cos\theta.\sin\psi & \sin\phi.\sin\theta.\sin\psi+\cos\phi.\cos\psi & \cos\phi.\sin\theta.\sin\psi-\sin\phi.\cos\psi\\ -\sin\theta & \sin\phi.\cos\theta & \cos\phi.\cos\theta\end{bmatrix} \quad (6)$$

For transformation of linear velocities, by the following matrix equation time rate of the displacements described with respect to world coordinate (earth-fixed) frame rates can be obtained as follows:

$$\begin{bmatrix}\dot{x}\\ \dot{y}\\ \dot{z}\end{bmatrix}=J_1(\eta_2).\begin{bmatrix}u\\ v\\ w\end{bmatrix} \quad (7)$$

Inversely, body coordinate frame velocities can be determined from world coordinate frame velocities in a similar fashion:

$$\nu_1=J_1^{-1}(\eta_2).\dot{\eta}_1 \quad (8)$$

Angular rates described with respect to body-fixed frame are transformed into the time rate of Euler angles by following non-orthogonal transformation matrix.

$$\dot{\phi}=p+q\sin(\phi)\tan(\theta)+r\cos(\phi)\tan(\theta) \quad (9)$$

$$\dot{\theta}=q\cos(\phi)-r\sin(\phi) \quad (10)$$

$$\dot{\psi}=\frac{q\sin(\phi)+r\cos(\phi)}{\cos(\theta)} \quad (11)$$

These three equation forms are represented in matrix notation:

$$\begin{bmatrix}\dot{\phi}\\ \dot{\theta}\\ \dot{\psi}\end{bmatrix}=J_2(\eta_2).\begin{bmatrix}p\\ q\\ r\end{bmatrix} \quad (12)$$

$$J_2(\eta_2)=\begin{bmatrix}1 & \sin(\phi)\tan(\theta) & \cos(\phi)\tan(\theta)\\ 0 & \cos(\phi) & -\sin(\phi)\\ 0 & \sin(\phi)\sec(\theta) & \cos(\phi)\sec(\theta)\end{bmatrix} \quad (13)$$

2.2 the final equations for the AUV's motion simulation

Six kinematic equations of motion are as follows:

$$\begin{aligned}\dot{\phi}&=p+q\sin\phi\tan\theta+r\cos\phi\tan\theta\\ \dot{\theta}&=q\cos\phi-r\sin\phi\\ \dot{\psi}&=(q\sin\phi+r\cos\phi)/\cos\theta\end{aligned} \quad (14)$$

$$\begin{aligned}\dot{x}&=u(\cos\theta\cos\psi)+\\ &\quad v(\sin\varphi\sin\theta\cos\psi-\cos\varphi\sin\psi)+\\ &\quad w(\cos\varphi\sin\theta\cos\psi+\sin\varphi\sin\psi)\\ \dot{y}&=u(\cos\theta\sin\psi)+\\ &\quad v(\sin\varphi\sin\theta\sin\psi+\cos\varphi\cos\psi)+\\ &\quad w(\cos\varphi\sin\theta\sin\psi-\sin\varphi\cos\psi)\\ \dot{h}&=-\dot{z}=u(\sin\theta)+\\ &\quad v(-\sin\varphi\cos\theta)+\\ &\quad w(-\cos\varphi\cos\theta)\end{aligned} \quad (15)$$

3. Controller Design:

Based on the linear model containing 3 states, we will design a proportional - derivative (PD) inner loop for controlling the pitch angle θ, and a proportional (P) outer loop for controlling the depth z.

3.1. Vessel Transfer Function

The first step to design control system for a vehicle is obtain its transfer function. At first, we want to achieve the inner loop transfer function that relating input stern angle (f_s) to the output vehicle pitch angle (Θ). According to kinematic and dynamic equations expressed, the inner Pitch loop transfer function is as follows:

$$G_\theta(s)=\frac{\theta(s)}{f_s(s)}=\frac{\frac{M_{f_s}}{I_y-M_q}}{s^2-\frac{M_q}{I_y-M_q}s-\frac{M_\theta}{I_y-M_q}} \quad (16)$$

Now we calculate outer depth loop transfer function that relating the input Pitch angle (θ_d) to vehicle depth (z). Under real conditions, the inner Pitch loop response is much faster than the outer depth loop so we can make equal with Θ. According to kinematic and dynamic equations expressed, the depth transfer function is as follows:

$$G_z(s)=\frac{Z(s)}{\theta(s)}=\frac{-\mu_1}{s} \quad (17)$$

3.2. Control Law

As denoted before, we want design a proportional-derivative (PD) inner loop for controlling the pitch angle Θ and a proportional (P) for controlling the depth z. According to the control law presented above, the inner loop control law is as follow:

$$\frac{f_s(s)}{e_\theta(s)}=-K_p(T_d s+1) \quad (18)$$

Where

$$e_\theta(error\ in\ pitch)=\theta_{des}(desired\ pitch)-\theta(actual\ pitch) \quad (19)$$

Kp is proportional gain and Td is derivative time constant. Because of difference between the vehicle stern angle and pitch angle the minus sign is applied. Positive stern angle create negative torque around Y

axis that force the vehicle diving down (negative pitch rate).
The control law for outer loop denoted as follow:

$$\Delta = \frac{\theta(s)}{e_z(s)} \tag{20}$$

Where

$$e_z = z_d - z \tag{21}$$

In view of the above control equations and considering the dynamic and kinematic characteristics of our AUV model, we designed the vehicle P-PD controller system blocks that shown as below :

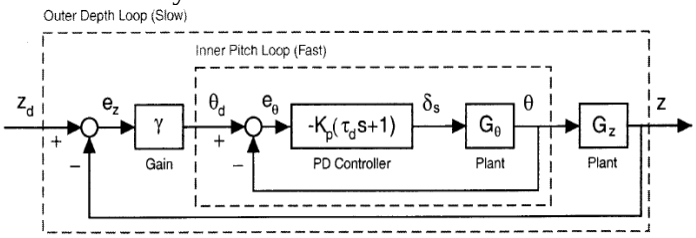

Fig.2 The vehicle controller system block

3.3. Controller design procedure:

Before choosing gain of the controller for a specified vessel we review the controller design.
We design our own controller to have a specified second order answer in natural frequency ω_n and damping coefficient ζ. For second order answer we have:

$$G(s) = \frac{K}{S^2+2\zeta\omega s+\omega^2} \tag{22}$$

3.4. Overshoot, ts, t_p

For choosing a suitable answer in a specified system, we must consider the %OS, setting time (t_s) and peak time (t_p).
Damping coefficient is a function of the percentage overshoot that calculated as follows:

$$\zeta = \frac{-\ln(\frac{\%OS}{100})}{\left[\pi^2+ln^2(\frac{\%OS}{100})\right]} \tag{23}$$

By damping coefficient and using the following equations the natural frequency can be obtained:

$$\omega = \frac{\pi}{T_P\sqrt{1-\zeta^2}} \tag{24}$$

$$\omega = \frac{4}{\zeta T_S} \tag{25}$$

3.5. Obtain the poles:

By considering the transfer function of second order answer and using the following the equation we can determine the location of poles in the coordinate plane.

$$S_{1,2} = \xi\omega \pm \omega\sqrt{1-\xi^2} \tag{26}$$

3.6. Pitch Controller

According to the vessel specifications:
Fin Lift= Mfs = -1575.9 kg.m2/s
Iy=469 kg/m2
Added Mass =Mq.= -458 kg.m2
Combined Term = Mq = 9826.2 kg.m2/s
Hydrostatic= Mθ = 13719.6 kg.m2/s2
And using $G_\theta(s)$, the Open loop transfer function is as follows:

$$G_\theta(s) = \frac{-1.7}{s^2+10.6s+14.8} \tag{27}$$

And the open loop poles are:

S1= -1.654 S2 =-8.945

Given that the vessels depth changes should not be too much the overshoot chosen around 0.05. By using $G_\theta(s)$, the value of $\zeta = 0.69$ and the value of T_d= 0.21 was obtained. By using the transfer function Root-Locus graph that we draw in MATLAB, the natural frequency ω_n=1.27 rad/sec and K_p=0.2604 obtained.

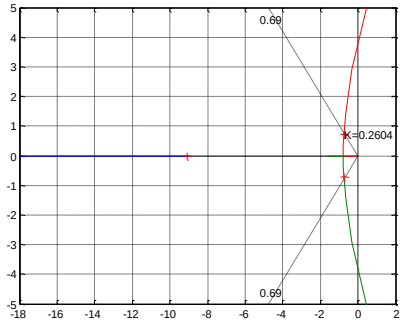

Fig.3 Transfer Function's Root-Locus Graph

3.7. Depth Controller

The depth transfer function adds third pole to the system. To ensure that the Pitch loop response is faster than depth loop response, the Pitch loop poles must be five-time interval away from the depth loop pole. For this we use a graph of the root-Lucas has achieved the appropriate Δ.

3.7.1. State feedback controller

In this section we use state feedback controller with trigger signal, u = -Kx. Where K is gain matrix and x is state matrix.
We have:

$$G_\theta(s) = \frac{-1.7}{s^2+10.6s+14.8} \tag{28}$$

And

$$G_z = {}^{-20}/_{s} \tag{29}$$

That gives us:

$$G_\theta(s) \times G_z = \frac{34}{s^3+10.6s^2+14.8s} \tag{30}$$

[A, B, C, D] = tf2ss ([34],[1 10.6 14.8 0]) (31)
gives:

$$A=\begin{bmatrix}-10.6 & -14.8 & 0\\ 1 & 0 & 0\\ 0 & 1 & 0\end{bmatrix} \quad B=\begin{bmatrix}1\\0\\0\end{bmatrix} \quad C=[0 \quad 0 \quad 34]$$

D= 0 (32)

The controllability matrix $P_C = [B \quad AB \quad A^2B]$ is calculated. If the P_c be a non-zero matrix, which means the system is state controllable.

For $\zeta = 0.69$ the poles are $\begin{cases} -0.338 \pm \mathrm{j}\, 0.355 \\ -10 \end{cases}$ and gives us $s^3 + 10.676s^2 + 7s + 2.4 = 0$.

When the matrix A is not in CCF form, we use $\bar{x} =$ Px to transfer the system to CCF form. Then the matrix P is $[0, 0, 1;\ 0, 1, 0;\ 1, 0, 0]$ and the effective system is $(-10.6, -14.8, 0)$. So the gain matrix is as following:

$$K = [10.676 + 1.09, , 7 + 0.52, 2.4 - 0\ ]$$

and

$$P = [11.766, 7.52, 2.4]$$

4. Simulation results

In order to demonstrate the effectiveness and stability of P-PD controller designed in this paper, we tested the maneuverability of selected AUV that we described the specification in section 3.6. One of the most important maneuvers that the underwater vessels do is circulation maneuver that is done by rudders level control. The maneuver is performed by applying a constant angle to the rudder, the submarine began to rotate and its height start decreases. Another important maneuver for submarines is dive and climb maneuvers. These maneuvers are done by using the elevator control levels. These maneuvers change the AUV's depth.

Two of the most important control levels in submarines are rudder control levels (dr) and elevator control levels (ds). The elevator control levels are control the depth means by applying positive and negative input the vessel will climb and dive. As shown in figures 4, 5 and 6 by using positive ds as controller input after 100 seconds the submarine depth changes from 0 to 43 meters. By applying negative ds in designed controller, the submarine start diving gently (figures 7, 8 and 9). By changing the rudder control elevators we can control the submarines heading. In the figures 10 and 11 by applying dr= 0.1 the submarines do the snake maneuver without any change in depth. The figure 12 shows the Snake maneuver in 3-D plot. By applying both rudder control levels and elevator control levels the submarines do the Circulate maneuver that shows in figures 13 and 14.

4.1. Simulation results for d_s= 0.1 (rad)

As mentioned before, for positive elevator control levels input the submarine began climb. The simulation results show below:

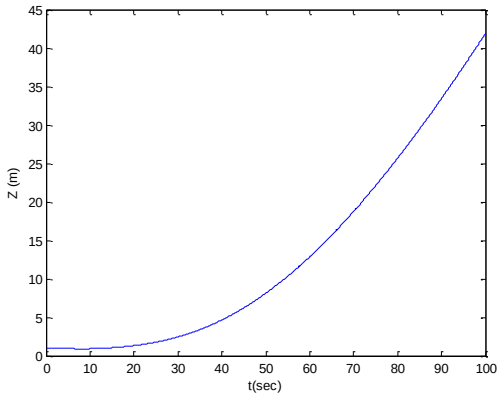

Fig.4 The depth change with time

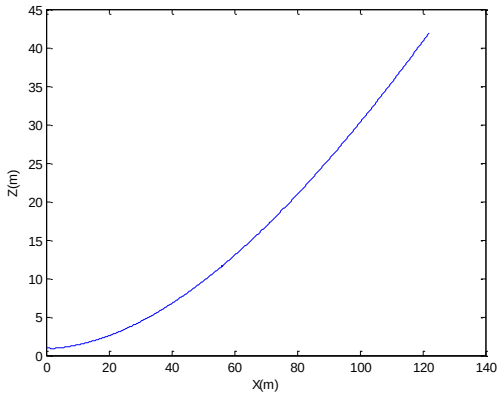

Fig. 5 Moving track in x-z plane

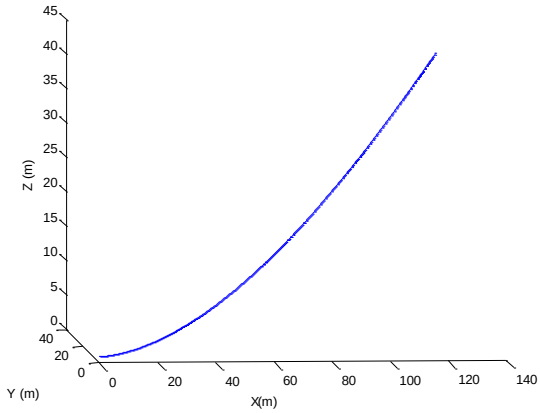

Fig.6 Depth changes in 3-D graph

4.2. Simulation results for d_s= -0.1 (rad)

For negative elevator control levels input the submarine began dive. The simulation results show below. As is evident from the results for asymmetric control orders, the AUV shown symmetric behavior, which represents the accuracy of the simulation.

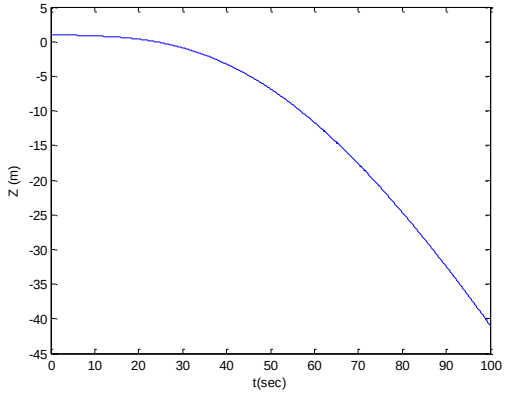

Fig.7 The depth change with ti

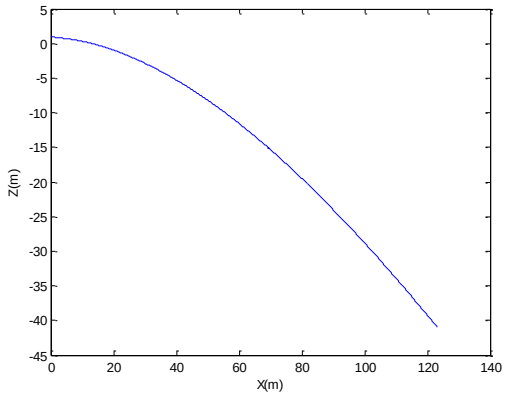

Fig.8 Moving track in x-z plane

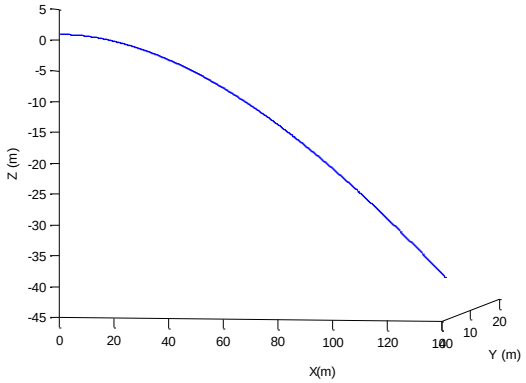

Fig.9 Depth changes in 3-D graph

4.3. Simulation results for dr= 0.1 (rad)

For the rudder control input, submarines began to rotate that the results are shown below:

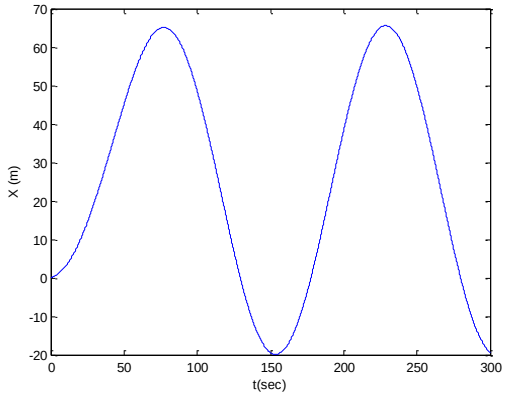

Fig.10 Snake move along the X axis

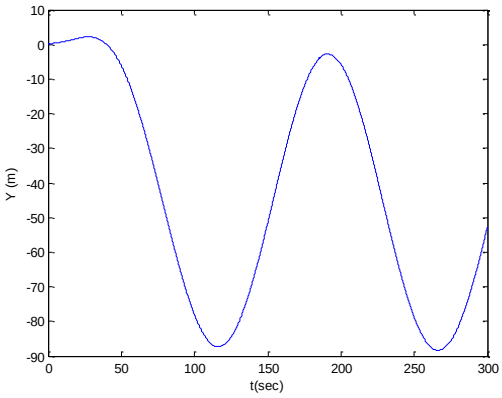

Fig.11Snake move along the Y axis

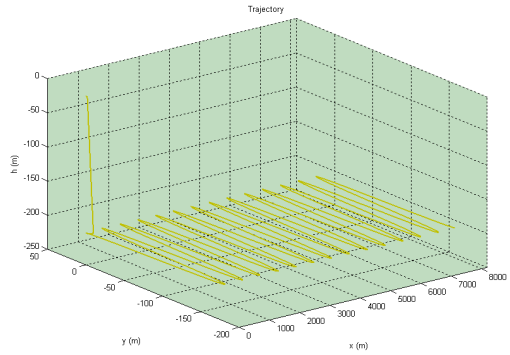

Fig.12The Snake maneuver in 3-D

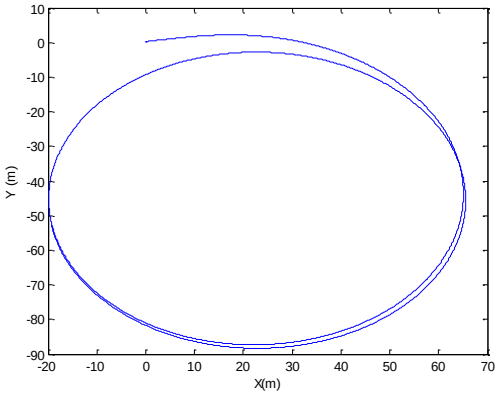

Fig.13 Circulation maneuver in Y-X plane

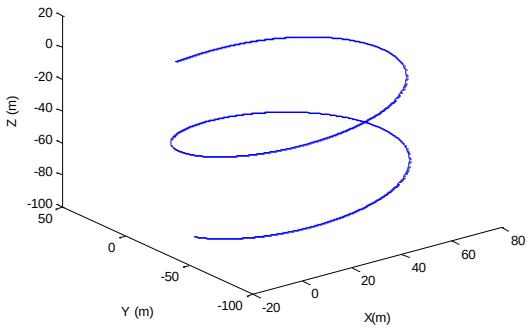

Fig.14 Circulation maneuver in 3-D

5. Conclusions

Control systems for depth and heading control of a small AUV were designed and tested in field. The P-PD with state feedback has proved useful in the development of the control systems for the AUV based on Myring hull profile. To construct the control system, a 6 DOF general mathematical model of underwater vehicles was derived, which is powerful enough to apply it to different kinds of underwater vehicles according to its own physical properties. Based on the general mathematical model, a simulation platform was established to test motion characteristics, stability and controllability of the vehicle. The control system was design based on AUV's mathematical model. After that we test the control system performance by dive, climb and circulation orders. The results show that the performance of controllers meets the requirement of performance and stability in both the vertical and horizontal planes.

6. References

[1] Farrell JA, Pang S, Li W, Arrieta R (2004) Biologically inspired chemical plume tracing demonstrated on an autonomous underwater vehicle, Man, and Cybernetics Conference, September 2004, Hague, Netherlands

[2] Yildiz O, Gokalp RB, Yilmaz AE (2009) A review on motion control of the Underwater Vehicles. In: Proceedings of electrical and electronics engineering, 2009. ELECO 2009, Bursa, 2009, pp 337–341

[3] UUV programs (2007) http://ftp.fas.org/irp/program/collect/ uuv.htm

[4] Prestero T Verification of a six-degree-of-freedom simulation model for the REMUS autonomous underwater vehicle, MSc/ME Thesis, Massachusetts Institute of Technology, 2001

[5] Geisbert JS Hydrodynamic modeling for autonomous underwater vehicles using computational and semi-empirical methods. Verginia Polytechnis Institute and State University, 2007

[6] Yue C, Guo S, Li M ,ANSYS fluent-based modeling and hydrodynamic analysis for a spherical Underwater robot. In: Proceedings of 2012 IEEE international conference on mechatronics and automation, pp 1577–1581, 2012

[7] Guo S, Mao S, Shi L, Li M ,Design and kinematic analysis of an amphibious spherical robot. In: Proceedings of 2012 IEEE international conference on mechatronics and automation, pp 2214–2219, 2012

[8] Herman P ,Decoupled PD set-point controller for underwater vehicles. J Ocean Eng 36(6–7):529–534,2009

[9] Fossen, T.I . Guidance and Control of Ocean Vehicle . New York: John Wiley & Sons. 1994

[10] Wadoo S, Kachroo , Autonomous underwater vehicles: modeling, control design and simulation. CRC Press, edn 1,2010

[11] Buckham BJ, Podhorodeski RP, Soylu S , A chattering-free sliding-mode controller for underwater vehicles with fault tolerant infinity-norm thrust allocation. J Ocean Eng, 35(16):1647–1659, 2008

[12] Qi X, Adaptive coordinated tracking control of multiple autonomous underwater vehicles. Ocean Eng 91:84–90, 2014

[13] Zeinali M, Notash L, Adaptive sliding mode control with uncertainty estimator for robot manipulators. Mech Mach Theory 45(1):80–90, 2010

[14] Jun SW, Kim DW, Lee HJ, Design of T-S fuzzy-model based controller for depth control of autonomous underwater vehicles with parametric uncertainties. In: 2011 11th international conference on control, automation and systems, ICCAS 2011, Gyeonggi-do, Korea, Republic of, 2011, pp 1682–1684,2011

[15] Kumar N, Panwar V, Sukavanam N, Sharma SP, Borm JH, Neural network-based nonlinear tracking control of kinematically redundant robot manipulators. Math Compute Model 53(9–10):1889–1901, 2011

[16] Fossen, T.I . Marine Control System . 2002

[17] Xu B, Pandian SR, Sakagami N, Petry F, Neuro-fuzzy control of underwater vehicle-manipulator systems. J Franklin Institute, 349(3):1125–1138,2012

[18] Medagoda L, Williams SB, Model predictive control of an autonomous underwater vehicle in an in situ estimated water current profile. Oceans, Yeosu, pp 1–8, 2012

[19] Steenson LV, Phillips AB, Turnock SR, Furlong ME, Rogers E, Effect of measurement noise on the performance of a depth and pitch controller using the model predictive control method. Autonomous underwater vehicles (AUV), 2012 IEEE/ OES, 1(8):24-27, 2012

[20] Mohan S, Kim J, Indirect adaptive control of an autonomous underwater vehicle-manipulator system for underwater manipulation tasks. Original Res Article Ocean Eng 54(1):233–243, 2012

[21] Cooney LA, Dynamic response and maneuvering strategies of a hybrid autonomous underwater vehicle in hovering. Thesis of Master of Science in ocean engineering, Massachusetts Institute of Technology, 2009

[22] Sgarioto D, Steady state trim and open loop stability analysis for the REMUS autonomous underwater vehicle. Defense Technology Agency, New Zealand Defense Force, DTA Report 254, 2008

[23] Yang C, Modular modeling and control for autonomous underwater vehicle (AUV). Thesis of master of engineering department of mechanical engineering national university of Singapore, 2007

[24] Lin FC, Adaptive fuzzy logic-based velocity observer for servo motor drives. Mechatronics 13:229–241, 2003

[25] Subudhi B, Mukherjee K, Ghosh S, A static output feedback control design for path following of

autonomous underwater vehicle in vertical plane. Ocean Eng 63:72–76, 2013

[26] A. Annamalai, A. Motwani, S.K. Sharma, R. Sutton,P. Culverhouse and C. Yang, A Robust Navigation Technique for Integration in the Guidance and Control of an Uninhabited Surface Vehicle, THE JOURNAL OF NAVIGATION, 68, 750–768, 2015

[27] Bong SeokPark, Adaptive formation control of under actuated autonomous underwater vehicles, Elsevier, Ocean Engineering96, 2015

[28] Thor I. Fossen, and Anastasios M. Lekkas, Direct and indirect adaptive integral line-of-sight path-following controllers for marine craft exposed to ocean currents, INTERNATIONAL JOURNAL OF ADAPTIVE CONTROL AND SIGNAL PROCESSING, 2015

[29] M. Kim, Hangil Joe and Son-Ceol Yu, Dual-loop robust controller design for autonomous underwater vehicle under unknown environmental disturbances, ELECTRONICS LETTERS, Vol. 52, No. 5, pp. 350–352, 2016

INTERNATIONAL JOURNAL OF
COASTAL & OFFSHORE ENGINEERING
IJCOE No. 4 / Autumn 2016 (19-25)

Oscillating Motion of Triangular Cylinder in a Viscous Fluid

Hamid Malah[1], Yuri Sergeyevich Chumakov[2], Sara Ramzani Movafagh[3]

[1]Department of Hydroaerodynamics, Institute of Applied Mathematics and Mechanics, Peter the Great St.Petersburg Polytechnic University, St. Petersburg, 194064, Russia; hamid.malah@gmail.com
[2]Department of Hydroaerodynamics, Institute of Applied Mathematics and Mechanics, Peter the Great St.Petersburg Polytechnic University, St. Petersburg, 194064, Russia; chymakov@yahoo.com
[3]Department of Civil Engineering and Applied Ecology, Institute of Civil Engineering, Peter the Great St.Petersburg Polytechnic University, St. Petersburg, 194064, Russia; sara.rm84@yahoo.com

ARTICLE INFO

Article History:
Received: 30 Aug. 2016
Accepted: 15 Dec. 2016

Keywords:
Triangular cylinder
Harmonic oscillation
Movable internal mass
Numerical simulation
OpenFOAM
Viscous fluid.

ABSTRACT

The system consisting of two rigid bodies in a viscous fluid is considered. The main body with mass M is placed in a viscous incompressible fluid, and the body with mass m moves inside the main body. This system is known as vibrobot which can be used in arbitrary inspection fluid mechanic objects such as oil industries pipes and tanks, as well as marine industries, medicine, etc. In this paper, the interaction between the vibrobot and viscous fluid is studied to achieve the motion laws of the vibrobot with the harmonic oscillation of internal mass. Also the flow structure around vibrobot and its effects on the hydrodynamic force acting on the vibrobot are investigated. Analyses are carried out by direct numerical simulation of the vibrobot motion in a viscous fluid by OpenFOAM package. Calculations are performed for the following combinations of control parameters; The ratio of the viscous fluid mass to the vibrobot mass $\mu_1=0.35$, the ratio of the internal mass to the vibrobot mass $\mu_2=0.325$ and dimensionless oscillation frequency f=1/5, when Reynolds number takes values in the range of $50<Re<250$. Calculations have been performed with different initial approximations, determined by different initial velocities of the incident flow.

1. Introduction

In this paper, numerical simulation of two-dimensional flow around a triangular cylinder subjected to a horizontal oscillating motion is considered in a viscous incompressible fluid. First of all, the history of studying bluff-body subjected to the fluid is expressed.

The liquid flow through a horizontal channel is a classical problem in the field of fluid mechanics. There are many cases where obstacles are in the path of fluid flows. When the flow separation due to an obstacle is very large, the obstacle may be classified as a bluff-body [1].

While a bluff-body in the fluid oscillates, or the body is fixed in the oscillating fluid, circulation around the body will be formed. Flow field around the bluff-body is usually divided into two main regions, i.e., an inner boundary layer and an outer flow field [2]. The study of two-dimensional oscillatory flow is important in the case of wave-induced forces on cylindrical structures and is the first step to understanding the complex three-dimensional structure of the wave. The flow due to loading and vibration of the cylinder in the viscous flow have been investigated during the recent decades [3].

A large number of numerical and experimental investigations on flow past variously shaped bodies have been accomplished by many researchers [4–8]. In contrast to the studies of the flow past a circular, square and rectangular cylinder, there are limited studies that focus on a triangular cylinder [9].

Wang et al. [10] experimentally presented a self-excited rotational oscillation on isolated and tandem triangular cylinders. Tatsuno [11] experimentally investigated the sample flow in the stable inner boundary layer near the triangular cylinder. In Tatsuno's paper, an equilateral triangular cylinder is used as a test body and oscillated sinusoidally in the fluid.

Numerical simulation of two-dimensional flow around a triangular cylinder subjected to a vertical oscillating motion in the channel were performed by Alawadhi [12]. In works of Jiahuang Tu et al. [13] the problem of two-dimensional fluid flow has studied numerically past the permanent and rotationally oscillating equilateral triangular cylinder with variable angle of

the incident, the Reynolds number, oscillating amplitude and oscillating frequency. Since the size of vibrobot is small, the Reynolds number is low. Therefore, flow around vibrobot is in the undetectable turbulence mode [14]. Thus, this problem is modeled as well as laminar mode. This principle can be used in medicine, arbitrary inspection fluid mechanic objects [15], etc.

Although many papers have been published on the flow around the different cylinders, lack of comprehensive study of triangular cylinders compared to round or square cylinders is obvious. Therefore, in this paper, a numerical simulation of the motion of the vibrobot in a viscous fluid is carried out by the OpenFOAM package with a simple harmonic oscillation on the triangular cylinder.

In this paper, a simplified plane setup of flow field and rigid body is assumed, that is symmetrical about the horizontal axis. The viscous and incompressible fluid is directed horizontally and the rigid triangular-shaped object (presenting one corner to the approaching flow and having one edge in the wake region) is allowed to move horizontally only. The main rigid body experiences (a) an inertia force due to the presence of a prescribed harmonic acceleration of a second internal mass, and (b) a horizontal force due to the presence of an outer fluid field with a certain coupling interface stress state. The central aim of the research presented in the paper is the characterisation and quantification of the induced fluid forces in order to determine the resulting locomotion of the object.

Geometrical Arrangement and Mathematical Equations

This section describes the model used for the rigid object and the surrounding flow. As the single degree of freedom of the object depends on the prescribed motion of the internal mass and the produced outer flow field, the solution of the Navier-Stokes equations is proposed in a moving coordinate system.

The system consisting of two rigid bodies in a viscous fluid is considered. The main body with mass M (corpus) is placed in a viscous incompressible fluid, and the body with mass m (internal mass) moves inside the main body. The triangular obstacle is in the middle of the considered zone. The dimensions of this zone are selected in a way which reduce boundary effects and satisfy the free-stream boundary condition and conform with other studies. The ratio of the vertical line of obstacle to the height of the channel is denoted by f which is called blockage ratio. To examine the effects of boundaries near obstacle on the characteristics of flow, $f = 0.033$ is reported as an acceptable value in many studies [1,2].

The internal mass interacts with the main body by a force which is generated by the actuator. The applied force to the internal mass, causes reaction force which effects to the main body. Reaction force changes the speed of the main body relative to the environment, hence resistance force of fluid changes in the opposite direction of the main body motion. Thus, adjusting the motion of the internal mass relative to the main body changes the external force acting on the main body in order to controlling the motion of the entire system. It is assumed that the internal mass has periodic longitudinal motion relative to the corpus which the entire system moves as a single assembly. Here, u_M is denoted as the velocity of the corpus, s and $z = \dot{s}$ are the motion and speed of the internal mass relative to the corpus, respectively that have been shown in Figure 1.

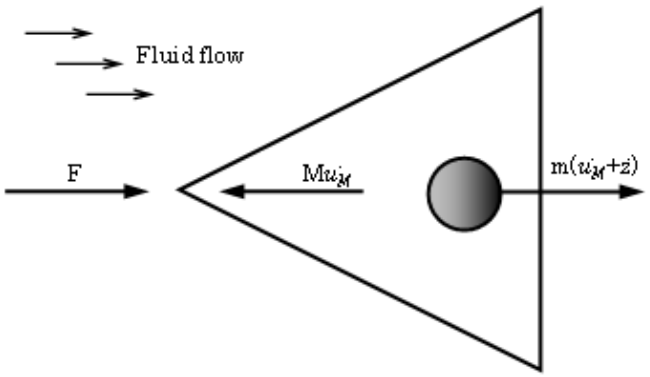

Figure 1: Schematic of the motion.

The equations of motion of the internal mass and corpus in a fixed coordinate system have the following form:

$$m(\dot{u}_M + \dot{z}) = -G \quad (1)$$

$$M\dot{u}_M = G + F \quad (2)$$

Here F is the horizontal force which is caused by the interaction between oscillating body and incident flow, G is the interaction force between the internal mass and corpus. By eliminating force G from equations (1) and (2), normalizing the speed by U_0 (velocity amplitude of the internal mass oscillations), normalizing the time by $RU_0{}^{-1}$ (R is the characteristic size of the corpus) and at last normalizing the force by $\rho_f RU_0{}^2$, the basic equation of entire system motion is obtained in the following form:

$$\dot{u}_M = -\mu_2\dot{z} + \mu_1(R^2/S)F \quad (3)$$

Here μ_2 is the ratio of the internal mass (moving mass) to the vibrobot mass ($\mu_2 = m/M + m$), μ_1 is the ratio of the viscous fluid mass (which occupies the same volume as the vibrobot) to the vibrobot mass ($\mu_1 = M_f/M + m$) and S is the cross sectional area of the corpus. Force F is determined by considering the motion of the fluid which surrounds the vibrobot.

The considered model is described by the non-steady Navier-Stokes system of equations. By normalizing the spatial coordinates, time and speed by R, $RU_0{}^{-1}$

and U_0 , respectively, vector form of the governing system of equations is as follows:

$$\partial U/\partial t + U.\nabla U = -\nabla p + \Delta U/Re \qquad (4)$$
$$\nabla.U = 0$$

Where $U = (u, v)$ is the dimensionless velocity, p is the dimensionless pressure and Re is Reynolds number. To solve this system of equations numerically, it is convenient to use the moving coordinate system associated with the vibrobot. To maintain the fluid motion in the form of a new non-inertial coordinate system, pressure should be defined as:

$$p = \tilde{p} + x\dot{\omega} \qquad (5)$$

Here the first term $\tilde{p}$ is the pressure in the fixed coordinate system, the second term $x\dot{\omega}$ is the contribution of the inertial components, $\dot{\omega}$ is the acceleration of the moving coordinate system and x is the dimensionless coordinate.
In the new coordinate system, on the boundary of the vibrobot, non-slip conditions (sticky fluid conditions) are defined:

$$u|_c = v|_c = 0 \qquad (6)$$

Where $u|_c$ is tangential velocity on the shell of triangular cylinder and $v|_c$ is normal velocity on the shell of triangular cylinder.
To determine the conditions at infinity, in this case, the acceleration of the moving coordinate system is written. For this purpose, the coordinate system should be switched to the moving coordinate system associated with the vibrobot. Hence the acceleration of the fixed coordinate system equals to the acceleration of the moving coordinate system plus acceleration of the coordinate system:

$$\dot{u}_M = \dot{\omega} + \dot{u}|_c \qquad (7)$$

Since $\dot{u}|_c = 0$, so

$$\dot{\omega} = -\mu_2\dot{z} + \mu_1(R^2/S)F \qquad (8)$$

At infinity, due to the fact that flow is potential, the boundary conditions are defined as follows:

$$\dot{u}|_\infty + \dot{\omega} = 0;\ \dot{u}|_\infty = -\dot{\omega} \qquad (9)$$

$$\dot{u}|_\infty = \mu_2\dot{z} - \mu_1(R^2/S)F \qquad (10)$$

With the assumption of potential flow at infinity, the condition of pressure can be obtained:

$$\partial p/\partial x\,|_\infty = -\dot{u}|_\infty = -\mu_2\dot{z} + \mu_1(R^2/S)F \qquad (11)$$

Calculated forces acting on vibrobot caused by viscous fluid in the dimensionless formulation are conducted by the following equation:

$$F_p = \int_S pnds - \int_S \bar{\sigma}.nds \qquad (12)$$

Where $\bar{\sigma}$ is the tensor of viscous stress, S is the vibrobot cross-sectional area and n is the outward normal vector to the vibrobot surface.
Thus, the obtained force vector F_p can be decomposed into the vertical component lift force F_y, and horizontal force F_x which consists of viscous resistance and inertial forces [3]. Inertial components are caused by acceleration of the fluid and consist of two parts; inertial added mass forces due to local acceleration near the cylinder and the Froude-Krylov forces, which is related with pressure gradient created in fluid which is used to simulate oscillating flow. In this case, Froude-Krylov forces can be calculated as:

$$F_{fk} = \int_S x\dot{\omega}\, nds \qquad (13)$$

Taking into account equation (13), the force F, acting on vibrobot in the moving coordinate system is calculated as:

$$F = F_x - F_{fk} \qquad (14)$$

Hence, the condition of pressure at infinity (equation (11)) can be rewritten as:

$$\partial p/\partial x\,|_\infty = -\dot{u}|_\infty = -\mu_2\dot{z} + \mu_1(R^2/S)(F_x - F_{fk}) \qquad (15)$$

The system of equations (4), (14) and (15) completely describe the motion of the vibrobot of any form in viscous fluid (and motion fluid around vibrobot) for a given motion law of the internal mass.
In the next step, the motion of a vibrobot with equilateral triangular cross-section is investigated in viscous fluid under harmonic oscillations of the internal mass:

$$\dot{z} = \sin(2\pi ft) \qquad (16)$$

Where $f = 1/KC$ is the dimensionless oscillation frequency. Here KC is Keulegan-Carpenter number [4].

Numerical solution

Discretization

This section describes the steps taken in order to solve the Navier-Stokes equations using an open-source framework (OpenFOAM).
Discretization of the computational domain is one of the solution processes [5]. In this work, block-structured grids is used which is built by a module in OpenFOAM known as blockMesh [6]. In Figure 2 a method for dividing the computational domain is presented.

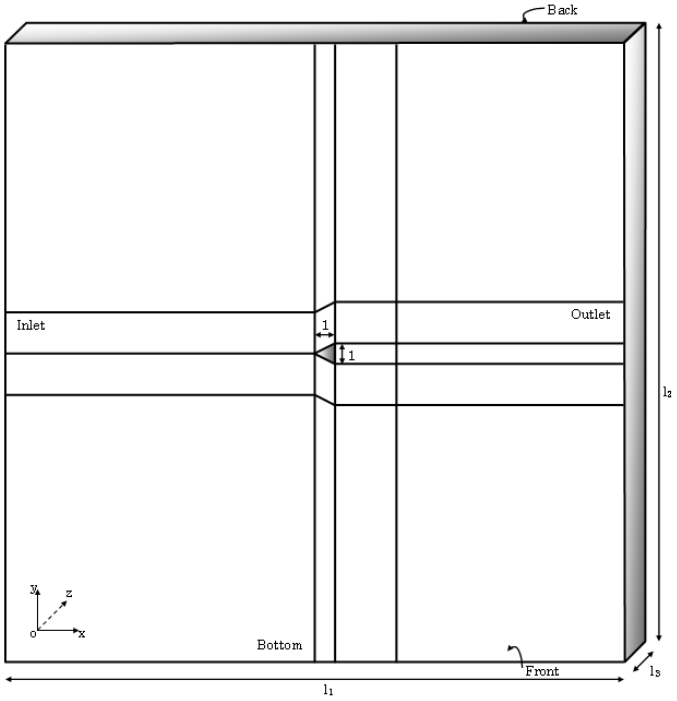

Figure 2: Division of the computational domain into blocks.

Here for two-dimensional calculations a domain with dimensions of $30 \times 30 \times 1$ is used where these values respectively point to length, height and width of the domain.

In Table 1 the values of the main parameters of the grids is presented. In Table 1; n is the total number of cells, N_m is the number of cells on the boundary of the cylinder, V_m is the volume of the smallest cells where is located in the boundary of the cylinder and V_{max} is the volume of the smallest cells where is located on the vicinity of the outer boundary of the domain. Additionally, in this table extremum values of indicators skewness M_s, non-orthogonality M_n and uniformity M_u for utilized grids, which are determined in accordance with the documentation of OpenFOAM package, are presented.

Table 1: Parameters of the computational grids.

Parameters	n	N_m	V_m	V_{max}	M_n	M_s	M_u
m_1	27652	197	24 exp.(-4)	0.22	30	0.37	0.46
m_2	56734	131	8 exp.(-4	0.5	30	0.37	0.46

In OpenFOAM package, discretization of motion equations process is carried out by the finite volume method (FVM) in the Cartesian coordinate system. For this purpose, discrete values of velocity components and discrete values of pressure are located in the center of cells [7].

To minimize the errors due to the first order approximation, the time step (τ) in all the calculations is chosen from the condition $C^{max} < 0.1$. Here, C^{max} is the maximum Courant number [8]. Courant number in the OpenFOAM package is determined by the formula:

$$C = (|U_P|\tau)/\delta \tag{17}$$

Where $|U_P|$ is the velocity modulus in the cell, δ is the cell size in the direction of the velocity.

Boundary conditions

At the input and the output boundaries of the domain non-reflecting boundary conditions are set as:

$$\begin{cases} u = u_\infty;\ \partial p/\partial x = -\dot{u}_\infty; & u_0 > 0 \\ \partial p/\partial x = 0;\ p = -\dot{u}_\infty x; & u_0 \le 0 \end{cases} \qquad v = 0 \tag{18}$$

They are combined with the conditions of equation (15) which are defined on the boundary at infinity. Conditions depend on variable u_0, which defines flow direction relative to the outward normal vector at the boundaries.

At the top and the bottom boundaries non-slip conditions are laid down:

$$\partial p/\partial y = 0;\ \partial u/\partial y = 0;\ v = 0 \tag{19}$$

At the boundary of the cylinder non-slip conditions for the velocity are set:

$$u = v = 0 \tag{20}$$

The condition of pressure is:

$$\partial p/\partial n = 0 \tag{21}$$

At the front and the back boundaries of the domain special *"empty"* boundary conditions are given which are provided in OpenFOAM package in the case of non-responding calculations in an arbitrarily given direction. Required initial conditions in the entire computational domain, utilize the values of velocity and pressure corresponding to the undisturbed flow.

Verification

Due to lack of insufficient quantifications from the numerical solutions of triangular cylinders, and assuming that OpenFOAM is a mature solver, here in Figure 3, the flow pattern obtained by calculations in the OpenFOAM package is compared with the experimental results reported by Tatsuno [9]. In Tatsuno's study, glass micro-particles were suspended in a fluid to visualize the fluid flow and he also noted that $\vartheta = 0.53\ [cm^2/\mathrm{s}]$, that ϑ is kinematic viscosity. The results show that the entire structure of the flow obtained from the calculations and from the experiment are symmetrical about the axis of oscillation and as already seen, these flow patterns coincide qualitatively with each other.

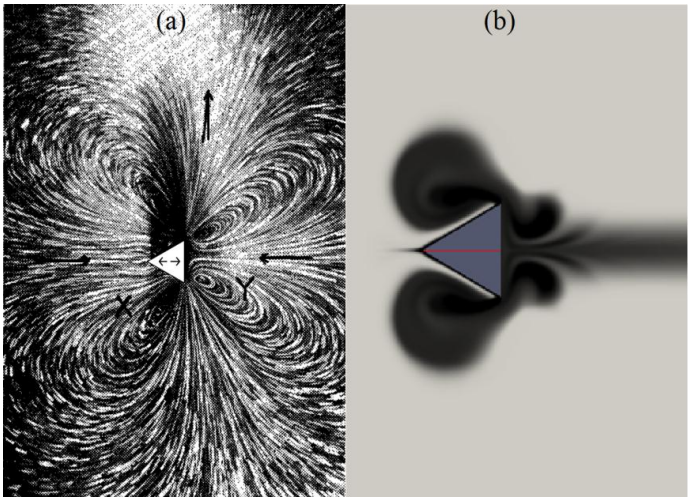

Figure 3: Flow pattern of a triangular cylinder in viscous fluid for $\upsilon = 0.53\ [cm^2/s]$. a) Experimental result reported by Tatsuno, b) Numerical solution using OpenFOAM package in this paper.

Results and Discussion

This section presents the results on the locomotion in a flow at small Reynolds numbers. Calculations have been performed for the following combinations of control parameters: $\mu_1 = 0.35$, $\mu_2 = 0.325$, and $f = 1/5$, in the range of $50 < Re < 250$. Results of calculations have been obtained with different initial approximations, determined by different initial velocities of the incident flow.

In the studied range, three stable modes of vibrobot motion were found. To describe these modes it is convenient to introduce the following motion characteristics: U_{ave} is the average speed of motion and η is the performance indicator of motion, describing the energy consumption of the body motion caused by internal motion. They are defined by the following equation:

$$\eta = N_0/N_{vbr}\ \% \qquad (22)$$

Here N_0 is the minimum power required to move the body with speed U_{ave} (values N_0 for different Re obtained according auxiliary calculations), N_{vbr} is the consumed power to move the vibrobot with speed U_{ave}.

Changes in characteristics of vibrobot motion with increasing Reynolds number for different modes of motion are shown in Figure 4 and Figure 5. In the zone of low Reynolds numbers ($Re < 160$) unique periodic symmetry was observed about the axis of oscillation (regime S), which determines the direction of motion of the vibrobot toward the positive direction of the x-axis. Increasing Reynolds number leads to increase in the average values of both speed and performance indicator of the vibrobot motion.

For range of Reynolds number greater than 180 two new regimes arise; for $180 < Re < 210$ quasi-periodic regime K_1 when $\vartheta = 48\ [cm^2/s]$ is observed and for $Re > 210$ quasi-periodic regime K_2 when $\vartheta = 46\ [cm^2/s]$ is observed.

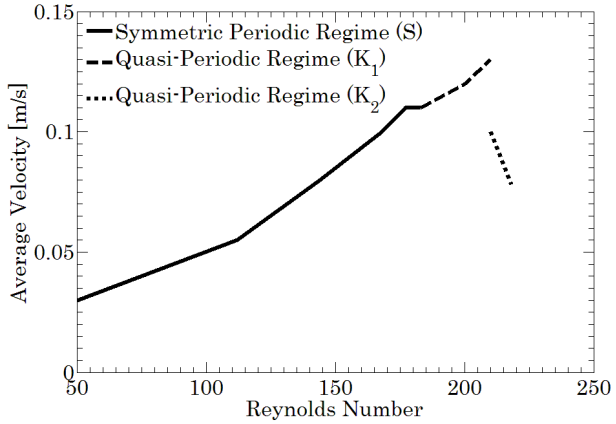

Figure 4: Motion characteristics of vibrobot; Dependence of average velocity on Reynolds number.

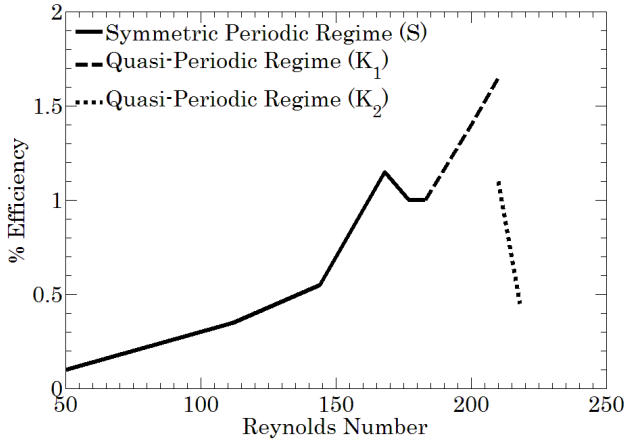

Figure 5: Motion characteristics of vibrobot; Dependence of efficiency on Reynolds number.

Moreover, in Figure 6, the flow patterns of different quasi-periodic modes are shown for a half period. Also schematic of velocity amplitude of the vibrobot versus time for regime K_1 when $\vartheta = 48\ [cm^2/s]$ is displayed in Figure7.

In Figure 8, velocity amplitude of the vibrobot versus time for two different modes with different initial conditions are shown. These modes are obtained for regime K_2 when $\vartheta = 46\ [cm^2/s]$. It is obvious that with different initial conditions, final velocity amplitudes are the same.

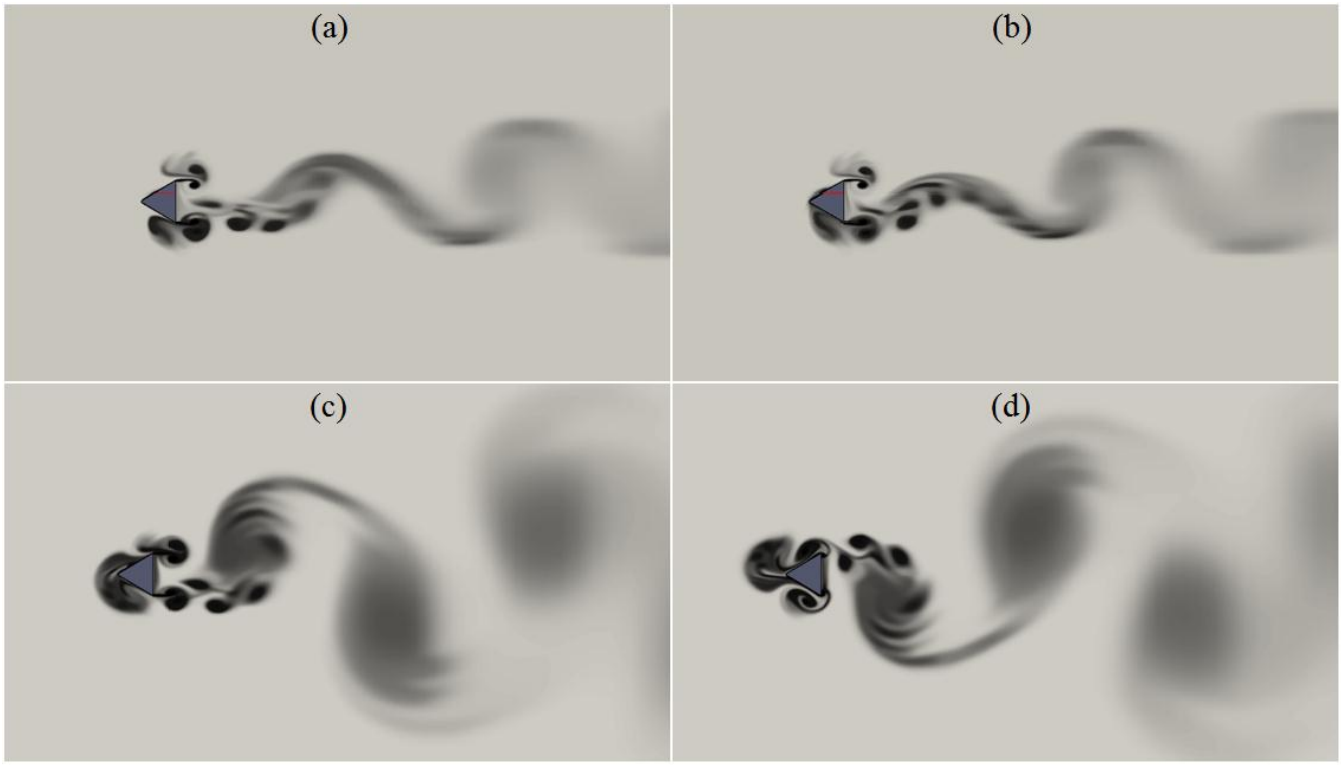

Figure 6: Flow pattern of a triangular cylinder in viscous fluid for a half period quasi-periodic modes. (a,b): Regime K_2 when $\upsilon = 46\ [cm^2/s]$ (c,d): Regime K_1 when $\upsilon = 48\ [cm^2/s]$.

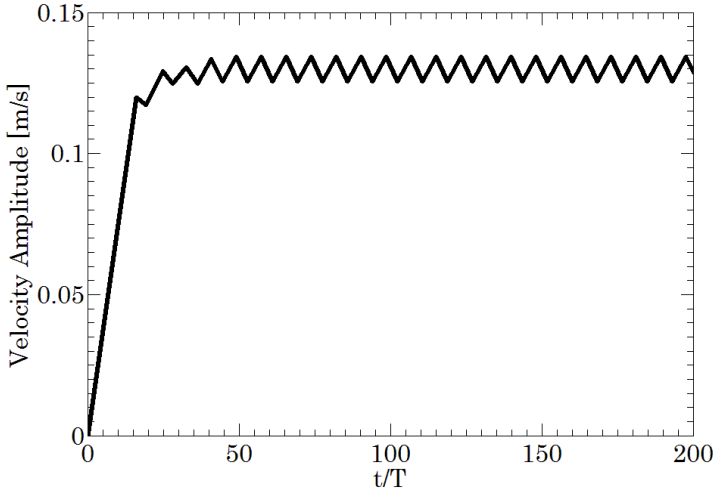

Figure 7: Velocity amplitude of the vibrobot versus time for regime K_1 when $\upsilon = 48\ [cm^2/s]$.

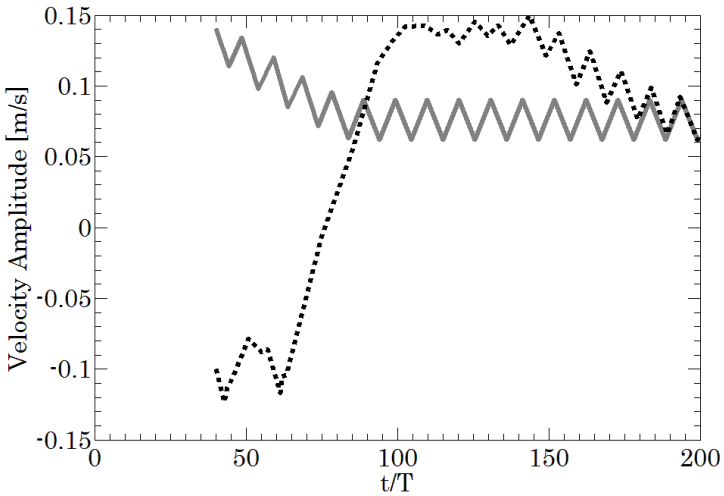

Figure 8: Velocity amplitude of the vibrobot versus time for two different initial conditions for regime K_2 when $\upsilon = 46\ [cm^2/s]$.

Summary and conclusions

In this paper, a triangular cylinder in a viscous fluid is considered which is under harmonic oscillations of the internal mass. The following results have been obtained:

1. The selected form for body under a given motion law of the internal mass for $f = 1/5$ (investigated oscillation frequency) allows to provide conditions for directional steady motion in a viscous fluid in the range of $50 < Re < 250$.

2. The direction of motion in most of the studied range is determined by the initial conditions, which by using that, different steady modes of straight motion of vibrobot can be realized, both in the positive direction of the x-axis and toward the negative direction of the x-axis but they have different effects.

3. Most of the observed flow regimes belong to the category of quasi-periodic modes, i.e. the full period of the vibrobot is equal to several periods of oscillation of the internal mass. Basic periodic flow regime turns into quasi-periodic flow regime at $Re > 180$. This is primarily due to the fact that with increasing Reynolds number, hydrodynamic force distinct the temporal harmonic oscillation from the main harmonic oscillation.

4. Maximum efficiency of motion, for the given parameters, does not exceed 1.7%. This value is achieved for the quasi-periodic regime K_1 for $Re = 210$. At high Reynolds numbers, less efficient modes have been observed, which gradually turn into chaotic.

All these results provide a basis for understanding the interaction between vibrobot and viscous fluid and it is a platform for studying more complex laws of motion in order to maximize the effectiveness of such devices.

References

[1] Abbassi, H., Turki, S., and Ben Nasrallah, S., ‘‘Numerical investigation of forced convection in a plane channel with a built-in triangular prism,’’ Int. J. Therm. Sci., Vol. 40, pp. 649–658, 2001.

[2] Tatsuno, M., and Bearman, P. W., ‘‘A visual study of the flow around an oscillating circular cylinder at low Keulegan-Carpenter numbers and low Stokes numbers,’’ J. Fluid Mech., Vol. 211, pp. 157–182, 1990.

[3] Koopmann, G.H., ‘‘The vortex wakes of vibrating cylinders at low Reynolds numbers,’’ J. Fluid Mech., Vol. 28, pp. 501–512, 1967.

[4] Davis, R. W., and Moore, E.F., ‘‘A numerical study of vortex shedding from rectangles,’’ J. Fluid Mech., Vol. 116, pp. 475–506, 1982.

[5] Saha, A. K., Biswas, G., and Muralidhar, K., ‘‘Three-dimensional study of flow past a square cylinder at low Reynolds numbers,’’ Int. J. Heat Fluid Flow., Vol. 24, pp. 54–66, 2003.

[6] Srigrarom, S., and Koh, A. K. G., ‘‘Flow field of self-excited rotationally oscillating equilateral triangular cylinder,’’ J. Fluids Struct., Vol. 24, pp. 750–755, 2008.

[7] Williamson, K., ‘‘Sinusoidal flow relative to circular cylinders,’’ J. Fluid Mech., Vol. 155, pp. 141–174, 1985.

[8] Ghadimi, P., Djeddi, S.R., Oloumiyazdi, M.H., and Dashtimanesh, A., ‘‘Simulation of flow over a confined square cylinder and optimal passive control of vortex shedding using a detached splitter plate,’’ Scientia Iranica transaction B- Mech. Eng., Vol. 22, pp.175–186, 2015.

[9] Alonso, G., Sanz-Lobera, A., and Meseguer, J., ‘‘Hysteresis phenomena in transverse galloping of triangular cross-section bodies,’’ J. Fluids Struct., Vol. 33, pp. 243–251, 2012.

[10] Wang, S., Zhu, L., Zhang, X., and He, G., ‘‘Flow Past Two Freely Rotatable Triangular Cylinders in Tandem Arrangement,’’ J. Fluids Eng., Vol. 133, 081202, 2011.

[11] Tatsuno, M., ‘‘Circulatory streaming in the vicinity of an oscillating triangular cylinder,’’ J. Phys. Soc. Japan., Vol. 38, pp. 257–264, 1975.

[12] Alawadhi, E. M., ‘‘Numerical Simulation of Fluid Flow Past an Oscillating Triangular Cylinder in a Channel,’’ J. Fluids Eng., Vol. 135, 041202, 2013

[13] Tu, J., Zhou, D., Bao, Y., Han, Z., and Li, R., ‘‘Flow characteristics and flow-induced forces of a stationary and rotating triangular cylinder with different incidence angles at low Reynolds numbers,’’ J. Fluids Struct., Vol. 45, pp. 107–123, 2014.

[14] Hémon, P., and Santi, F., ‘‘On the Aeroelastic Behaviour of Rectangular Cylindres in Cross-Flow,’’ J. Fluids Struct., Vol. 16, pp. 855–889, 2002.

[15] De, A. K., and Dalal, A., ‘‘Numerical simulation of unconfined flow past a triangular cylinder,’’ Int. J. Numer. Methods Fluids., Vol. 52, pp. 801–821, 2006.

[16] Morison, J. R., Johnson, J. W., and Schaaf, S. A., ‘‘The Force Exerted by Surface Waves on Piles,’’ J. Pet. Technol., Vol. 189, pp. 149–154, 1950.

[17] Justesen, P., ‘‘A numerical study of oscillating flow around a circular cylinder,’’ J. Fluid Mech., Vol. 222, pp. 157–196, 1991.

[18] Issa, R. I., ‘‘Solution of the implicitly discretised fluid flow equations by operator-splitting,’’ J. Comput. Phys., Vol. 62, pp. 40–65, 1986.

[19] Versteeg, H. K., and Malalasekera, W., *An introduction to computational fluid dynamics: the finite volume method*, Longman, 2007.

[20] Shademani, R., Ghadimi, P., Zamanian, R., and Dashtimanesh, A., ‘‘Assessment of Air Flow over an Equilateral Triangular Obstacle in a Horizontal Channel Using FVM,’’ J. Math. Sci. Appl., Vol. 1, pp. 12–16, 2013.

[21] Ferziger, J. H., and Peric, M., *Computational Methods for Fluid Dynamics*, Springer, 2002.

INTERNATIONAL JOURNAL OF
COASTAL & OFFSHORE ENGINEERING
IJCOE No. 4 / Autumn 2016 (27-32)

Wave Run-Up and Stress Imposed On a Permeable Coastal Bed Sample of the Caspian Sea

Mojtaba Zoljoodi[1]

[1] *Faculty member and assistant professor, Iranian National Institute for Oceanography and Atmospheric sciences (INIOAS), email: zoljoodi@inio.ac.ir*

ARTICLE INFO

Article History:
Received: 4 Jul. 2016
Accepted: 15 Dec. 2016

Keywords:
Permeable bed,
wave run up and run down,
Caspian Sea bed,
injection and suction phases

ABSTRACT

This research aims to reconsider the wave run-up and eulerian schematic of flow contours and the fluid movement path in the sediment sample gathered from southern Caspian Seashore bed, using experimental method in wave flume. The general characteristics of flow depend on the kind of bed structure, the bed shear tension, vertical velocity profile and the permeation velocity, could be changeable. While, because the increasing of water surface height, the fluid penetrates bed, and consequently the suction phase happens within the bed. Through this condition the flow contours approach the bed and the mean velocity accelerates near the bed, and then the tension rises about 3 times.Because the decreasing of water surface height, the fluid permeates out from the bed and the injection phase happens, so that the flow contours get away from the bed and the mean velocity falls down near the bed , so the tension slakes about 80%. This studyuses 3 waves with a sharpness ranges from 0.01 to 0.06.The wave run-up has been measured using the wave height recorders which have been installed on a ramped shore with a constant slop of 1:5. By using a camera under water and also color injection into the bed, the flow contours and movement path of fluid in the sample of Caspian Sea, the permeability ranges have been drawn. Meantime, the flow velocity is estimated in two positions including near the bed surface and the bed deep. Through the relative non-dimensional permeation velocity ($\tilde{U}$=Vz/Vx), it is shown that in a given wave frequency, by increasing velocityin the suction phase, the tension imposed on the bed is risen up, whiles by increasing the relative velocity in injection phase the tension imposed on the bed is fallen down.

1. Introduction

A Fluid current depends on the bed permeability over a porous surface such as, sandy bed of Caspian Sea. For calculation of the bed permeability, the hydraulic conductivity of bed sediments and hydraulic gradient of fluid are of high importance. Regarding the literature reviews on the permeability experimental studies except to this research and an investigation done by Beidokhti et al, (2003) [1], there is a little developed works in this study field.Conley and Inman (1992) [2] have done some field studies about the effects of bed structure on the wave behavior, also they found that the formation of the shore bed depends on the tension variations. The effect of bed permeability on wave characteristics over a shore has been studied by Conley and Inman (1994) [3]. One of the results derived by analysis of water flows over a permeable bed that is conducted by Conley and Inman (1994) [3] and Beidokhti et al, (2003) [1], has been shown in Figure 1.

Regarding this graph, it is notable that the high suction velocity could lead to increase the tension imposed on the bed and conversely, through the high injection velocity, the tension could be decreased near the bed. Meantime, the suction velocity indicates a direct connection to the permeability of bed and pressure gradient, whiles there is a converse relation with the fluid viscosity. Conley and Inman`s experiment is done on a horizontal bed through fluctuation of the fluid Head, with a constant frequency.

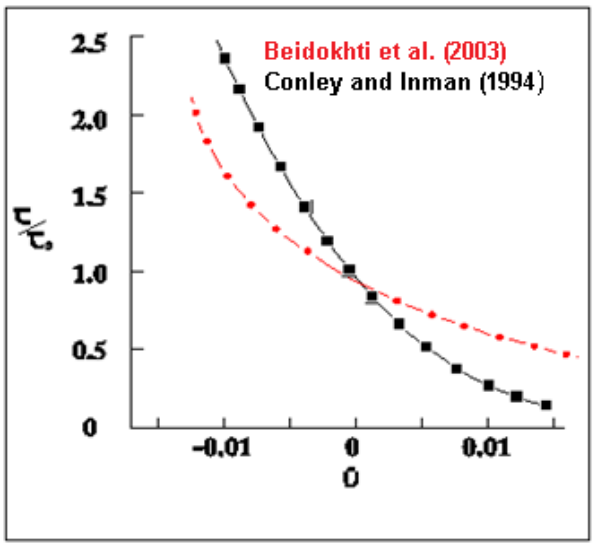

Figure 1.the results derived by Beidokhti et al.,(2003) and Conley and Inman (1994).
high suction velocity could lead to increase the tension imposed on the bed and conversely, through the high injection velocity, the tension could be decreased near the bed.

Villarroel-Lamb et al, (2014) [4] conducted the series of experiments through a Hunt-type runup formulation and Indicated that there is a clear relationship between bed permeability and the maximum wave run-up. Hughes (2004) [5] developed a study to provide an estimation technique that was as good as existing formulas for breaking wave run-up and better at estimating nonbreaking wave run-up. For irregular waves breaking on the slope, a single formula for the 2% run-up elevation proved sufficient for all slopes in the range $2.3 \leq \tan\alpha \leq 1.3$. Antonia et al. (1990) [6], conducted some researches on the effect of surface suction to vortex boundary layer and separation event. This experiment investigates the effects of suction and injection phases on the surface tension of a ramped bed of Caspian Sea sediments affected by run-up and rundown. These effects on the wave run-up also are considered. According to this fact that in the experimental models to determine the extent of run-up and rundown, and in general the hydraulic reactions of breakwaters and shore structures, the permeability of bed is assumed to be ignorable because of the selection of the common experimental scales, thus, conducting such experiments on the samples provided from Caspian Sea shore bed, in order to consider the effects of the bed permeability could be necessary.

2- Physical foundations

While the waves approach to the shallow zone of sea (near the shoreline), they rise and consequently breakdown after collision to the shoreline. Following the wave-break, and the resulted balance with hydrostatic force, the water surface gets raised. The rising of water surface is called run-up (Figure 2).

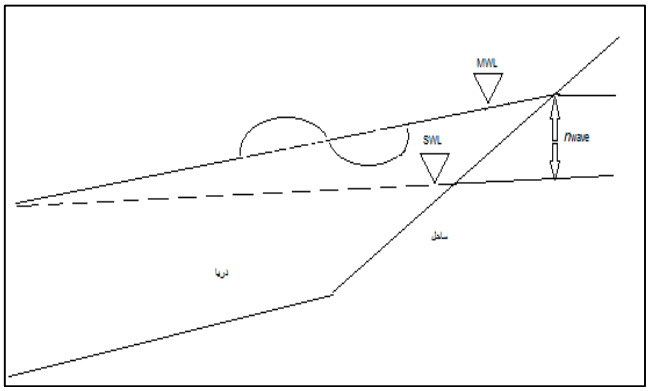

Figure 2. Wave Run-up

The run-up hydraulic reaction of wave occurs during the wave collision to the shoreline. At this moment, the waves – because of having the kinetic energy- climb the ramped shore, and so, the vertical distance of water level fluctuation on top of the water table, is the so called the wave run-up (Figure 3-A).
When, the kinetic energy fall to zero , by the existing potential energy and the fluid integration, the wave moves downward from shoreline and the hydraulic reaction of wave rundown occurs. The vertical distance of water level fluctuation under the water table, is the so called the wave rundown (Figure 3-B).

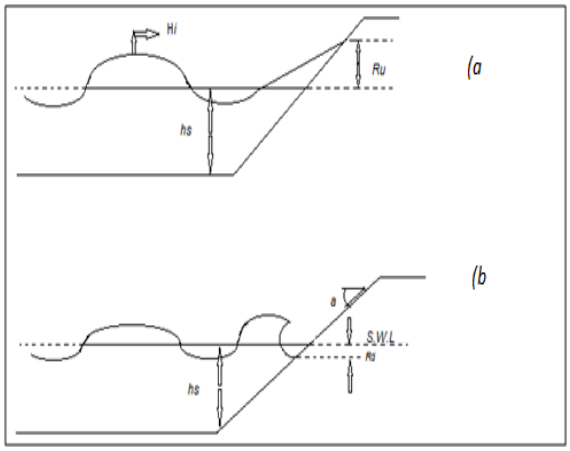

Figure 3; a) wave run-up, b) wave run-down

Wave run-up and rundown impose the positive and negative pressure on the shore bed respectively. In the case the bed is permeable, through the wave movement toward shore and the hydraulic reactions of wave run-up and rundown on the ramped shore, some currents could be generated within the shore bed. The above mentioned currents penetrate the bed, but the interactions with the objects over the bed and the consequent damping, limit their penetration by a certain deep.
The water pressure gradient is considered the cause of above current, and the generated velocity gradient will be different based on the bed gradation and permeability. Friction of shore currents by the bed permeability leads to lose the wave energy as

reduction of run-up and rundown and also manner of wave break.To show the manner of wave break and the wave interaction with the ramped shore, the similarity parameter of wave break or the non-dimensional number of Airybaren has been used (Figure 4).

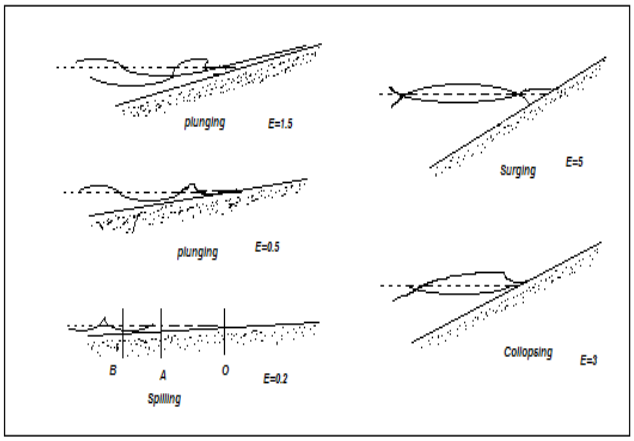

Figure 4; Breaking similarity parameter

The similarity parameter of break is defined as follows: $\xi = \frac{\tan a}{\sqrt{S}}$ (1)

In the above equation, "S" as the sharpness of wave is defined by the following relation: $S = \frac{H}{L}$ (2),

and here "H" is the height of wave and "L" is the length of wave.

3- Experimental phases

To consider the permeability effect of Caspian Sea shore bed on hydraulic reactions of wave, the laboratory model has been applied. The wave flume dimensions are as follows: 45m length, 6m width and 1.5m depth. In order to prevent production of the horizontal waves, the flume is divided into 3 sections so that the middle flume has 26m length, 1.5m width and 1.5m depth. All experiments have been done on an artificial shore at the outset of middle flume. The waves are generated by using a piston paddle installed at the end of flume. The artificial shore has been made inside a box with dimensions of 2.5m length, 1.5m width and 0.65m depth and a constant slop of 1:5.This box is filled by the gravels gathered from southern coasts of Caspian Sea with different permeability. The sandy and gravel materials are taken in consideration based on the soil mechanic experiments by 3 different permeability (including 3 water conductivity coefficients: 0.079, 0.075 and 0.079 cm/s). During the experiments, 6 waves have been generated and moved towards the artificial shore. The waves which hit the shore have sharpness ranges from 0.01 to 0.06. During the interaction of wave and shore, a camera has been installed under water on the shore bed, to track and record the fluid current which is colored. The velocity of the current has been estimated by measuring the relation between time and distance of the current movement. To record the wave run-up and rundown, 2 wave height recorders have been installed on the ramped shore bed. In total about 65 experiments have been done that their outputs are shown by graphs and tables.

3-1- Measurement errors

The measurable parameters through the experiments include: wave run-up, wave height, waves frequency, current velocity within the bed. The measurement errors of above parameters during the experiments have been shown in table 1.

Table 1; The errors derived through measurements in the experiments

three depths of 5 , 10 and 15 cm.	The flow speed in the bed (suction and injection)	The flow speed of wave run-up and run-down	Wave period	Wave height	Wave run-up	Parameters
V1 , V2, V3	Uzs , Uzi	UR , Ud	T	Hw	R	variable
cm/s	cm/s	cm/s	s	cm	cm	unit
0/04±	0/02±	0/025±	0/02±	0/03±	0/2±	Error

4- The Findings

4-1- Effect of bed permeability on the wave run-up

In this section, the graphs of the wave relative run-up (as non-dimensional, R/H) based on the wave sharpness and the similarity break parameter, has been shown. Also, the current velocity of bed and the effects of injection and suction velocity on generated tension have been considered.

By the figure 5, the wave relative run-up according to the wave sharpness is shown, for the Caspian Sea permeable beach through the measurement points and their fitting line.

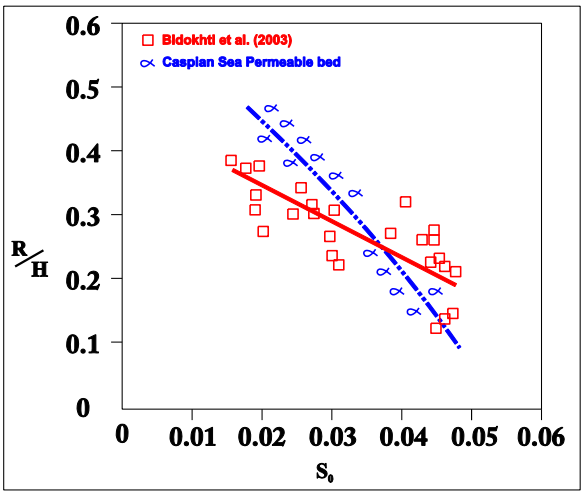

Figure 5; relative wave run up according to the wave sharpness for the permeability of Caspian Sea beach

Figure 6, compares the wave relative run-up according to the wave sharpness, between permeable beach of Caspian Sea with the permeability coefficient about 0.079, and the experimental beach in the study of

Beidokhti et al, (2003) [1] by their best fitting lines. Both studies illustrated that the permeability significantly causes high reduction of wave run-up, especially for the waves with poor sharpness. Actually this finding affirmed the result derived by the study of Beidokhti et al. [1].

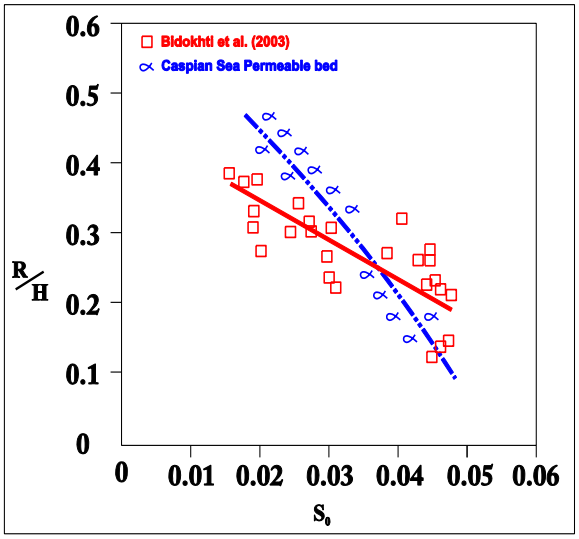

Figure 6; comparing of relative wave run up according to the wave sharpness over the Caspian Sea beach with the permeability coefficient about 0.079 and the study of Beidokhti et al (2003)

4-2- The effect of bed permeability on the bed currents

Reviewing the film record of the colored water movement, the effect of bed permeability on the current over the bed has been studied. The method used was based on the colored water movement and the calculation of the general current velocity over the bed in three positions: near the surface, middle and depth of the bed (Figure 7). Table 2, includes the waves height and frequency parameters along with the current velocity over the bed. The results derived by film analysis illustrated that by decreasing the radius of curvature in the current track, the bed permeability is getting decreased. Meantime, in the high depth the radius of curvature could be decreased also, as this finding illustrates that the strength of bed versus the fluid movement, gets increased by high depth and poor permeability.

Table 2; the information of measurements of the flow speed within the Caspian Sea bed

Experiment	Permeability	Wave frequency	Flow speed	Flow speed within the bed: Speed at depth of 5 cm. V1 (cm/s)	Flow speed within the bed: Speed at depth of 15 cm. V1 (cm/s)
1		9/5	1/95	1/2	1/96
2		9/1	1/2	1/11	0/99
3	(0/079)	8/4	1/55	1/16	1
4		9/1	1/04	1/12	0/95
5		8/3	1/1	1/1	0/93
6		9	1/09	1/38	0/91

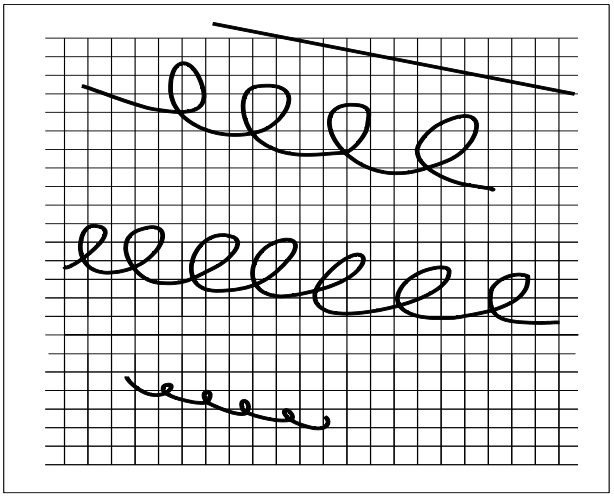

Figure 7. Track of injected color in three points respectively at 5cm, 10cm and 15cm from bed surface for the shore bed of Caspian Sea sample.

4-3- The effect of bed permeability on the tension imposed over the bed

As before mentioned, while the fluid penetrates/transpires the bed respectively a suction/injection process occurs. By studying the current tracks, U-suction and U-injection have been measured through different experiments for the permeability coefficient of 0.079. In the laboratory environment and during wave run-up/rundown, the horizontal velocity is the same run-up/rundown velocity, as defined the bed suction/injection respectively. Regarding the researches developed by Canli and Innman (1994) [3], and introducing the non-dimensional parameter (Ũ=Vz/Vx), this parameter is defined as following relations:

$$\tilde{U}zi=\frac{U\ injection}{U\ rundown} \text{ and } \tilde{U}zs\frac{U\ suction}{U\ runup} \qquad (3)$$

For all experiments, it is calculated that Ũzs and Ũzi are the same, regarding the absolute values. The findings are presented by table 3.

Table 3; the measurement of different speed parameters

Experiment No.	$U_{suction}$ (cm/s)	$U_{injection}$ (cm/s)	U_{runup} (cm/s)	$U_{rundown}$ (cm/s)	$\tilde{U}zs=\frac{Usuction}{Urunup}$	$\tilde{U}zi=\frac{U\ injection}{Urundown}$
1	-1/9925	1/0127	47/3921	25/4484	-0/0567	+0/042
2	-3/129	2/8028	32/874	20/34	-0/0618	+0/0670
3	-1/058	2/4680	20/427	16/525	-0/0756	+0/0878
4	-3/584	2/756	21/4316	16/815	-0/1487	+0/1068
5	-4/565	2/977	20/2176	14/5394	-0/1267	+0/1239
6	-25/8567	3/2454	20/5271	15/2062	-0/2328	+0/1328

Beidokhti et al`s observations (2003) [1] verified that in a wave with constant frequency, by increasing the

suction rate the bed tension in a permeable condition (t) comparing to the bed tension in a impermeable condition (t0), namely t/t0, is getting increased. Whiles, by increasing the injection rate the relation (t/t0) gets decreased. In the present investigation this problem has been studied according to 3 constant frequencies for the shore bed of Caspian Sea sample, and the results are shown by figure 8.

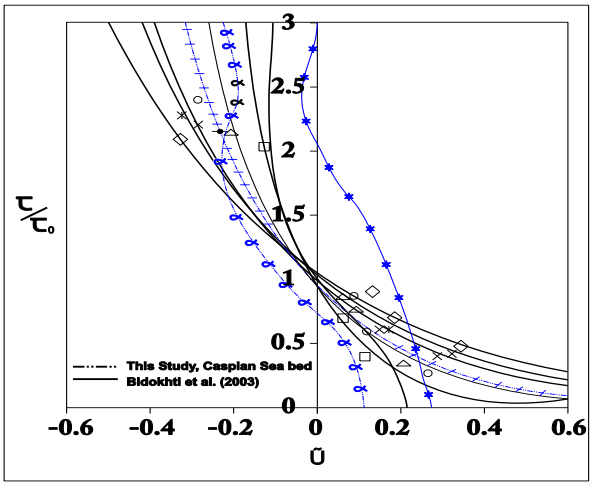

Figure 8; non dimensional parameter (Ũ) graph according to t/t0

5 – Results

The comparison between the results derived from Beidokhti et al`s experiments and the results of present experiments (Figure1), about the tension imposed on the bed, indicates that there is a similarity among the tension variations and the non-dimensional velocity through both studies.

Note, Canli and Inman (1994) [3] had done the experiments for a horizontal bed with different permeability, through one wave frequency only, and Beidokhti et al, 2003 [1] developed the experiments for an artificial sediments with different permeability, through 6 wave frequencies, whiles in the present investigation, the experiments have done on the samples of the Caspian Sea bed through 3 wave frequencies. The results obtained show that the reduction of relative tension up to about 80% in the injection phase was significantly evident, whiles in the suction phase increasing of relative tension is notable by 3 times (Figure 9). These intense variations illustrate the effect of bed permeability on tension, so that it should be taken into consideration in the natural conditions. It should be noted, the results obtained about wave run-up variations on the impermeable bed are pretty similar to the results of Ahrenz (1981) [7] so that in both of them the wave run-up height over the impermeable bed recorded with high ranks.

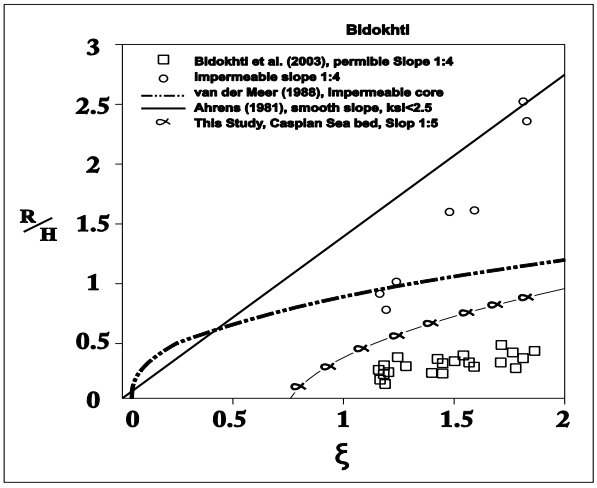

Figure 9; comparing the results of relative wave run up

6- Conclusion

The velocity of the current is getting decreased by poor permeability and deepening of the bed in the sample of Caspian Sea bed. Based on the observations of this experiment the velocity of the current within the bed does not relate to the wave frequency and the general line of current within the bed follows the water level. Vertical track of the fluid movement because of positive and negative imposed pressures on the bed (generated through wave run-up and rundown) completely depends upon the wave height and head. The fluid movement tracks as incomplete spiral lines parallel to the water level move towards outside.

In a wave cycle, the suction and injection phenomena are observed inside the bed. So that, by increasing/decreasing the head in result of wave run-up/rundown and imposing the positive/negative pressure on the bed the suction/injection occurs respectively. About the effect of permeability on tension imposed on the bed,it should be noted by increasing the suction velocity the tension on the bed is getting increased up to 3 times, whiles by increasing the injection velocity the tension on the bed is getting decreased about 80% , both phases (suction/injection) occur through approaching / receding of the vortex boundary layer to the bed. The variations of tension on the vortex boundary layer near the bed have a significant Importance.

The Increasing of bed permeability lead to decrease the wave run-up by 4 times and higher sharpness of wave also could decrease the wave run-up. Poor permeability in the sample of Caspian Sea bedincreases the wave run-up as it is evident on the permeable bed. Different permeability in proportion to the wave sharpness increase did not indicate a physical impact on wave run-up decrease.

Wave run-up from the ramped impermeable shore bed, as it is presented in the previous study,indicated of low ranks compared to the impermeable horizontal shore bed [8,9 and 10].

In a given permeability of the Caspian Sea bed with a specific wave frequency, by changing the wave height

there is not any changes at U parameter , namely the relation of Ũ=Vz/Vx, has been considered independent from the wave height. Through a specific wave frequency it is found that by increasing Uzs the ratio of t/t0 is getting increased, whiles by increasing Uzi the ratio of t/t0 is getting decreased, such as the obtained results by Beidkhti et al (2003) [1]. Thus, regarding the considerable effect of bed permeability on the tension imposed of bed, it is necessary these effects to be taken into consideration through the applied researches.

References

[1] Bidokhti,A. A., and Zoljoudi, M., (2003) The effects of permeable bed on waves run-up and surface stress., Journal of the Earth and Space Physics, Vol. 29, No.1, 23-33.

[2] Conley, D.C. and Inman, D.L. (1992) Field Observation of the Fluid Granular Boundary Layer under Near-Breaking. Journal of Geophysical Research , 97, 9631-9643. https:/doi.org/10.1029/92JC00227

[3] Conley, D.C. and Inman, D.L. (1994) Ventilated Oscillatory Boundary Layer. Journal of Fluid Mechanics , 273, 261-284. https:/doi.org/10.1017/S002211209400193X

[4] Villarroel-Lamb, D., Hammeken, A. and Simons, R. (2014) Quantifying the Effect of Bed Permeability on Maximum Wave Runup. 34th International Conference on Coastal Engineering, Seoul, South Korea, 15 June 2014.

[5] Hughes, S.A. (2004) Estimation of Wave Run-up on Smooth, Impermeable Slopes Using the Wave Momentum Flux Parameter. Coastal Engineering, No. 51, 1085-1104. https:/doi.org/10.1016/j.coastaleng.2004.07.026

[6] Antonia, R.A., Bisset, D.K., Fulachisr and Anselmet, F. (1990) Effect of Wall Suction on Bursting in a Turbulent Boundary Layer. Physics of Fluids A : Fluid Dynamics , 2, 1241-1247. https:/doi.org/10.1063/1.857624

[7] Ahrenz, J.P. (1981) Irregular Wave Run up on Smooth Slops. Technical Paper No. 81-17, U.S. Army Corps of Engineers, Coastal Engineering Research Center, Fort Belvoir, Virginia.

[8] Seelig, W.N. and Ahrens, J.P. (1981) Estimation of Wave Reflection and Energy Dissipation Coefficient for Beaches, Revetments and Breakwaters. TP 81-1 U.S. Army Corps of Engineers,Coastal Engineering Research Center, Fort Belvoir, VA, 40 P.

[9] Allsop, N.W.H., Hawkes, P.J., Jackson, F.A. and Franco, L. (1985) Wave Run-Up on Steep Slopes-Model Tests under Random Waves. Report SR2, Hydraulics Research Ltd., Wallingford.

[10] Postma, G.M. (1989) Wave Reflection from Rock Slops under Random Wave Attack. MSc Thesis, Delft University of Technology, Delft.

INTERNATIONAL JOURNAL OF
COASTAL & OFFSHORE ENGINEERING
IJCOE No. 4 / Autumn 2016 (33-41)

The Ability LNG, LPG and General Port Vessels Maneuvering in Berthing Zone of IRAN LNG Project Jetties in Persian Gulf

Ali Sheikhbahaei[1*], Said Mazaheri[2], Syrus Ershadi[3]

[1] *M.E. Student on Marine structure, Hormozgan University, Iran; A.Sheykhbahaee@Gmail.com*
[2] *Assist. Prof. in Offshore Eng., Head of Maritime Transportation and Technology Dept. Transportation Research Institute, Iran*
[3] *Assist. Prof. in Civil Eng. Dep., Technical Faculty, Hormozgan University, Iran*

ARTICLE INFO

Article History:
Received: 24 May. 2016
Accepted: 15 Dec. 2016

Keywords:
LNG & LPG Ships
LNG jetty & terminals
safety navigation
turning circle,
basin vessel maneuver,
approach system,
mooring facility.

ABSTRACT

For the purpose of having a safety navigation, the transportation path, deployment of carrier, physical specifications, locations and … have high level of importance. In this research, along with the above mentioned factors, we have compared the result with technical standard and commentaries for port and harbor facilities in Japan, and to analysis both advantage and disadvantages of them. The IRAN LNG project (ILC), will product the overall amount of 10/80 million tons of LNG per annum. Based on the type and capacity of LNG ship (Membrane Type,150000 m3), 13 vessels and 6 tug boat are estimated, mostly considered as high capacity LNG carriers. Since the IRAN LNG ships enter to terminal on ballast and after loading departure and also with considering number and marine traffic on South pars, one way channel with 0.5 L (L is length of ship) considered. On this base, we need Maximum width of 157.5 m and minimum 122m (for LNG Ships), and Maximum width 120m and minimum 89m (for LPG Ships). Area, circumference and diameter of basin with anchorage & buoys on general jetty that in collusive general Cargo, Sulphar & Ro-Ro berth respectively are 154610 m2, 1830m and 320m that covered Japanese's standard completely but about turning circle, we have area, circumference and diameter respectively 5896 m2, 250m and 708m which doesn't coordinate with Japan's standard except only one subject (Sulphar berth with aids tug boat).

1. Introduction

Natural gas transmission through its gas essence and the usage of pipelines in long distance confronts many difficulties in common. Based on available technology abilities , LNG method (liquefied natural gas) as an economic and confident one, can obviate the difficulty of gas shipment to transmit gas to far distances, to a great deal.

Great southern pars gas area in Persian Gulf is the biggest in the world and contains 50% of Iran gas storage and 9% of the world gas reservation.

This area in Persian Gulf establishes 27 phases of gas refinery, 25 petrochemical, projects and 3 LNG units in southeast of Bushehr.

2- Hydroclimotology of Studies Area

1-2- BMO wind data , has been gathered and based on revising and taking vessels in special period in one area , during more than 50 years, by British Meteorological office (BMO).

In the vicinity of project site , BMO data have been provided , especially for this project , for one 59-year period (from 1949 to 2007) in an area about 26 to 28 degrees latitude and 51 to 53 degrees longitude, The area cover is shown in Figure (1) and event percent in Table (1) , result show that predominant wind direction based on BMO data, from north to west (315) and the maximum recorded speed is equivalent to 27/8 m/s (Met-ocean Measurements,2006).

[DOR: 20.1001.1.25382667.2016.4.0.5.9]

Table 1: event percent of wind annum based on BMO data

Wind Speed Frequency (%)																	
Ws(m/s)\D	0	22.5	45	67.5	90	112.5	135	157.5	180	202.5	225	247.5	270	292.5	315	337.5	Total
5.4 – 7.9	0.825	0.144	0.144	0.084	0.383	0.849	0.981	0.359	0.287	0.096	0.072	0.203	1.375	4.269	6.015	2.428	18.514
7.9 – 10.7	0.562	0.06	0.036	0.06	0.299	0.526	0.49	0.215	0.072	0.012	0.012	0.024	0.741	3.36	5.322	1.937	13.728
10.7 – 13.8	0.263	0.024	0.048	0	0.048	0.191	0.167	0.06	0.012	0.036	0.012	0.012	0.215	1.471	2.464	0.729	5.752
13.8 – 17.1	0.012	0.012	0	0	0.048	0.096	0.06	0.012	0.024	0.012	0	0	0.06	0.383	0.897	0.287	1.903
17.1 – 20.7	0.024	0	0	0	0	0.012	0.012	0	0	0	0	0	0.012	0.084	0.239	0.048	0.431
20.7 – 24.4	0	0	0	0	0	0	0	0	0	0	0	0	0	0	0.012	0	0.012
24.4 – 28.4	0	0	0	0	0	0.012	0	0	0	0	0	0	0	0	0	0	0.012
28.4 <	0	0	0	0	0	0	0	0	0	0	0	0	0	0	0	0	0
Total	0.686	0.24	0.228	0.144	0.778	1.686	1.71	0.646	0.395	0.156	0.096	0.239	2.403	9.567	14.949	5.429	40.352

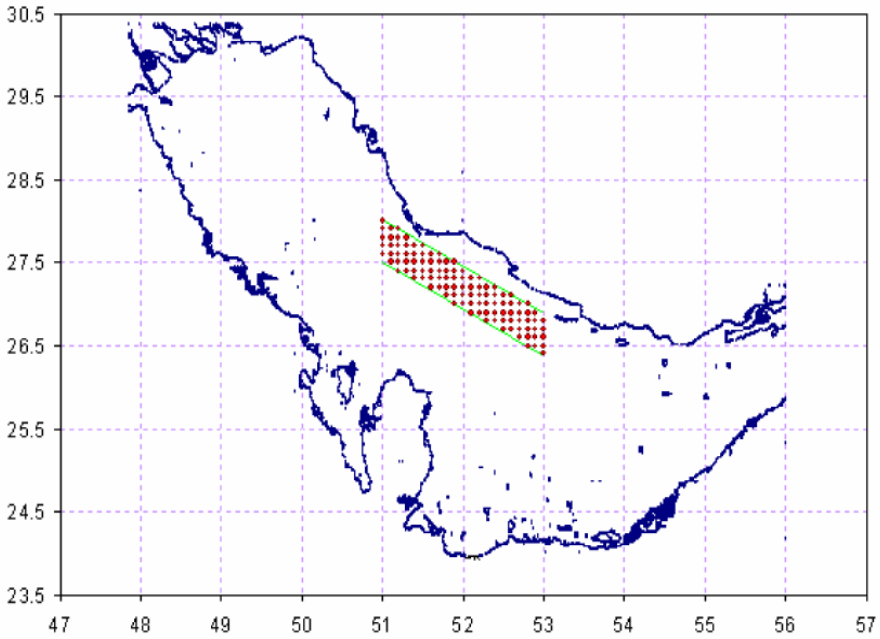

Figure 1: zone of under cover BMO near IRAN LNG site

2-2- BMO wave data

Table 2 and Figure 3; indicate the form of get wave rose of these data, statically and graphically. As it is obvious, predominant wave direction and the longest recorded wave maximum are 315° and 7/8 m /s (Met-ocean Measurements, 2006).

Table (2): height wave classification on base BMO data

Hs(m)\Dir	0	22.5	45	67.5	90	112.5	135	157.5	180	202.5	225	247.5	270	292.5	315	337.5	Total
0.5 – 1	1.441	0.274	0.548	0.345	1.513	1.87	1.941	0.869	1.06	0.369	0.476	0.536	3.704	5.419	6.444	2.513	29.322
1 – 1.5	0.953	0.226	0.179	0.119	0.762	1.227	1.417	0.465	0.417	0.155	0.167	0.238	2.215	4.931	7.444	2.906	23.821
1.5 – 2	0.524	0.06	0.107	0.024	0.274	0.417	0.584	0.226	0.071	0.06	0.048	0.024	0.691	2.739	4.502	1.489	11.84
2 – 2.5	0.274	0.048	0.036	0.024	0.071	0.25	0.167	0.143	0.06	0.012	0.024	0.024	0.465	1.608	2.358	0.75	6.314
2.5 – 3	0.095	0	0.012	0.012	0.048	0.167	0.107	0.036	0.024	0	0.012	0.012	0.155	0.917	1.096	0.345	3.038
3 – 3.5	0.048	0.012	0.012	0	0.012	0.036	0.024	0.024	0	0.012	0	0	0.048	0.238	0.631	0.214	1.311
3.5 – 4	0.012	0	0	0	0.012	0.012	0.036	0.036	0	0.012	0	0	0.036	0.226	0.25	0.06	0.692
4 – 4.5	0	0.012	0	0	0.024	0	0	0	0	0	0	0	0.024	0.107	0.095	0.06	0.322
4.5 – 5	0	0	0	0	0.012	0	0	0	0	0	0	0	0.012	0.071	0.083	0.012	0.19
5 – 5.5	0	0	0	0	0	0	0	0	0	0	0	0	0	0.071	0.048	0	0.119
5.5 – 6	0	0	0	0	0	0	0	0	0	0	0	0	0	0	0.036	0	0.036
6 – 6.5	0	0	0	0	0	0	0	0	0	0	0	0	0	0.012	0	0	0.012
6.5 - 7	0	0	0	0	0	0	0	0	0	0	0	0	0	0	0.012	0	0.012
7 – 7.5	0	0	0	0	0	0	0	0	0	0	0	0	0	0	0	0	0
7.5 - 8	0	0	0	0	0	0	0	0	0	0	0	0	0	0	0.012	0	0.012
8 – 8.5	0	0	0	0	0	0	0	0	0	0	0	0	0	0	0	0	0
Total	3.347	0.632	0.894	0.524	2.728	3.979	4.276	1.799	1.632	0.62	0.727	0.834	7.35	16.339	23.011	8.349	77.041

[DOR: 20.1001.1.25382667.2016.4.0.5.9]

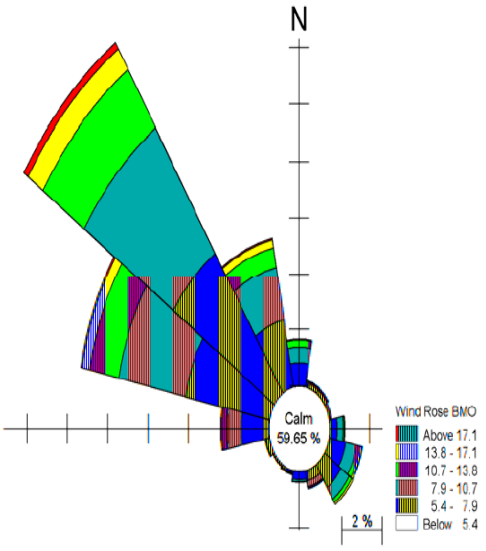

Figure 2: annum wind Rose based on BMO data

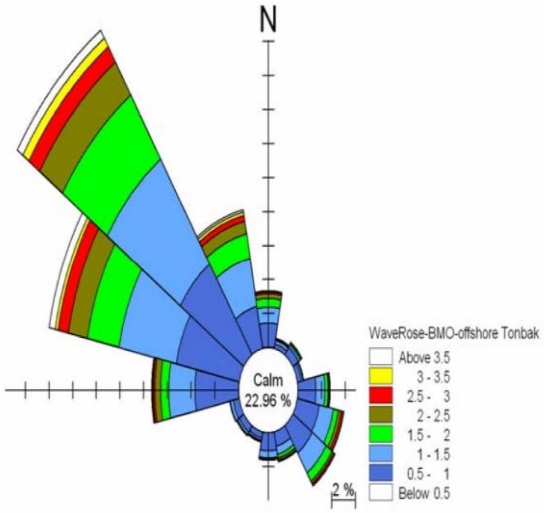

Figure 3: annum wave Rose based

3- Navigation Issues

In Consideration of physical characteristics and shipment case, vessel pith is of great importance for performing safe navigation (Navigation Aids, 2008) Therefore, we will consider navigation characteristics (length, width and depth) and turning circle (diameter) and basin (area and depth) of vessel in general and IRAN LNG (ILC) in particular, thus, we need vessels' feature listed in table 3 shortly (FEED, 2002).

Table 3: Vessels' feature in IRAN LNG Project

Properties			Overall Length (LOA)	Length between perpendiculars (LBP)	Beam (B)	Draft (D)	Capacity	Displacement tonnage (DT)
Units			m	m	m	m	Tons & m3	Tons
LNG SHIP	Max. ship		315	302	50	12.0	220,000 m^3	158,000
	Min. ship		244	230	34.4	9.9	70,000 m^3	55,500
LPG SHIP	Condensate	Max. Ship	278	264	45	12	150,000 tons	182,000
		Min. ship	214	206	34	12.3	60,000 tons	73,500
	LPG Vessel	Max. Ship	240	228	36	12.3	80,000 m^3	66,000
		Min. ship	178	167	27	9.5	30,000 m^3	34,000
Ro-Ro SHIP			198	180	40	9.5	22000 tons	39600
General Cargo SHIP			174	158	24.8	9.5	20000 tons	28000
Sulphar SHIP			116	105	19.4	7	6000 tons	8000

It should be mentioned that for measuring the duration of LNG loading and unloading, we will act as follow:
About 10 house for loading and unloading, 2.5 hours for approaching, berthing and mooring, 1.5 hours for cooling down and to hours for oceanic and atmospheric unexpected events.
Since this maneuver is done in source along with destination, loading and unloading take about 2 days. The most LNG production amount in ILC project is equivalent to 10/80 million tons which is considered as high capacity of 10/50 million, per annum.

The distance between loading location (general area , Tombak , IRAN LNG jetty) and unloading location (supposedly far east , Chinese southwest coasts) has been approximately considered 5000 sea miles , and 0/1 will be evaporated from the overall LNG , in this interval.

Required ships

$$= \frac{\dfrac{\text{factory production capacity (million tons per year)} \times \text{mean exploit percent of factory MMBTU} \times \text{termal capacity of LNG per ton}}{\text{LNG dencity}}}{\text{portage } (m^3) \times \text{termal capacity for per } m^3 \text{ LNG}}$$

$$\text{loading and unloading duration} + \text{berthing duration} + \frac{\text{interval between two port} \times 2}{\text{vessel speed} \times 24}$$

[DOR: 20.1001.1.25382667.2016.4.0.5.9]

So for IRAN LNG project we will have:

Number of Required Carriers

$$= \frac{\frac{10.8\times10^{6}\,kg}{450\,kg/m^{3}}}{145000m^{3}\times\frac{365day}{2day+\frac{5000mil\times2}{19\,mil/hr\times24\,hr/day}}} \approx 13\,farvand$$

1-3 width of Navigation Channel

In the determination of the width of a navigation channel, due consideration shall be given to the types and dimensions of target vessels, the traffic volume and length of the channel, and natural conditions including meteorological and marine conditions, but in such case that the use of tugboats is prescribed, a refuge area for vessel is provided, or the length of channel is very short, however, the channel width can be reduced to the extent not to hinder safe navigation of vessels.

In this case, is required to do complementary studies (Navigation Aids, 2008).

For ordinary navigation channels, the following values are adopted as the standard width:

a) For a double – way channel , an appropriate width that is 1.0 L or larger is adopted , except for :
   1- Cases in which the length of navigation channel is relatively long : 1.5L
   2- Cases in which the target vessels frequently pass in both ways through the channel : 1.5L
   3- Cases in which the target vessels frequently pass in both ways through the channel and the length of the channel is relatively long : 2.0L
b) For a one – way channel, an appropriate width that is 0.5 L or larger is adopted.

Since, vessels are imported in IRAN LNG project and they depart after loading and their interval time shipping is 2 days for LNG, 13 days for LPG and 20 days for sulphur ships.

Thus, sea traffic is not severe and we can consider one – way IRAN LNG, the width of navigation channel will be considered 0/5 L (Navigation Aids & Navigation study, 2008).

Based on related wharves, LNG and LPG carrier can pass one navigation channel, so based on Japan international standard we have:

Table 4: Suggested width of LPG and LNG vessels of Navigation channels in Iran LNG project.

Width of Navigation channel		Ship type
Min	Max	
244 (0.5) = 122	315(0.5)=157.5	LNG carrier
178(0.5)=89	240(0.5)=120	LPG carrier

Table 5: Suggested width of Ro-Ro , General cargo & sulphar vessels of Navigation channels in Iran LNG project

Ship type	Width of Navigation channel
Ro-Ro	198 (0.5) = 99
General Cargo	174 (0.5) = 87
Sulphar	116 (0.5) = 58

Table 6: Interval & down time shipping for IRAN LNG Project

Ship type	Interval time shipping	Down time shipping	
		Max	Min
LNG	2.2 days	0.26%	0.18%
LPG	13 days	---	---
Sulphar	20 days	27%	15%
Tug boat	---	2.51%	

Wharves of Ro-Ro, Sulphar and General Cargo vessels are located in municipal port (Ro-Ro berth Structural Design, 2008) , pass another navigation channel that is described below:

Mentioned down time for sulphur ship in above table will be per annum and if we want to consider it per season, it will be at least 40% and at most 55% (FEED, 2002).

It is required to mention that down time shipping is the duration that inappropriate atmospheric and oceanic condition, doesn't let the vessel, berth, load and unload(Mooring study for LNG & LPG condensate breath at Tombak, 2007).

3-2- Basin

In planning and design of basins , consideration shall be given to the safety in anchorage , the easiness of ship maneuvering , the cargo handling effectively, the meteorological and marine conditions , the effects of reflected waves and ship-generated waves on vessels in the harbor, and the conformity with related facilities. Therefore, the location of basin is determined appropriately in consideration of the layout of breakwaters, wharves and navigation channels, and the calmness requirement (Navigation study & Navigation Aids, 2008).

In the determination of the area of a basin used for anchorage or buoy mooring, due consideration shall be given to the purpose of the use, anchorage method, sea bottom material, wind speed, and water depth.

For buoy mooring, considerations shall be given to the type of the use and to the horizontal movement of the buoy when the tidal range is large. Swinging mooring (Fig. 4(a)) and mooring with two anchors (Fig. 4(b)) are the two most frequently used anchorage methods. The required length of anchor chain varies depending on the type of vessel, anchorage method, and meteorological and marine conditions. Therefore, it is necessary to determine the chain length in such a way that the holding powers of the mooring anchor and the chain lying on the bottom can resist the forces acting on the vessel under expected conditions. In general,

[DOR: 20.1001.1.25382667.2016.4.0.5.9]

the stability of the mooring system increases as the length of the anchor chain becomes longer.

The area of anchorage is defined as a circle having a radius equivalent to the sum of the vessel's length and the horizontal distance between the bow and the center of rotation.

Figure 4(c) shows a vessel moored in a single-buoy mooring, and Figure 4 (d), shows a vessel moored in a double-buoy mooring with buoys located in bow and stern the vessel. In this double-buoy mooring, it is necessary to locate the buoys in such a way that the line connecting the two buoys becomes parallel with the directions of tidal currents and winds. In the determination of the area of these types of buoy mooring areas, Table (9) may be used as a reference.

Table 7: anchorage area in mooring with anchor

Purpose of the use of the basin	**Anchorage method**	**Sea bottom material or wind speed**	**Radius**
Offshore waiting or cargo handling	Swinging mooring	Good anchoring	L + 6D
		Poor anchoring	L + 6 D + 3m
	Moring with two anchors	Good anchoring	L +4.5 D
		Poor anchoring	L +4.5D +25m

Thus, by basing the above table for IRAN LNG, we will have:

Table 8: area of basin in mooring with anchor in IRAN LNG Project

Kind of vessel				**LNG ship**		**LPG ship**	
Purpose of the use of the basin	Anchorage method	Sea bottom material or wind speed	Radius	Max(m)	min(m)	Max(m)	min(m)
Offshore waiting	Swinging mooring	Good anchoring	L+6D	315+6(15) =405	244+6(15) = 334	240+6(15)= 330	178+6(15) = 268
		Poor anchoring	L+6D+30 m	315+6(15)+30= 435	244+6(15)+30= 364	240+6(15)+30 = 360	178+6(15)+30= 298
	Mooring with two anchors	Good anchoring	L+4.5D	315+4.5(15)= 382.5	244+4.5(15)= 311.5	240+4.5(15) = 307.5	178+4.5(15)= 245.5
		Poor anchoring	L+4.5D+ 25m	315+4.5(15)+25 = 407.5	244+4.5(15)+25= 336.5	240+4.5(15)+ 25 = 332.5	178+4.5(15)+25= 270.5

Kind of vessel				**General cargo ship**		**Ro-Ro ship**	
Purpose of the use of the basin	Anchorage method	Sea bottom material or wind speed	Radius	Max(m)	min(m)	Max(m)	min(m)
Offshore waiting	Swinging mooring	Good anchoring	L+6D	174+6(11) =240	158+6(11) =207.5	198+6(11)= 264	180+6(11) =246
		Poor anchoring	L+6D+30m	174+6(11)+30= 270	158+6(11)+30= 154	198+6(11)+30 = 294	180+6(11)+ 30 = 276
	Mooring with two anchors	Good anchoring	L+4.5D	174+4.5(11)= 223.5	158+4.8(11)= 207.5	198+4.5(11) = 247.5	180+4.5(11) = 229.5
		Poor anchoring	L+4.5D+25m	174+4.5(11)+25 = 248.5	158+4.5(11)+25 = 232.5	198+4.5(11)+25 = 272.5	180+4.5(11)+ 25 = 254.5

Kind of vessel				**Sulphar ship**	
Purpose of the use of the basin	Anchorage method	Sea bottom material or wind speed	Radius	Max(m)	min(m)
Offshore waiting	Swinging mooring	Good anchoring	L+6D	116+6(11) =182	105+6(11) = 171
		Poor anchoring	L+6D+30m	116+6(11)+30 = 212	105+6(11)+30 = 201
	Mooring with two anchors	Good anchoring	L+4.5D	116+4.2(11) = 165.5	105+4.5(11) = 154.5
		Poor anchoring	L+4.5D+25m	116+4.5(11)+25 = 190.5	105+4.5(11)+25= 179.5

Since the largest circle that can be embedded in general cargo, Ro-Ro basin , and Sulphar berth is approximately 320 meters long, it doesn't cover international standards and commentaries for port and harbor facilities in Japan , and the only corresponding

[DOR: 20.1001.1.25382667.2016.4.0.5.9]

case in Sulphar Ship is mooring with two anchors (Figures 5 and 6).

It is required to mention that L is the overall vessel and D, the water depth in below equations.

Table 9: area of basin used for buoy mooring

Anchorage method	Area
Singe-buoy mooring	Circle having a radius of (L+25m)
Double-buoy mooring	(L+50m) × L/2 rectangle

In IRAN LNG project, the area of basin in single – buoy mooring method is equivalent to:

Table 10: The area of basin single – buoy mooring in ILC project

Kind of vessel		LNG ship		LPG ship	
Size		Max (m)	min (m)	Max(m)	min(m)
Single-buoy mooring	Circle having a diameter of (L+25m)	315+25=340m	244+25=269	240+25=265	178+25=203
Double-buoy mooring	Rectangular (L+50m) L/2	(315+50)315/2= 57487.5	(244+50)244/2= 35868	(240+50)240/2= 34800	(178+50)178/2= 20292

Kind of vessel		General cargo ship		Ro-Ro ship	
Size		Max (m)	min (m)	Max(m)	min(m)
Single-buoy mooring	Circle having a diameter of (L+25m)	174+25=199	158+25=183	198+25=223	180+25=205
Double-buoy mooring	Rectangular (L+50m) L/2	(174+50)50/2= 5600	(158+50)50/2= 5200	(198+50)198/2= 24552	(180+50)180/2= 20700

Kind of vessel		Sulphar ship	
Size		**Max (m)**	**min (m)**
Single-buoy mooring	Circle having a diameter of (L+25m)	116+25=141	105+25=130
Double-buoy mooring	Rectangular (L+50m) L/2	(116+50)50/2= 4150	(105+50)50/2= 3875

Since area , circumference and diameter of basin in ILC project for General cargo, sulphur, and Ro-RO vessels are 154610 m^2 , 1630m and 320m (Navigation Aids , 2008 , [14] , the only corresponding case with international standard in Japane , is the area of basin in sing – buoy mooring method for sulphur ship (Figures 5 to 7).

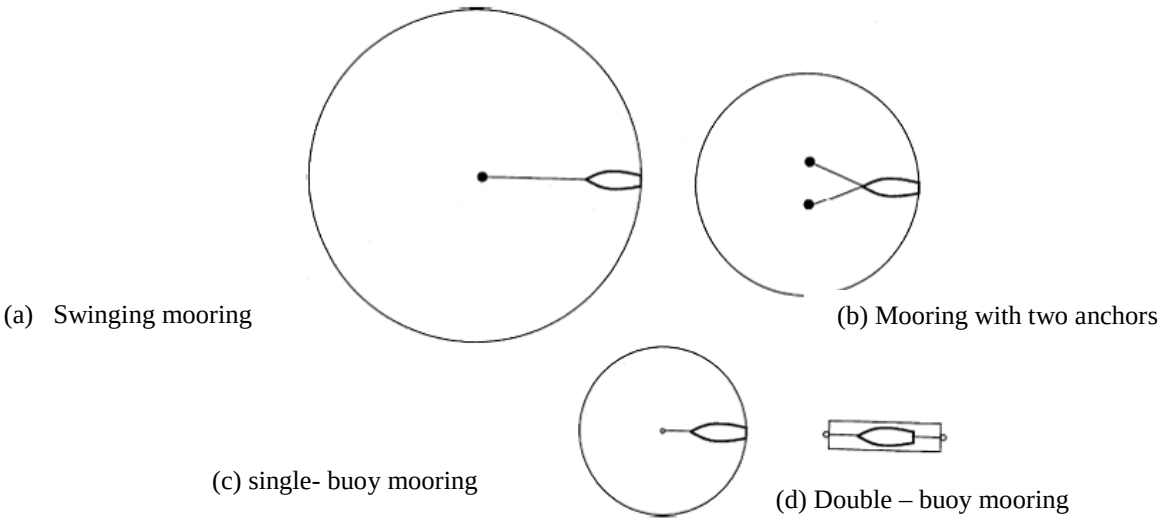

(a) Swinging mooring

(b) Mooring with two anchors

(c) single- buoy mooring

(d) Double – buoy mooring

Figure 4: Basin concept of area of basin (per vessel)

[DOR: 20.1001.1.25382667.2016.4.0.5.9]

The area of basin for LPG and LNG wharves doesn't have any limitations in this case and doesn't correspond to international standards either.

3-3- Turning circle

Turning basins are used for vessels' maneuvering.

In the determination of the area of a basin used for bow turning, due considerations shall be given to the method of bow turning, the vessels' bow turning performance, the layout of mooring facilities and navigation channels, and the meteorological and marine conditions, and turning basins should be located appropriately in front of mooring facilities in consideration of the layout of other navigation channels and basin (Navigation Aids & Navigation study, 2008). The standard area of turning basin is as follows:

(a) Bow turning without assistance of tugboats: circle having a diameter of 3L.

(b) Bow turning using tugboat: circle having a diameter of 2 L.

Thrusters with a sufficient power may be considered as equivalent to a tugboat (Maneuvering Simulations with three types of ships for the industrial part of Tombak, 2008). As for small ships, when the above standard area cannot be provided due to topographic conditions, the area of turning basin may be reduced to the following level by using mooring anchors, winds, or tidal currents (Navigation study, 2008):

a) Bow turning without assistance of tugboat: circle having a diameter of 2L.

b) Bow turning using tugboat: circle having a diameter of 1.5L.

The area of turning basin for different vessels of IRAN LNG project is measured based on international standards and port facilities in Japan, listed in Table 11.

Table 11: The Area of Required Turning Circle for Vessel Maneuvering.

Kind of vessel		*LNG ship*		*LPG ship*	
size		*Max*	*min*	*Max*	*min*
Without tog boat	*Circle having a diameter of 3L*	*3(315)=945*	*3(244)=732*	*3(240)=720*	*3(178)=534*
With using tog boat	*Circle having a diameter of 2L*	*2(315)=630*	*2(244)=488*	*2(240)=480*	*2(178)=356*

Kind of vessel		*General cargo ship*		*Ro-Ro ship*	
size		*Max*	*min*	*Max*	*min*
Without tog boat	*Circle having a diameter of 3L*	*3(174)=522*	*3(158)=474*	*3(198)=594*	*3(180)=540*
With using tog boat	*Circle having a diameter of 2L*	*2(174)=348*	*2(158)=316*	*2(198)=396*	*2(180)=360*

Kind of vessel		***Sulphar ship***	
size		***Max***	***min***
Without tugboat	*Circle having a diameter of 3L*	*3(116)=348*	*3(105)=315*
With using tugboat	*Circle having a diameter of 2L*	*2(116)=232*	*2(105)210*

Since the area, circumference and diameter of turning circle in Ro-Ro general cargo and Sulphar jetties confines, are equivalent to 5896 m^2 , 708 and 250m respectively (Navigation study,2008) depending on the computations of the above table, it is determined that this diameter doesn't correspond international in Japan except for one case.(Sulphar ship with tugboat)

4-3 Depth of basin

The depth of basin below the datum level shall be determined by adding an appropriate keel clearance to the maximum draft expected (such as full draft). Where the seasonal variation in the mean sea level is larger than the tide level variation due to astronomical tide and the mean sea level frequently becomes lower than the datum level or waves or swell of appreciable heights enter the basin, it is necessary to consider the effects of these phenomena.

In IRAN LNG project, water depth in Ro-Ro, General cargo and Sulphure basin limit is varied from -5 to -11 meters reaching 11 meters after dredging the depth of the whole areas. Water depth in LNG and LPG jetties limit, is also equal to -15 meter (FEED, 2002). It is also required to mention that 10 degrees of berthing angle, 0, 02 m/s berthing design speed and loading vessel have under keel clearance, equals 1.5 meter and along with 20 fenders installed in 20 m intervals (Mooring study for LNG & LPG condensate breath at Tombak, 2007).

5-3 Calmness of basin

[DOR: 20.1001.1.25382667.2016.4.0.5.9]

For basins that are located in front of mooring facilities and used for accommodating or mooring vessels, the calmness of a specified level shall be achieved for 97.5% or more of the days of the year, except for these cases where the use of the mooring facilities or the area in front of the mooring facilities is categorized as a special use.

The threshold wave heights for cargo handling for basins in front of mooring facilities should be determined appropriately in consideration of the type, size and cargo handling characteristics of the vessels. For this purpose, the values listed in Table (12) may be adopted (Mooring study for LNG & LPG condensate breath at Tombak, 2007).

Calmness of basin is usually evaluated by the wave height in the basin, but it is desirable to consider as necessary the effects of wave direction and period which affect the motions of moored vessels as well.

Table 12: Threshold wave height for Cargo Handling.

Ship Size	Threshold wave height for cargo handling (H 1/3)
Small- sized ships	0.3 m
Medium- and – large- sized vessels	0.5 m
Very large vessels	0.07 – 1.5 m

Displacement Tonnage (DT) is equivalent to 555000 and 34000 respectively, for the smallest LNG and LPG vessels, and the largest ones are 158000 and 66000.

Thus, depending on this category, LNG vessels are classified as very large & LPG ones, as large to very large vessels. Since the computation base of hydrodynamic IRAN LNG (ILC) project is BMO data, we will have Table 12: ($_{Hs}$) mean = 0.88 m, (Hs) max = 7.8 m.

Table 13 , gives as references the allowable amplitudes of vessel motions for different type of cargo handling, that have been suggested by Ueda, and Shiraishi and PIANC, we can find allowable amplitudes of LNG and LPG vessel motions, that are a special kinds of tugboat, in a following table:

Table 13: Allowable Amplitudes of Vessel Motions for Different Type of Vessels

Vessel type	Surging	Swaying	Heaving	Rolling	Pitching	Yawing
General Cargo ships	±1	±0/75	±0/5	±2/5	±1	±1/5
Grain carriers	±1	±0/5	±0/5	±1	±1	±1
Ore carriers	±1	±1	±0/5	±3	±1	±1
Oil tankers(foreign route)	±1/5	±0/75	±0/5	±4	±2	±2
Oil tankers (coastal route)	±1	0/75	±0/5	±3	±1/5	±1/5
Container ships (Lo/Lo)	±0/5	±0/3	±0/3	±1/5	±0/5	±0/5
Ferries, container ships (Ro-Ro) and pure car carriers	±0/3	±0/6	±0/3	±1	±0/5	±0/5

4-References:

Report

Sahel consultant engineering, 2008, ″ Ro-Ro berth Structural Design ″

Sahel consultant engineering, 2008, ″ LPG Trestle Structural Design ″

JGC group, 2002, ″ Front End Engineering Design Package (FEED) ″, P III

Water & environment technology co., 2006, ″ Met-ocean Measurements ″

Sahel consultant engineering, 2007, ″ Hydrodynamics studies report ″

Sahel consultant engineering, 2008, ″ Hydrologic and climatic studies ″

JGC group, 2002, ″ Specification for LNG jetty″ for Tombak, Iran

Sahel consultant engineering, 2008, ″ Navigation Aids ″

Sahel consultant engineering, 2008, ″ Navigation study ″

Alkyow hydraulic consultancy & research, 2007, ″ Mooring study for LNG & LPG condensate breathe at Tombak″

Alkyow hydraulic consultancy & research, 2008, ″ Maneuvering Simulations with three types of ships for the industrial part of Tombak″

Sahel consultant engineering, 2008, ″ Berthing approach system spec.″

Sahel consultant engineering, 2008, ″ Geotechnical Design Parameters (Part 1) ″

Sahel consultant engineering, 2008, ″Morphodynamic studies″

Sahel consultant engineering, 2008, ″Geotechnical Design Parameters (Part 2)″

Sahel Consultant engineering, 2008, ″ Suspended Deck Structures design Criteria″

Sahel consultant engineering, 2008, ″ Ro-Ro berth structural analysis ″

Books:

2002, ″ Technical standards and commentaries for port and harbour facilities in Japan″, handbook of harbour facilities

2006 ,″ port and Marine Structures Design Manual in IRAN ″, NO.300-6

[DOR: 20.1001.1.25382667.2016.4.0.5.9]

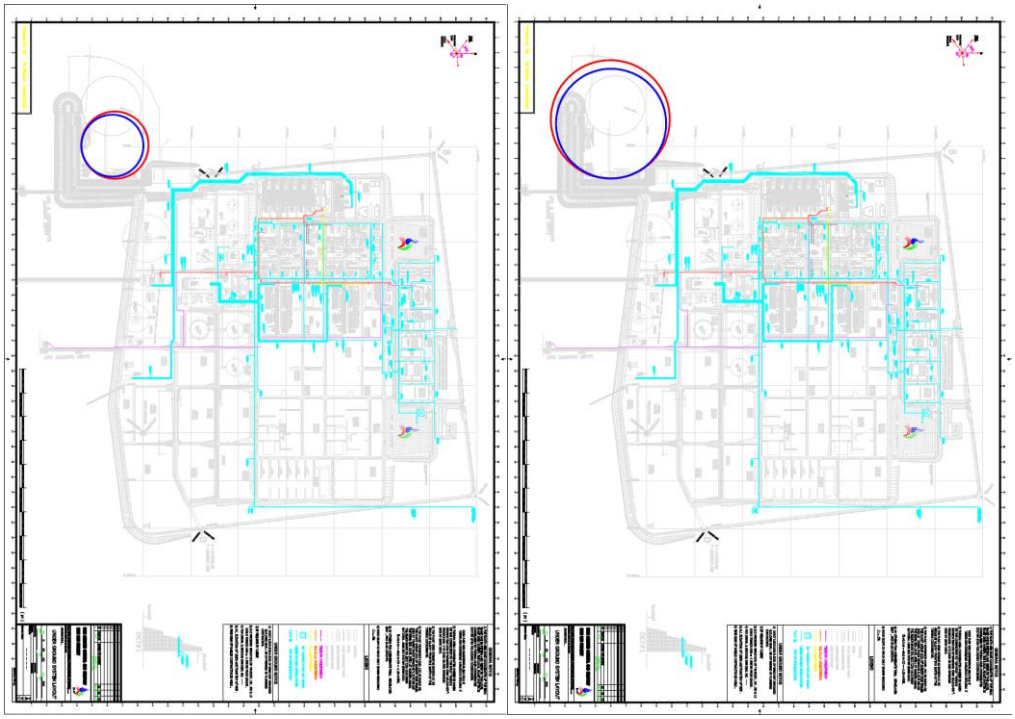

General port: Area basin used for buoy mooring, single buoy
Max. Radius: 141m, min. Radius: 130m

General port: anchoring area, offshore waiting, swinging mooring, good anchoring, Max. Radius: 247.5m
Min. radius: 229.5m

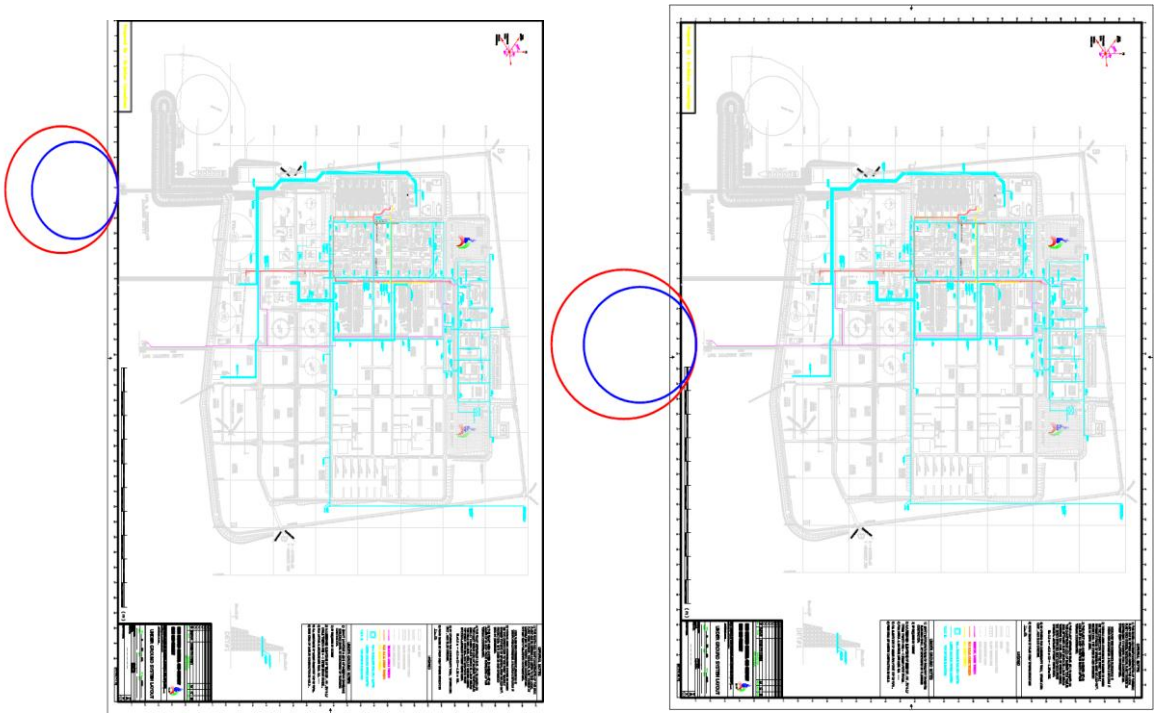

Area basin used for buoy mooring, single buoy,
For LPG jetty, Max. Radius: 265m, min. Radius: 203m

Area of turning circle for LNG jetty, with using tug boat
Max. Radius: 315m, min. radius: 244m

Figure 5: Basin and Turning circle Area in IRAN LNG project jetties

[DOR: 20.1001.1.25382667.2016.4.0.5.9]

INTERNATIONAL JOURNAL OF
COASTAL & OFFSHORE ENGINEERING
IJCOE No. 4 / Autumn 2016 (43-50)

Numerical Analysis of Dynamics of Ship-OWT (Offshore Wind Turbine) Collision

Hossein Nemati [1], Farhood Azarsina[2]

[1]*M.S. in civil engineering, Islamic Azad University, Science and Research Branch of Tehran; Nematibusiness@gmail.com*
[2]*Assistant Professor, Islamic Azad University, Science and Research Branch of Tehran; farhood.azarsina@mun.ca*

ARTICLE INFO

Article History:
Received: 13 Oct. 2016
Accepted: 15 Dec. 2016

Keywords:
Offshore wind turbine
the floating vessel
dynamic numerical analysis
software ABAQUS

ABSTRACT

Offshore Structures supply vessels during operation are at risk of collision. The ship has random load, including offshore structures resistance is raised. In this paper, under the impact of a wind turbine offshore supply vessel with 5 different mass displacements are analyzed. Structural study examined the environmental conditions intermediate depth ocean water using ABAQUS finite element model of the software. The effects of static preload weight of turbine blades and environmental loads (wind, wave, sea current and the water pressure on the turbines) before hitting the ship dynamics, in terms of the structural behavior. Parameters such as power and momentum of support, around the turbine horizontal displacement, stress and strain Von-Mises different parts of turbines in different loading conditions (change in mass displacement of picky float) compared together and the results are discussed.

1. Introduction

The offshore environment can provide a variety of renewable energies by which communities can provide the energy required because of the marine environment, a lot of energy in the form of heat, wave, wind, tidal produces. The existing offshore structures in the present day mobile and fixed offshore wind turbines for optimal use of wind power, both inside and outside the country are very important.

These structures by the mechanical energy of the wind generator, the power required to transform communities. Therefore, careful analysis of collision is important. According to figures released by the Health and Safety [1] management on offshore installations in the UKCS 1975 to 2001, numbers of 551 incidents of collisions of ships with a variety of offshore installations have been registered [2].

Dealing with the causes of the accident are 5 main groups [3]:

- Estimates and false diagnosis captain (the main cause of collisions)
- The loss of equipment (e.g. power loss vessel dynamic positioning)
- Weather and environmental conditions
- Anchor problems running or cable anchoring (jams or stretching anchors and anchors)
- Others

This paper attempts to simulate offshore wind turbine with a constant supply vessel collision incident Monopole deals. In previous studies using the finite element method has been done, a lot of simplifying assumptions, especially with respect to geometric modeling turbine can be seen. Also, in previous studies to facilitate the issue is complex, dynamic and a quasi-static that could shed light on the exact mechanism of collision. But here is completely dynamic approach is investigated.

Literature Review

In this regard, Such work began in the early years and then with the development of computer software for numerical analysis and finite element methods in the analysis and comparison with experimental data was available simple laboratory model to help studying more complex finite element models.

Menkes [4] In experimental studies completely fixed on a beam that was equally affected by the impact load, showed that the severity of injury, damage distinguishable from each other three modes of structure completely that can be observed. The various modes of failure of the sheet are also examined.

They continued in the study by Smith and Nurick [5] the failure modes of the circular sheet and Olsen studies [6] square sheets of failure modes were found.

From 1990 onwards, the scientists investigated the effect of different boundary conditions, the reinforcement steel and different loading conditions were inclined to force to determine the deformation,

to investigate the process of turbine as well as tear sheets.

Nurick and devices [7] experimental results on a square sheet steel fixed fines provided under impact loading. They showed phenomenon started tearing through the sides and across the border continues to the corners.

In 1998 Luca and Penn [8], analysis of dynamic elastic and non-reinforced sheet steel panels using simplified and advanced analytical techniques had taken.

Nurick [9] used to implement the rigorous test condition and the test is also consistent with the theory.

Geometric modeling of wind turbine

Dimensions and geometric parameters of the wind turbine fixed Mono-pile studied in this paper is specified in the table below.

Table1. Geometric characteristics of turbine

60	Turbine Blade weight (ton)
80	Diameter of turbine blades (m)
80	Height of horizontal axis of blades from the water level (m)
5	Base diameter of turbine (m)
0.05	Base thickness of turbine (m)
10	Diameter of energy absorber sphere (m)
0.1	Thickness of energy absorber sphere (m)
0.65	Drag coefficient of mono-pile cylinder
1.6	Inertia coefficient of mono-pile cylinder

One of the most important components of a wind turbine energy-absorbing steel spherical shell (with slippery surface mounted on the base) is just floating in the clash. The use of this butter, the creation of a centralized force on the floating turbine, protection of electronic equipment installed on the turbine, reducing the energy absorbed by the turbine during the process of collision and preventing collisions huge floating to the surface Turbine is.

The spherical shell is used to increase capacity to deal with its float, a ring with a thickness of 10 cm, the use and installation of the spherical shell and the base of the turbine. Below method of modeling the sphere and energy-absorbing ring, can be seen in software:

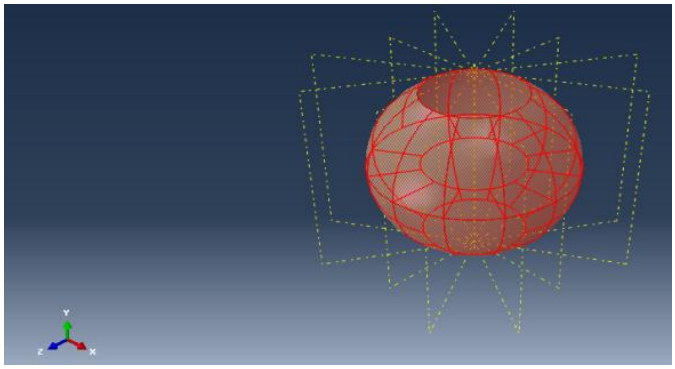

Figure1.modeling the sphere and energy absorber ring

Describing the collision

The main purpose of article is investigation on the dynamic fracture of offshore wind turbine structures due to the collision of floating to it. How to deal with a floating wind turbine is a complex nonlinear problem involving nonlinear dynamics and geometry of the problem is being encountered. Nonlinear finite element method is a useful method to solve this problem.

It is better to compare both the spherical shell and not have to use it. Studies show that the force of the collision on floating wind turbines to the main base of the turbine in the case of sphere, is about half. The energy absorbed by the turbine in the case of sphere, will be reduced significantly. Therefore, the spherical shell mentioned in the analysis of this deal will play an important role.

In general, the analysis of vessel collisions with turbines, based on the principle of conservation of momentum and energy based.
Local deformation in the collision is an example of this method.

The principle of conservation of momentum to the collision incident is written as follows [10]:

$$(m_s + a_s)v_s + (m_p + a_p)v_p = (m_s + a_s + m_p + a_p)v_c \quad (1)$$

In above relation m_s and m_p were floating mass and the mass of the turbine, a_s and a_p were added mass and added mass floating turbine, v_s and v_p and v_c respectively represent floating rate before hitting the structures, turbine speed before the collision float Subscribe to the vessel and the turbine speed collisions are traumatic.

The principle of conservation of energy for the collision incident is written as follows [10]:

$$\frac{1}{2}(m_s + a_s){v_s}^2 + \frac{1}{2}(m_p + a_p){v_p}^2 = \frac{1}{2}(m_s + a_s + m_p + a_p){v_c}^2 + E_s \quad (2)$$

In the above relation, E_s is depreciated strain energy of the system after the collision, which is defined as follows:

$$E_s = \frac{1}{2}(m_s + a_s)v_s^2 \left[\frac{(1-\frac{v_p}{v_s})^2}{(1+\frac{m_s+a_s}{m_p+a_p})} \right] \quad (3)$$

Assuming the rest of the incident energy source for the body hit collision, kinetic energy is floating support. The total energy of the collision is due to the full integration method for solving the shell element is calculated using the following equation:

$$E_{total} = E_{kinetic} + E_{internal} + E_{slide} \quad (4)$$

Where $E_{kinetic}$ is kinetic energy of picky substance, $E_{internal}$ is internal energy of the body hit and E_{slide} by the sliding energy, obtained from contact between the two structures.

Environmental conditions in the study area

Information listed in the table below in relation to environmental conditions is derived from PETRONAS Company in Malaysia:

Table2. the environmental situation of case study area

28	Area wind speed at the height of 10 meters of static water level (m/s)
8	characteristic wave height (m)
9.4	characteristic wave period (s)
1.5	Sea flow speed at water level (m/s)
1.2	Sea flow speed at the height of 15 meters from sea bed (m/s)
0.3	Sea flow speed at the height of 3 meters from sea bed (m/s)
1025	water density ρ_{water} ($\frac{kg}{m^3}$)
1225	weather density ρ_{wind} ($\frac{kg}{m^3}$)
30	Water depth (m) d (m)

Investigation of the environmental forces on the turbine structures

Wind force on the structure of the surface water in the form of static and rotating horizontal axis turbines apply. Distribution of wind speed in the region is as follows [11]:

$$\frac{u_h}{u_H} = (\frac{h}{H})^{\frac{1}{n}} \quad (5)$$

Where u_h wind speed at height h from the surface of the water, u_H wind speed at an altitude of 10 meters above sea level, 1 / n is called the front, usually depending on the sea state, distance to the water and the wind continued between 1 / 13 and 1/7 respectively.

Power, for storm is equal to 1 / 13 for the issue in this project is considered equal to 1/8, H 10 cm, h is the height of the water level.

According to API regulations on turbines wind power per unit length is calculated as follows:

$$F_{wind} = \frac{1}{2}\rho_{wind} u_h^2 C_s A \quad (6)$$

Where ρ density of air around the structure, Cs cylindrical shape factor equal to 5.0 (depending on the shape of the body and air viscosity) and A is the projected area of the cylindrical structure per unit length is equal to 5 square meters.

The second force is the force of waves on structures.

The project for calculating the parameters of the wave, the wave theory of linear Airy will use Linear wave equation can be solved directly by the equations obtained. In this case, the speed potential of the equation can be written as follows [12]:

$$\phi = \frac{H_s g T_s \cosh(ks)}{4\pi \cosh(kd)} \sin\theta \quad (7)$$

Parameter represents the wave number k or the phase difference θ is:

$$\theta = kx - \frac{2\pi}{T_s}t \quad (8)$$

The dispersion relation to the value of k, we have:

$$\omega^2 = gk\tanh(kd) \quad (9)$$

To obtain a defined wavelength, we write the following relationship:

$$L_{wave} = \frac{2\pi}{k} \quad (10)$$

In general, continuity equation can be written as follows:

$$\frac{\partial^2\phi}{\partial x^2} + \frac{\partial^2\phi}{\partial y^2} + \frac{\partial^2\phi}{\partial z^2} = 0 \quad (11)$$

Therefore:

$$\frac{\partial^2\phi}{\partial t^2} + g\frac{\partial\phi}{\partial z} = 0 \quad (12)$$

In this theory, for profile of free surface of waves we have:

$$\eta = \frac{H}{2}\cos\theta \quad (13)$$

$$U = \frac{\pi H_s \cosh(ks)}{T_s \sinh(kd)}\cos\theta \quad (14)$$

U is the maximum angle θ equal to 45 °. Therefore:

$$U_{\max} = \frac{\pi H_s \cosh(ks)}{T_s \sinh(kd)} \times \frac{\sqrt{2}}{2} \quad (15)$$

Acceleration of fluid particles on the surface of the substrate s at the height of the turbines will be equal to:

$$\dot{U} = \frac{2\pi^2 H_s \cosh(ks)}{T_s{}^2 \sinh(kd)} \sin\theta \quad (16)$$

U is the maximum angle θ equal to 45 °. Therefore:

$$\dot{U}_{\max} = \frac{2\pi^2 H_s \cosh(ks)}{T_s{}^2 \sinh(kd)} \times \frac{\sqrt{2}}{2} \quad (17)$$

Based on Morison Equation, maximum wave force per unit length on the turbine structure consists of two drag Forces F_D, depending on the kinetic energy of water and the force of inertia F_I is associated with accelerated particles, respectively. The forces calculated by the following formula [13]:

$$F_I = \rho_{water} C_M \pi \frac{D^2}{4} \dot{U} \quad (18)$$

$$F_D = \rho_{water} C_D \frac{D}{2} U^2 \quad (19)$$

To obtain the wave forces on the structure of its length must be gathered drag with the force of inertia on the turbine [14]:

$$F_{wave} = F_I + F_D \quad (20)$$

The third force is the force of the sea on the structure. With regards to information about the environment is to calculate the force exerted on the structure we have:

$$F_{current} = \rho_{water} C_D \frac{D}{2} |U_{current}| U_{current} \quad (21)$$

The fourth force is the force of the collision floating turbine. In a simple way, the collision can be modeled by time point.

In this case, the force of the static water level to be considered contrary to the x-axis. According to DNV regulations to acquire the force of floating offshore wind turbines have a base:

$$F_{impact} = 2.5\Delta \quad (22)$$

Where Δ floating mass (including the added mass) in the formula of F, KN and unit of Δ also be considered. Time analysis of dynamic forces exerted on the structure is 200 ms (Time period = 200 ms). At the same time force 50 millisecond intervals and analyzing various parameters such as stress, strain, displacement, and is equal to 1 mili second.

Impact force in a triangular pulse is applied to the structure.

Fifth force is the weight of the turbine blades. As mentioned turbine blades weigh 60 tons is considered. Circular cross-section of the cylinder is equal to:

$$\pi D_{pile} = 15.7 \quad (23)$$

Thus, the weight per unit length of the turbine blades on the top of the cylinder enters will be achieved.

The last force is pressure around the turbine. The study projects non-viscous liquid water, is non-rotating and incompressible. The pressure changes in the water and its calculation formula is as follows:

$$p_{water} = \rho_{water} g h \quad (24)$$

Impact force, with the exception of floating dynamic forces is static. In order to calculate the maximum stress applied to the system, wind and wave forces and current research in this line and have to be considered. It is important that the effect of the wind and the waves to be coupled and at the same time (as a linear superposition) make relevant analysis.

Appropriate element for modeling the structure

It is appropriate to analyze the dynamic element, the element is Shell. After successive changes in the dimensions and layout of finite element and obtaining proper convergence solutions from Shell four-node elements (S4R) is used. In addition, the use of shell elements with respect to the dimensions of the sheet is perfectly logical assumption is appropriate.

Analysis of materials used in the manufacture of turbine

To analyze this ordinary steel marine grade E elastic properties - plastic liner that general properties of ABS are based on US regulations are as follows:

Table 3.materials used in manufacturing turbine

$\rho_{steel} = 7800\ \frac{kg}{m^3}$	Usual steel density
$\sigma_y = 242$ MPa	Yield stress of usual steel
$\sigma_{ult} = 531$ MPa	Plastic ultimate stress of usual steel
$\epsilon_{ult} = \frac{531 - 242}{\frac{E}{85}} = 0.12$	Plastic ultimate strain
$E_{steel} = 210$ GPa	Modulus of elasticity of usual steel
$\nu = 0.3$	Poisson coefficient
$H = E/85$	Rigidity of Plastic region

Defined support is for the problem of a cantilever support which is defined in connecting the turbine base to the seafloor base.Appropriate mesh for analysis of intended problem for Shell element is in the form of shell four-tied (Squad) of structural type.

Results

Here, the intended various points on the turbine is shown briefly as follows:

This Study in 5 different modes of the floating mass displacements in 2800, 8400, 16800, 28000, and 56000 tones will be investigated. In each of the important parameters such as reaction support, horizontal movements, stresses Von-Mises as well as elastic and plastic strains are calculated by the software between the different states performed in the form of (3) to (6), a comparison between the above parameters is shown in different positions.

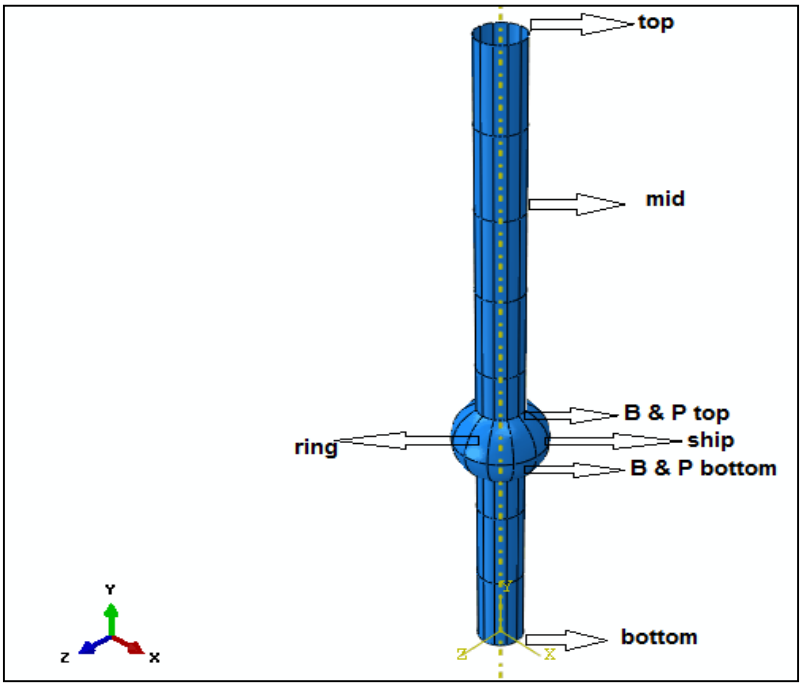

Figure2. Clarifying different points on the turbine

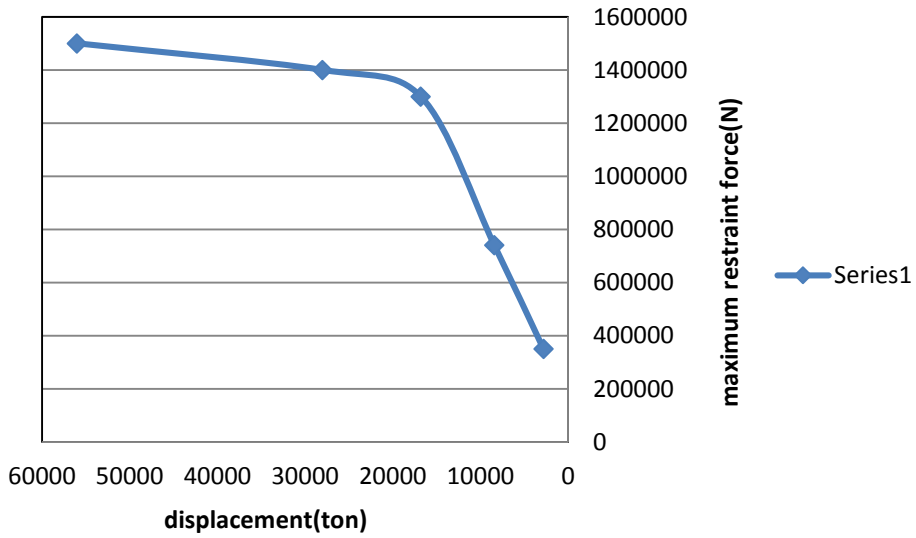

Figure 3. Comparison between maximum support forces in different cases of collision

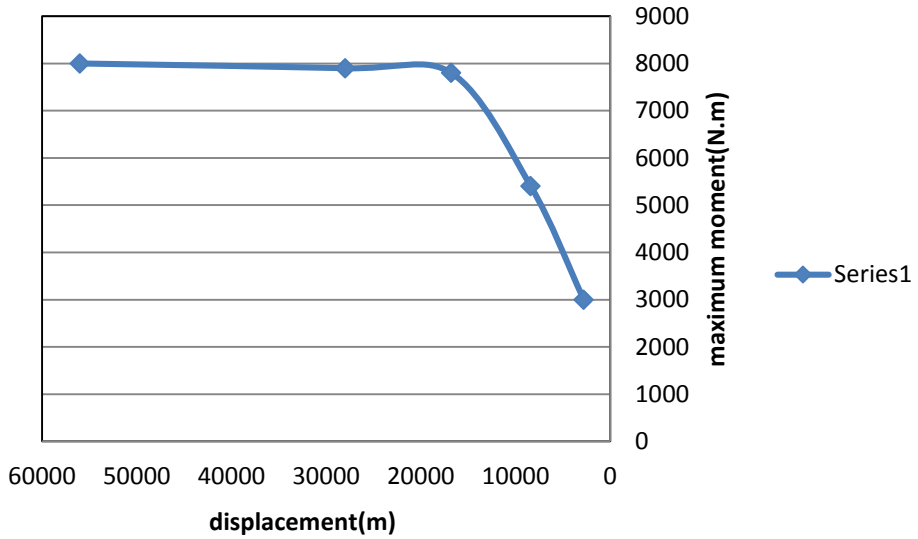

Figure 4. Comparison between maximum support moments in different cases of collision

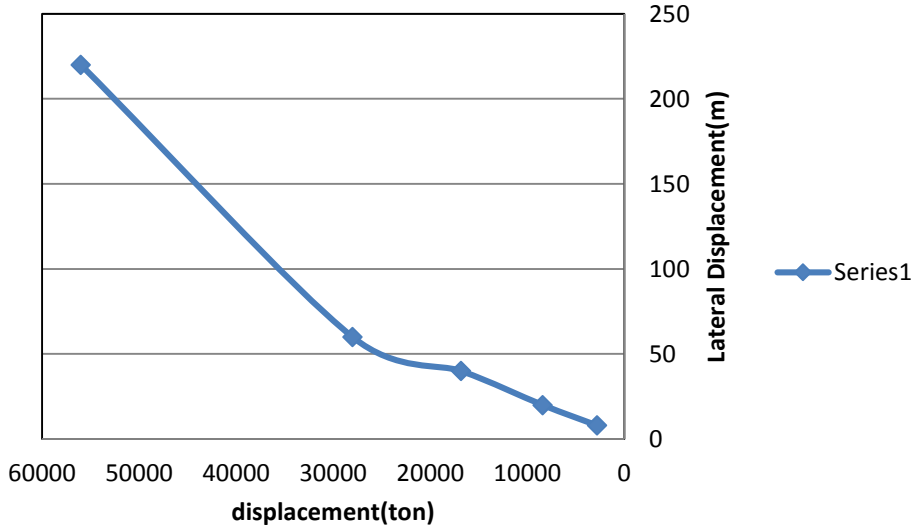

Figure 5. Comparison between maximum horizontal displacements of points on the structure in different case of collision

Comparing maximum horizontal displacement of turbine points in different cases

As the Figure 5 also suggests the maximum displacement of the top spot in the fifth turbine loading is equal to 220 cm.

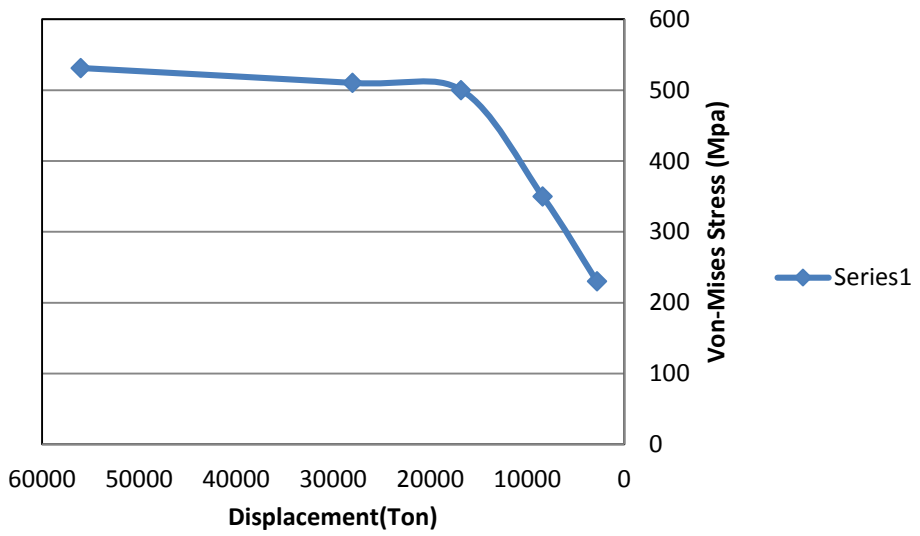

Figure 6. Comparison between maximum stresses of von-mises in different cases of collision

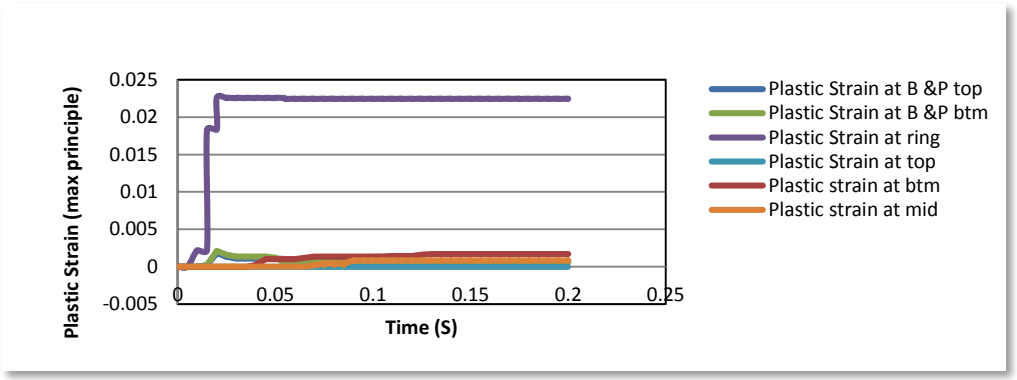

Figure 7. Elastic and plastic strains of points in the fifth case of collision

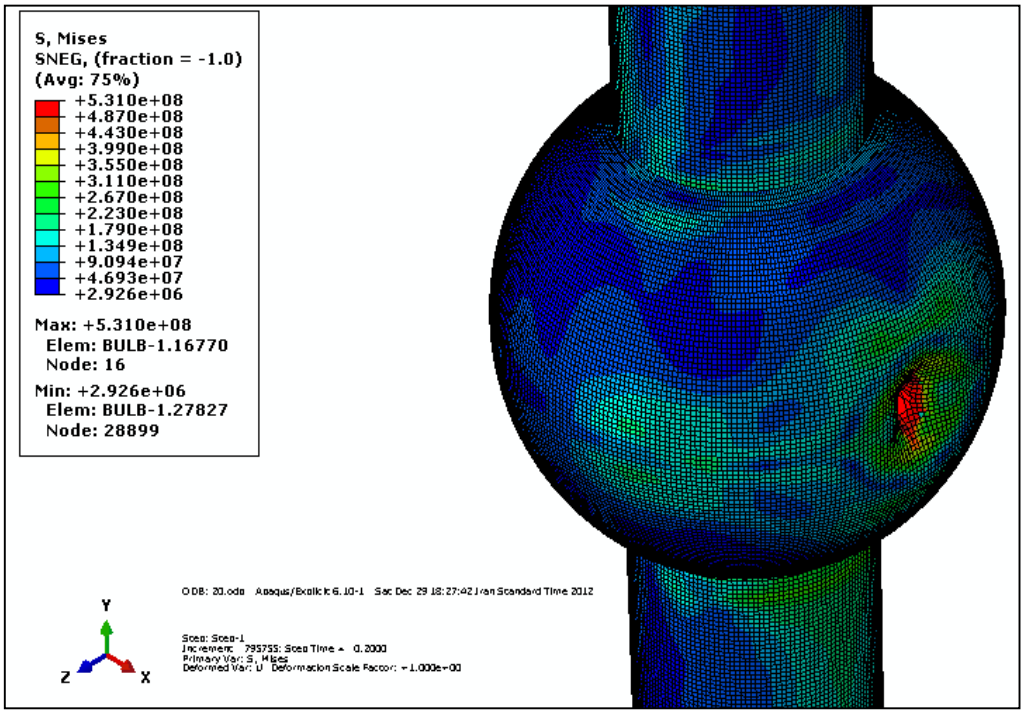

Figure 8. Contour of tensions on the turbine in the moment of t=200 ms and in the fifth case of collision

Conclusion

For observing the effect of mass floating movement on the output of the software in the process of treatment, the 5 different modes were investigated. After the software in different states came to the conclusion that the maximum forces and support reactions happen when a vessel is considered to have the largest mass movement.

However, the maximum displacement of different points along the x-axis and in the case of collision, it is important that only a fifth (to enter the field of plastic and structural failure) of maximum displacement, right at the point of impact.

While in four other cases, the maximum displacement is in the highest point of the turbine.

Finally, in the last case of collision, the point of contact with rot and compaction floating sphere that designs and principles of the turbine should be considered.

If this project in the future is to be continued to assess the following items, it can be more real output software solutions to help us.

- Flexible seabed soil intended to reduce the natural frequency of the system and finally Mono-pile turbines and soil interaction can also be calculated.
- Floating geometric model of ABAQUS software in order to ensure more accurate results.
- The effect of dynamic blade rotation and vibration are also taken into account.

References

[1] PETRONAS Technical Specifications, 2005, PTS 20.073, Design of Fixed Offshore Structures.

[2] Serco Assurance (2003). "Ship-Platform Collision Incident Database", Health and Safety Executive, Research report 053.

[3] Ellinas, C.P., "Mechanics of Ship/Jack-up Collision", J. Construct. Steel Research, V.33, 1995, pp. 283-305.

[4] Menkes S.B., Opat, H.J., "Tearing and Shear Failures in Explosively Loaded Clamped Beams", Exp. Mech., 1973.

[5] Teeling-Smith R.G., Nurick G.N. "The Deformation and Tearing of Thin Circular Plates Subjected to Impulsive Loads". International Journal of Impact Engineering, 1991.

[6] Olson, M.D., Fangan, J.R., and Nurick, G.N., "Deformation and Rupture of Blast Loaded square Plates-Predictions and Exprimental". International Journal Impact Engineering, 1993.

[7] Nurick G.N., Shave C.G. "Deformation and tearing of Thin Square Plates Subjected to Impulsive Loads". International Journal of Impact Engineering, 1995.

[8] L.A. Louca, Y.G. Pan. "Response of Stiffened Plate under Blast Load Engineering Structure, Vol.20, No.12, 1998.

[9] Nurick G.N., Olson M.D., Gagnan J.R. and Levin, A. "Deformation and tearing of blastloaded stiffened square plates". International Journal of Impact Engineering, 1995.

[10] K W Consultants Ltd (2002). "Resistance of Semi-submersibles to Collision," Health and Safety Executive, Offshore Technology Report 2002/007.

[11] American Petroleum Institute, 2000, API RP 2A-WSD, Planning, Designing and Constructing Fixed Offshore Platforms.

[12] Sadeghi, Kabir, "Engineering Coasts, Ports and Marine Structures", Department of Water and Power (Shahid Abbaspoor), 1380.

[13] Patil, K.C., and Jangid, R.S., Passive Control of Offshore Platform. Ocean Engineering, Vol. 32, pp. 1933-1949,2005.

[14] Morison, J. R, O'Brien, M. P., Johnson, J. W., and Schaaf, S. A, 1950. "The forces exerted by surface waves on 50onopoles". 1.Petrol. Teehn., 189, pp. 149-154.

[15] DNV, Det Norske Veritas. DNV-OS-J101 Offshore Standard. Design of Offshore Wind Turbine Structures. 2011.